

**LASER TRANSMISSION WELDING OF  
POLYBUTYLENE TEREPHTHALATE AND  
POLYETHYLENE TEREPHTHALATE BLENDS**

by

Sina Khosravi Maram

A thesis submitted to the Department of Chemical Engineering

In conformity with the requirements for  
the degree of Master of Applied Science

Queen's University

Kingston, Ontario, Canada

(August, 2010)

Copyright ©Sina Khosravi Maram, 2010

## Abstract

Laser Transmission Welding (LTW) involves localized heating at the interface of two pieces of plastic (a laser transparent plastic and laser absorbing plastic) to be joined. It produces strong, hermetically sealed welds with minimal thermal and mechanical stress, no particulates and very little flash. An ideal transparent polymer for LTW must have: a low laser absorbance to avoid energy loss, a low level of laser scattering so it can provide a maximum energy flux at the weld interface and also have a high resistance to thermal degradation. The objective of the project was to analyze the effect of blend ratios of polybutylene terephthalate and polyethylene terephthalate (PBT/PET) on these laser welding characteristics.

The blends were manufactured by DSM (Netherlands). They were characterized using Differential Scanning Calorimetry (DSC) and Thermal Gravimetry Analysis (TGA). The latter technique was used to estimate the order ( $n$ ), activation energy ( $\Delta H$ ) and frequency factor ( $A'$ ) of the degradation reaction of the polymer blends.

The normalized power profile of the laser after passing through the transparent polymer was measured using a novel non-contact technique and modeled using a semi-empirical model developed by Chen [1]. Adding more PET ratio to the blend, did not change beam profile of the transmitted beam significantly. Laser welding experiments were conducted in which joints were made while varying laser power and scanning speed. Measuring the weld strength and width showed that the blends containing PET have higher strength in comparison to pure PBT.

The temperature-time profile at the interface during welding was predicted using a commercial FEM code. This information was combined with the degradation rate data to estimate the relative amount of degraded material at the weld interface. It showed that increasing the ratio of PET in the blend makes it more resistant against thermal degradation which can be one of the reasons the PET containing blends reach higher weld strengths when compared to pure PBT.

## **Acknowledgements**

I am heartily thankful to my supervisors, Dr. Philip Bates, P. Eng; Professor at the Royal Military of Canada (RMC), and Dr. Gene Zak, P. Eng, Associate Professor at Queen's University, whose encouragement, guidance, support and interactive research environment from the start to the end of this project enabled me to develop a better understanding of the subject. Their enthusiastic guidance and patience throughout the duration of this work are most appreciated.

Special thanks to John Perreault and Clarence McEwen at RMC and Andrea Liskova from Queen's not only for their instruction and assistance during the experiments but also for showing me the true meaning of responsibility and commitment to work.

I would also like to thank James Sauve for his generous assistance in providing NIR spectrophotometer data on polymer reflectance and transmittance for the material used in this study.

And last but not least, I would like to thank my dearest family and my friends namely Reza Zamani, Sara Salehi, Sina Tahamtan, Dr.Amir Tahmasebi, and Dr.Charlene Salazar for being supportive and their moral support throughout the entire project.

# Table of Contents

Abstract.....	ii
Acknowledgements.....	iii
Table of Contents.....	iv
List of Figures.....	vii
Chapter 1 Introduction.....	1
1.1 Introduction to Laser Welding.....	1
1.1.1 Introduction to industrial plastic welding.....	1
1.1.2 Concept of Laser Transmission Welding.....	2
1.1.3 Laser welding history in industry.....	3
1.2 Objective.....	4
1.3 Thesis Organization.....	6
Chapter 2 Literature Review.....	7
2.1 Hardware.....	7
2.1.1 The Laser Review.....	7
2.1.2 Laser Transmission Welding Variants.....	11
2.2 Fundamentals of Laser Transmission Welding in Polymers.....	13
2.2.1 Optical Effects.....	14
Refraction and Reflection.....	14
Scattering.....	19
Absorption.....	24
2.2.2 Process Parameters.....	27
2.2.3 Modeling.....	31

Chapter 3 Material .....	33
3.1 Review of Polyesters.....	33
3.2 Materials Used in This Study.....	36
3.3 Plate Manufacturing.....	37
3.4 Material Properties.....	38
3.4.1 Thermal Properties.....	38
3.4.2 Physical Properties.....	39
3.4.3 Degradation Analysis from TGA Test.....	40
3.4.4 Optical Properties.....	41
Reflection.....	42
Transmission.....	44
Absorption.....	46
Chapter 4 Assessment of Laser Beam Scattering .....	47
4.1 Introduction.....	47
4.2 Equipment/Method .....	48
4.3 Results/Discussion .....	53
Chapter 5 Weld Strength Study .....	62
5.1 Introduction.....	62
5.2 Equipment/Method .....	63
5.2.1 Process Window Study .....	63
5.2.2 Weld Strength Study .....	64
5.3 Results and Discussion .....	65
Chapter 6 Thermal Modeling.....	74
6.1 Introduction.....	74
6.2 Method.....	76

6.2.1 Material Properties.....	76
6.2.2 Input Laser Beam Energy Distribution .....	77
6.2.3 Software and Mesh optimization .....	78
6.3 Results and Discussion .....	79
Chapter 7 Degradation Analysis .....	85
7.1 Introduction.....	85
7.2 Equipment/Method .....	89
7.3 Results/Discussion .....	89
Chapter 8 Conclusions and Recommendations.....	98
8.1 Conducted Work .....	98
8.2 Contributions .....	98
8.3 Conclusions.....	99
8.4 Recommendations.....	100
Bibliography .....	102
Appendix A.....	110
A.1- Thermal Properties.....	110
- Heat Capacity.....	110
- Heat Conductivity .....	112
- Thermal Expansion Coefficient .....	114
Appendix B.....	115
Appendix C.....	121
Appendix D.....	124
Appendix E.....	130

## List of Figures

Figure 1-1 Schematic view of Laser Transmission Welding .....	3
Figure 2-1 Stimulated emission where the atom in the excited state loses a photon, by interaction with another photon .....	8
Figure 2-2 Apparatus designed to measure beam profile in pinhole technique [14] .....	10
Figure 2-3 Typical 1-D beam profile at a working distance of 82.5 mm for DLx16 diode laser [14].....	11
Figure 2-4 Different methods for delivery of the laser beam to the joint interface: a) contour welding b) simultaneous welding, d) quasi-simultaneous welding [15].....	12
Figure 2-5 Various possible interactions between the laser beam and polymer .....	13
Figure 2-6 Light refraction when passing the interface between two media .....	15
Figure 2-7 Transmittance and reflection variation at different incident angles for polycarbonate (PC) [12] .....	17
Figure 2-8 Transmittance and reflection variation at different incident angles for high-density polyethylene (HDPE) [12] .....	17
Figure 2-9 Schematic view of an integrating sphere used for reflectance measurement [21] .....	18
Figure 2-10 Influence of the thickness on reflectance for PA mXD6 with 50% GF [22] .....	19
Figure 2-11 Scattering behavior of different materials in interaction with laser beam [24].....	20
Figure 2-12 Schematic graph of power flux distribution at different positions of the beam [8]....	21
Figure 2-13 Line energy intensity for the $i^{\text{th}}$ laser point beam in contour welding [2] .....	22
Figure 2-14 Non-contact method measured LE causing surface damage to laser-transparent part, degradation and melting to laser-absorbent parts for PC with 0.05 wt. % CB [2].....	28
Figure 2-15 Common joint types A) butt joint, B) T-Like joint , C) lap joint .....	29

Figure 2-16 Weld shear strength vs. laser scan power for different gap dimensions for 0.025% CB [2].....	30
Figure 3-1 Two steps in polymerization of poly (ethylene Terephthalate): A. Ester interchange of dimethyl terephthalic acid and ethylene glycol B. High-temperature esterification to yield high-molecular-weight polymer and ethylene glycol as a by-product [42].....	34
Figure 3-2 PBT production processes A) DMT trans-esterification B) PTA polymerization .....	35
Figure 3-3 Dimensions of the transparent part (left) and the absorbing part (right) made by injection molding .....	37
Figure 3-4 Heat capacity variation at different temperatures from MDSC for three blends.....	39
Figure 3-5 Degradation analysis of three blends of PBT/PET.....	41
Figure 3-6 Spectrophotometer measurement of total reflectance of polymer [2] .....	42
Figure 3-7 Reflectance ratio at different wavelengths for three blends of PBT/PET 100/0, 90/10, 75/25 .....	43
Figure 3-8 Schematic view of the integrating sphere used in order to measure transmission for samples for various wavelengths [2].....	44
Figure 3-9 Transmission ratio at different wavelengths for three blends of PBT/PET 100/0, 90/10, 75/25 .....	45
Figure 3-10 Absorption ratio at different wavelengths for three blends of PBT/PET 100/0, 90/10, 75/25 .....	46
Figure 4-1 Rofin-Sinar DLx16 HP diode laser and welding fixture in UW200 Workstation [41]	47
Figure 4-2 Schematic view of laser scanning over the transparent part on a non-contact method [8].....	48
Figure 4-3 Melt lines after laser scanning over the absorbing part for PBT/PET 75/25.....	50
Figure 4-4 Threshold power variation in three different locations along the scanning direction for PBT/PET 100/0, 90/10 and 75/25 .....	53

Figure 4-5 Thickness distribution for the transparent part with nominal dimensions of 2.5 cm × 10 cm × 2 mm .....	54
Figure 4-6 Normalized power distribution after the scattered laser gets absorbed by the black part (PBT/PET 100/0) for 12.6mm and 42.2mm distance from the edge .....	56
Figure 4-7 Normalized power distribution after the scattered laser gets absorbed by the black part (PBT/PET 90/10) for 12.6mm and 42.2mm distance from the edge .....	56
Figure 4-8 Normalized power distribution after the scattered laser gets absorbed by the black part (PBT/PET 75/25) for 12.6mm and 42.2mm distance from the edge .....	57
Figure 4-9 Normalized power distribution of all three blends at 12.66 cm distance away from the edge of the part .....	57
Figure 4-10 Comparing the relative power ( $P_0/P_k$ ) vs. melt width for PBT/PET 100/0 and PA6-0GF .....	58
Figure 4-11 Half of melt-width variation at the edge and the middle of PBT/PET 100/0 part.....	60
Figure 4-12 Half of melt-width variation at the edge and the middle of PBT/PET 90/10 part.....	60
Figure 4-13 Half of melt-width variation at the edge and the middle of PBT/PET 75/25 part.....	61
Figure 5-1 Schematic view of the transparent and absorbing part used for operating window test .....	63
Figure 5-2 Schematic view of the apparatus used for making the overlapped welds .....	64
Figure 5-3 Operating window for PBT/PET 100/0.....	66
Figure 5-4 Operating window for PBT/PET 90/10.....	66
Figure 5-5 Operating window for PBT/PET 75/25.....	67
Figure 5-6 Deformation on the transparent part for PBT/PET 75/25 by increasing the power .....	68
Figure 5-7 Photograph showing "recovery" after heating for PS [37].....	69
Figure 5-8 Maximum load at different laser powers, with scanning speed of 1000 mm/min for three blends of PBT/PET 100/0, 90/10, 75/25 .....	70

Figure 5-9 Weld interface for PBT/PET 100/0 with A) Scanning power of 80W and B) Scanning power of 90W .....	70
Figure 5-10 Melt width at different laser powers, with scanning speed of 1000 mm/min for three blends of PBT/PET 100/0, 90/10, 75/25 .....	71
Figure 5-11 Shear strength at different laser powers, with scanning speed of 1000 mm/min for three blends of PBT/PET 100/0, 90/10, 75/25 .....	73
Figure 6-1 Schematic view of the scattered laser beam passing plane A in a 2-D case of laser transmission welding .....	75
Figure 6-2 2-D NPDF of unscattered laser beam at 82.5mm distance from laser head [14] .....	77
Figure 6-3 Mesh grid on plane A .....	78
Figure 6-4 Maximum temperature at the centre of the weld as a function of mesh size .....	79
Figure 6-5 Sensitivity study to estimate extinction coefficient for the black part for PBT/PET 100/0 .....	80
Figure 6-6 Temperature distribution at the weld interface from the FE model for PBT at t=1sec	81
Figure 6-7 Temperature predicted by the FE model at the centre of the weld 0.035mm below the interface for PBT/PET 100/0 .....	82
Figure 6-8 Temperature predicted by the FE model at the centre of the weld 0.035mm below the interface for PBT/PET 90/10 .....	83
Figure 6-9 Temperature predicted by the FE model at the centre of the weld 0.035mm below the interface for PBT/PET 75/25 .....	83
Figure 7-1 TGA results for the three blends of PBT/PET .....	90
Figure 7-2 Order of the reaction for blends of PBT/PET 100/0, 90/10, 75/25 .....	91
Figure 7-3 Activation energy for blends of PBT/PET 100/0, 90/10, 75/25 .....	91
Figure 7-4 Frequency factor for blends of PBT/PET 100/0, 90/10, 75/25.....	92
Figure 7-5 Degradation model validation for PBT/PET 100/0.....	93

Figure 7-6 Degradation model validation for PBT/PET 90/10.....	93
Figure 7-7 Degradation model validation for PBT/PET 75/25.....	94
Figure 7-8 Temperature predicted by the FE model for a laser scan for PBT at 100 W .....	95
Figure 7-9 $m/m_o$ at different powers as a function of the time for PBT/PET 100/0.....	95
Figure 7-10 $m/m_o$ at different powers as a function of the time for PBT/PET 90/10.....	96
Figure 7-11 $m/m_o$ at different powers as a function of the time for PBT/PET 75/25.....	96
Figure 7-12 Shear strength as a function of power for three blends of PBT/PET .....	97
Figure A-1 Heat capacity variation at different temperatures resulted from MDSC for three blends .....	111
Figure A-2 Linear expansion coefficient vs. temperature for PET(left) and PBT(right).....	114
Figure C-1 Schematic view of injection molded dogbones .....	121
Figure C-2 Applied load versus the extension for PBT/PET 100/0.....	122
Figure C-3 Applied load versus the extension for PBT/PET 90/10.....	122
Figure C-4 Applied load versus the extension for PBT/PET 75/25.....	123
Figure E-1 Linear Relationship for Order of the Reaction ( $n$ ) and Activation Energy ( $E$ ) for PBT/PET 100/0.....	131
Figure E-2 Linear Relationship for Order of the Reaction ( $n$ ) and Activation Energy ( $E$ ) for PBT/PET 90/10.....	131
Figure E-3 Linear Relationship for Order of the Reaction ( $n$ ) and Activation Energy ( $E$ ) for PBT/PET 75/25.....	132
Figure E-4 Linear Relationship used for measuring frequency factor ( $A'$ ) for PBT/PET 100/0..	132
Figure E-5 Relationship used for measuring frequency factor ( $A'$ ) for PBT/PET 90/10 .....	133
Figure E-6 Relationship used for measuring frequency factor ( $A'$ ) for PBT/PET 75/25 .....	133

## List of Tables

Table 2-1 Refractive indices for different plastics .....	16
Table 3-1 Temperature distribution at different positions of the injection molder for PBT (Arnite T) and PET (Arnite A) [48] .....	37
Table 3-2 Thermal properties of the blends based on DSC studies .....	38
Table 3-3 General properties of base polymers PBT and PET .....	40
Table 3-4 Reflectance values for 2mm plaques .....	43
Table 3-5 Transmission for 2 mm thick plaques.....	45
Table 4-1 The beam profile distribution at 12 mm and 42 mm distance from the edge of the plate .....	55
Table 5-1 Average load at break and tensile test for three blends .....	72
Table 6-1 Summary of optical properties for three blends of PBT/PET 100/0, 90/10 and 75/25..	76
Table 6-2 Maximum temperature predicted by the model for three blends using 55, 70, and 100W laser power settings.....	84
Table 7-1 Results obtained from TGA data compared to other references.....	92
Table A-1 Thermal properties of the blends based on DSC studies .....	111
Table A-2 Thermal conductivity for the range of 31~104°C for PBT/PET 100/0 .....	112
Table A-3 Thermal conductivity for the range of 31~104°C for PBT/PET90/10 .....	113
Table A-4 Thermal conductivity for the range of 31~104°C for PBT/PET 75/25 .....	113
Table D-1 Temperature variation at time range of 0.74-1.23 for PBT/PET 100/0 .....	124
Table D-2 Temperature variation at time range of 0.74-1.23 for PBT/PET 90/10 .....	126
Table D-3 Temperature variation at time range of 0.74-1.23 for PBT/PET 75/25 .....	128

## Nomenclature

$A$	Light(laser) absorption coefficient of polymer, 1/m
$a$	Weld area, m <sup>2</sup>
$A'$	Frequency factor, min <sup>-1</sup>
$a_p$	Area of the pinhole, mm <sup>2</sup>
$A_T$	Absorbed ratio of the light
$C$	Constant
$c$	Heat capacity, J/(kg K)
$C_A$	Concentration of non-decomposed polymer, Moles/m <sup>3</sup>
$C_{sca}$	Scattering cross section, m
$D_a$	Thickness of laser-absorbent part, m
$E$	Activation Energy, J/moles
$E''(x, y)$	Total line energy intensity of the transmitted laser beam at given position of $(x,y)$ , J/m <sup>2</sup>
$E''_{di}(x, y)$	Direct line energy intensity from $i^{\text{th}}$ laser point beam at given position of $(x,y)$ , J/m <sup>2</sup>
$E''_{si}(x, y)$	Scattered line energy intensity from $i^{\text{th}}$ laser point beam at given position of $(x,y)$ , J/m <sup>2</sup>
$i$	Angle of incident light
$K_R$	Reaction rate constant, [Concentration/time]
$K_E$	Light (laser) extinction coefficient of polymer, 1/m
$k$	Thermal conductivity, W/(m K)
$K_T$	Transmitted ratio of the light
$LE$	Line Energy, J/m
$m$	Mass of the degraded sample at given time, kg
$M$	Molecular weight of the polymer repeat unit, kg

$m_0$	Initial mass of the sample before polymer degradation, kg
$m_f$	Final mass after complete polymer degradation, kg
$MW$	Molecular weight of the molecule, kg
$N$	Order of the reaction
$N_A$	Avogadro's number
$n_i$	Refraction at $i^{\text{th}}$ medium
$P$	Laser power, W
$p(\theta)$	Normalized phase function
$P_{in}$	Laser power for the onset of surface melting of the laser absorbent part using the non-contact method, W
$P_{i,j}$	Power passing through the pinhole at the $(i,j)$ coordinate, W
$P_{out}$	Laser power after passing through the polymer, W
$P_{ref}$	Laser power reflected from the polymer, W
$p_y(x - x_i)$	1-D Gaussian function for light intensity at position $x$ at weld interface, $1/m$
$P_i$	Laser power of the $i$ -th discretized beam before transmission, W
$P_0$	Melting threshold power for the absorbing part, W
$P''_{si}$	power intensity of scattered light from the $i^{\text{th}}$ point beam at $(x, y, z)$ in $x$ - $z$ plane, $W/m^2$
$P''_{di}$	power intensity of direct light from the $i^{\text{th}}$ point beam at $(x, y, z)$ in $x$ - $z$ plane, $W/m^2$
$Q(x, y, z)$	Heat source or heat sink, $W/m^3$
	Laser power absorbed by a unit volume polymer, $W/m^3$
$R$	Gas constant, $J/(K \text{ mol})$
$r$	Angle of refracted light

$R_T$	Reflected ratio of the light
$S$	Light(laser) scattering coefficient of polymer, 1/m
$T$	Temperature, K
$t$	Time, sec
$T_M$	Melting temperature, K
$W_i$	Width of the $i^{\text{th}}$ point laser beam, m
$w_k$	Width of the molten area, mm
$\alpha$	Linear thermal expansion coefficient, 1/K
$\alpha_e$	Absorption due to electron transition
$\gamma$	Non-decomposed mass fraction
$\delta$	Laser power or energy scattering ratio, as a function of weld interface
$\delta(y)$	Laser power or energy scattering ratio, as a function of depth $y$
$\Delta x$	Measurement increment along X axis, m
$\Delta y$	Measurement increment along Y axis, m
$\eta$	Reflectance
$\lambda_i$	Light wavelength at the $i^{\text{th}}$ medium, m
$\rho$	Density, Kg/m <sup>3</sup>
$\sigma$	Scattering standard deviation at the weld interface ( $y=0$ ), m
$\sigma(y)$	Scattering standard deviation at depth $y$ in $x$ - $z$ plane for laser transparent part, m
$\tau$	Weld shear strength, MPa
$v_i$	Light speed at the $i^{\text{th}}$ medium, m/sec
$v$	Laser scanning speed, mm/min
$\varphi_{i,j}$	Average power flux, W/m <sup>2</sup>

$\Psi$	Normalized Power Flux Distribution(NPFD), J/mm <sup>2</sup>
$\Psi^*(0)$	Normalized Power Flux Distribution at the centre of the scattered beam ( $y=0$ ), W/mm <sup>2</sup>

# Chapter 1

## Introduction

This chapter introduces Laser Transmission Welding (LTW), an industrial technique used for joining of thermoplastics. The different laser energy delivery techniques are described briefly. Finally, the objective of the thesis is addressed.

### 1.1 Introduction to Laser Welding

#### 1.1.1 Introduction to industrial plastic welding

Plastic components play a major role in day-to-day life. Because of their diverse characteristics, plastics have found their way as a suitable substitute for a broad range of materials used in different components. Replacing metal parts by plastics creates new applications as well as issues. Joining parts is one of these issues. With the exception of mechanical fastening, plastic joining can be subdivided into two categories: chemical bonding and welding. In the first technique, a tertiary substance (adhesive) is used to create a bond between the parts. The bond may involve non-chemical electrostatic forces between the adhesive molecules and the molecules on the substrate surface, or chemical forces between the adhesive and the adherent. The second technique, welding, consists of inducing a local phase change in the parts by heating up the interface and then providing the pressure to allow the materials to mix at the molecular level by diffusion. Different welding processes are used based on a variety of the heating sources and can be categorized as:

- *Thermal welding* : Hot plate, hot gas, extrusion, implant resistance and impulse welding;

- *Friction welding* : spin, ultrasonic, vibration welding;
- *Electromagnetic welding* : Implant induction, radio frequency, microwave, infrared and laser welding;

### **1.1.2 Concept of Laser Transmission Welding**

Laser Transmission Welding in plastics requires one part to be laser-transparent and a second to be laser-absorbing. In this technique, as shown in Figure 1-1, the laser beam passes through the bulk of transparent material, and generates the required energy by being absorbed near the surface of the absorbent part underneath. Materials are often made absorbent by mixing carbon black (CB) with the polymer. The absorbed energy causes a temperature rise in the absorbent part. Heat then flows into the transparent part by conduction. Once the material in both parts has melted or softened, molecular diffusion occurs between materials in the two parts, causing mixing of two materials on a molecular scale. Eventually, heat loss from the interface causes the material to solidify resulting in formation of the joint.

The fast cycle time and absence of relative part movement or vibration are a few of the advantages of this technique. Because of the straight and homogenous weld lines created in this technique, laser welding is a suitable joining method for parts where aesthetics are of importance, such as for automotive lighting [2]. It is also used to weld enclosures containing sensitive electronic components that would be damaged during any welding operation that involves relatively high frequency vibrations such as would be encountered in ultrasonic or vibration welding. The other advantage of this method compared to the other conventional welding methods is the high precision of the laser beam that makes it possible to weld miniature parts [1]. However, complexity and poorly understood interaction between the laser and the transparent material is one of the major disadvantages of this technique.

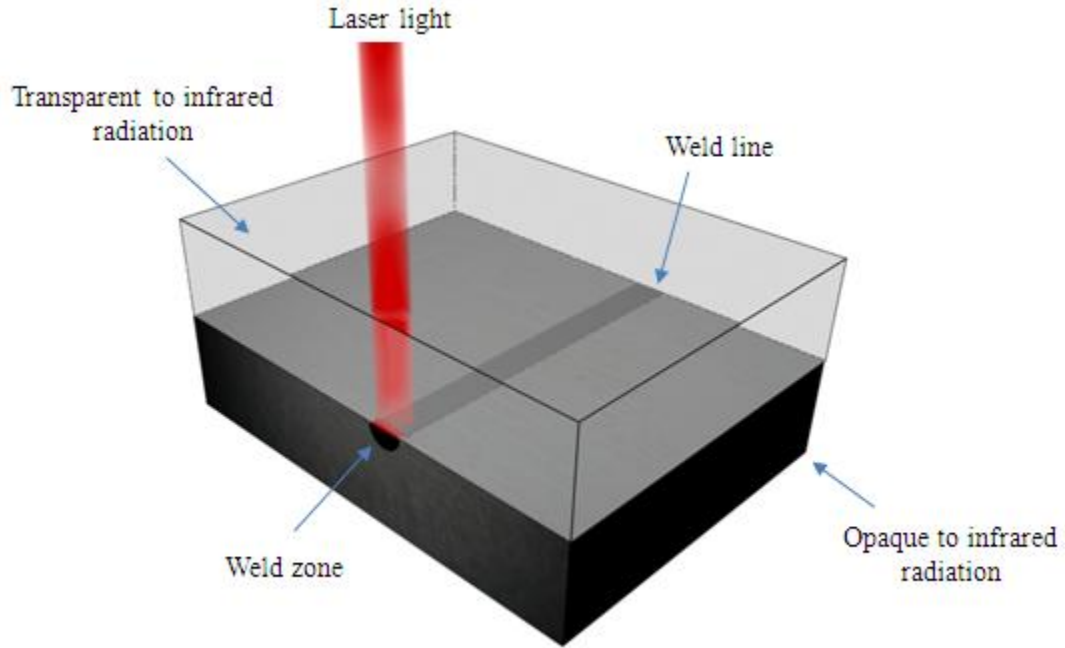


**Figure 1-1 Schematic view of Laser Transmission Welding**

### **1.1.3 Laser welding history in industry**

Laser welding has been used by the automotive industry for several decades. Fiat applied a CO<sub>2</sub> laser in 1975 to weld metal power train components. Gradually, by the 1980's, many car manufacturing companies started to replace resistance spot welding by laser welding to produce metal tailored welded blanks [3]. Through the invention of new technologies to generate the laser beam and to distribute it to the working space, the costs for this welding technique decreased to the point that it was cost-effective to apply laser welding to materials other than metals. The automotive industry is one area where the polymer laser welding technology has a good potential for significant expansion. For exterior applications, welding of lighting systems is under

investigation. Most of the lighting assemblies currently produced are made for vibration and hot plate welding technologies or require the use of adhesives. In many cases, there is a poor fit between the lens and the housing at the joint. This is a major concern for laser welding [4]. The first mass-produced part made using laser transmission welding was a keyless entry device for Mercedes in 1997. Recently BMW along with Bayer Inc. devised a process using laser transmission welding in combination with heated tool welding for commercial production of plastic air intake manifolds [5].

In the field of biomedical applications, laser welding is becoming more widely used for products such as disposable miniature devices for testing fluids such as blood [4]. This technique is also starting to take the place of adhesives that have been used to assemble the syringes. These parts historically had problems in high volume operations that required a high-level of cleanliness. Due to the potential of laser welding for making accurate, high quality, miniature joints, advantages in function, process time and economics are expected, which are promising for a wide range of applications [4].

## 1.2 Objective

The ideal polymer in a transparent part must have a low absorbance of laser energy in order to avoid the energy loss that would lead to heating of this component. Heating may cause melting and potentially other damage away from the weld interface. The ideal polymer must also cause little scattering of the laser light from its initial path in the transparent part. Scattering increases the path length the light must travel that can indirectly lead to energy absorption in the transparent part. It can also lead to a widening of the laser beam at the weld interface. This combination of energy loss and increased beam cross-sectional area results in a decreased power flux at the weld interface. Insufficient power flux at the interface may result in melting

temperature not being reached. Too much power flux at the interface has been shown to cause polymer degradation. Both too little and too much power will ultimately affect the weld strength [6].

The absorbance characteristic of a polymer depends on its molecular structure. Absorption of electromagnetic radiation happens once the energy of a photon is absorbed by the material. This energy is then transformed to other forms of energy, like heat. The absorbance is wavelength-dependent [7]. Scattering is caused by reflectance and refraction at interfaces within the polymer structure. These interfaces can be between amorphous and crystalline phases as well as between polymer and reinforcement.

The primary objective of the project was to study the effect of blending *Polybutylene Terephthalate (PBT)* with *Polyethylene Terephthalate (PET)* on:

- Laser light absorption and scattering. Laser light absorption was measured by an absorption spectroscopy technique using an integrating sphere. The scattering of the laser light, was analyzed by the weld line Transverse Energy Density Distribution (TEDD) technique developed by Zak et al. [8]. The output was modeled using a semi-empirical model developed by Chen [1] in order to predict the power distribution of the laser at the weld line.
- Weld strength and width. This was achieved by using different welding parameters such as laser power and laser speed to manufacture lap-shear specimens for each blend. The tensile strength and weld width were then measured and compared.
- Thermal degradation. This study examined the thermal degradation that can take place if the local power flux is too high in the centre of the weld. This was achieved by first determining the welding conditions at which degradation was believed to have occurred based on weld strength data. Degradation at the weld was then numerically predicted by

coupling temperature-time data from a thermal finite element model with information on the kinetics of degradation obtained from TGA results.

The driving force for this study was the DSM Company (Amsterdam, Netherlands), which provided the various compounds for this work.

### **1.3 Thesis Organization**

The second chapter gives a description of lasers in general, and how the laser energy is actually delivered to the part interface (2.1). The literature pertaining to optical effects of the polymer such as reflection, transparency, scattering and absorption is then reviewed in section 2.2.1. The effects of important LTW process parameters are then summarized in section 2.2.2.

Chapter 3 discusses the material under investigation. A brief introduction on polyesters is presented in section 3.1. Sections 3.2 and 3.3 describe the polymer blends provided by DSM and the details related to processing of the materials. Different physical, thermal, chemical and optical properties of these PBT and PET polymers are also described (3.1). Chapter 4 discusses the method used to determine the power distribution of the laser beam after passing through the transparent part for all three blends of PBT and PET.

In Chapter 5, the weld process window, weld strength and weld width of overlap weld joints for different blends are analyzed as a function of laser power and scan speeds.

In Chapter 6, a 2-D transient thermal model of the LTW process is constructed using a finite element method in order to determine the temperature distribution as a function of time and process conditions.

Chapter 7 describes the results of the thermal degradation study obtained using TGA. The degradation-time-temperature results are then simulated using a simple kinetic model. Chapter 7 also describes how the temperature-time simulation results from Chapter 6 can be combined with the kinetic degradation data to predict degradation during welding for each blend.

## Chapter 2

### Literature Review

#### 2.1 Hardware

##### 2.1.1 The Laser Review

The word laser is the abbreviation of Light Amplification by Stimulated Emission of Radiation. Einstein proved that light consists of bundles of wave energy, called photons. It was believed that there are two ways photons and species (i.e., atoms, ions, or molecules) may interact: it can be either by absorption of a photon by a species in a low-energy state that results in an excited species with corresponding increase in energy, or spontaneous emission of a photon by an excited species that results in reduction of its energy. In the latter case, the species can also lose energy without photon emission in a non-radiative decay. However, in 1916, Einstein by reviewing the thermal equilibrium between the photon/species interactions, recognized that the energy density of photons at a given frequency is, on average, constant in time; hence, the rate at which photons of any particular frequency are emitted must equal the rate of absorbing them. Therefore, he concluded that there must exist a third mechanism of interaction – known as stimulated emission – in which an excited species could be stimulated to emit a photon by interaction with another photon which is shown in Figure 2-1. This interaction became the foundation of light amplification that occurs in laser light generation as a coherent optical beam with a constant wavelength and time-dependent phase and amplitude [9].

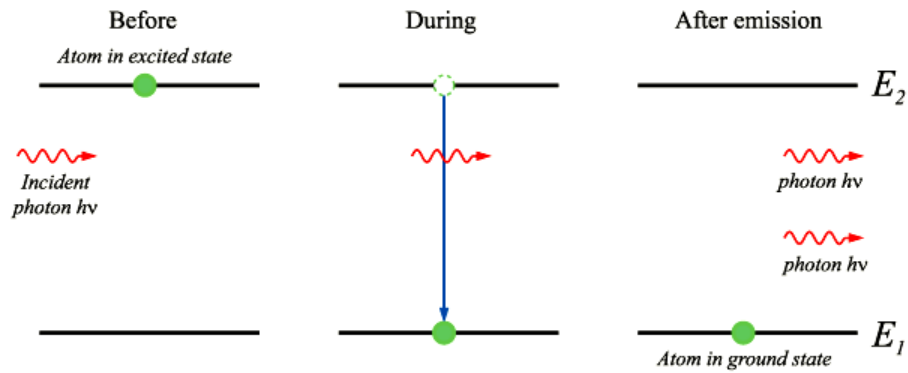


**Figure 2-1 Stimulated emission where the atom in the excited state loses a photon, by interaction with another photon**

Laser light can take the form of a continuous wave (CW), a pulse, or a train of pulses. The length of the pulse can vary from a tenth of a second to a few femtoseconds ( $10^{-15}$  s). Pulses may be produced at a rate of between one and several thousand per second. The average power may vary between milliwatt and kilowatt levels, with peak power attaining the order of gigawatts. Some lasers can be tuned to produce a range of wavelengths [9]. The ideal laser for Laser Transmission Welding (LTW) should be able to function in continuous mode with a wavelength in the near-infrared. In this wavelength region, light transmission through many polymers is high [10]. Common lasers used for polymer processing are Nd:YAG and diode.

In order to reach the powers required to weld plastics (10-200 W) using diode lasers, large numbers of low-power individual laser diode emitters (1-2W) are combined. All these micro lasers are converged in a focal point on the order of one millimeter [11] by means of complex micro optical elements. The delivery of the laser beam to the work piece surface can also be done by fiber optic cables. This method provides an axially symmetric Gaussian or top-hat beam power profile [12].

The spatial distribution of the power flux over the beam cross-section has to be determined [13]. The technique to quantify the power flux distribution is known as beam profiling. There are various techniques for determining the beam power profile. They are generally based on measuring the local power flux at different positions in a plane perpendicular to the laser beam. A common technique, known as the knife-edge approach, involves moving a sharp straight edge incrementally between a laser beam and power sensor. The sharp edge works as a gate that allows certain portions of the laser beam to reach to the power sensor. The power obtained by the power meter increases from zero to full power as the knife edge moves in along one axis. The test can be performed by moving the beam along two axes in order to obtain an estimate of the two-dimensional power distribution [13].

A related technique, known as the pinhole approach, uses a small cooled pinhole with a diameter that has both acceptable levels of power and spatial resolution. Once the laser passes through the hole, it is collected by a power meter sensor underneath as shown in Figure 2-2 Apparatus designed to measure beam profile in pinhole technique. The meter collects power readings over a grid. The average power flux over the pinhole area can be described as:

$$\varphi_{i,j} = \frac{P_{i,j}}{a_p} \quad \text{Equation 2-1}$$

where  $p_{i,j}$  is the power passing through the pinhole at the  $(i, j)$  coordinate and  $a_p$  is the area of the pinhole.

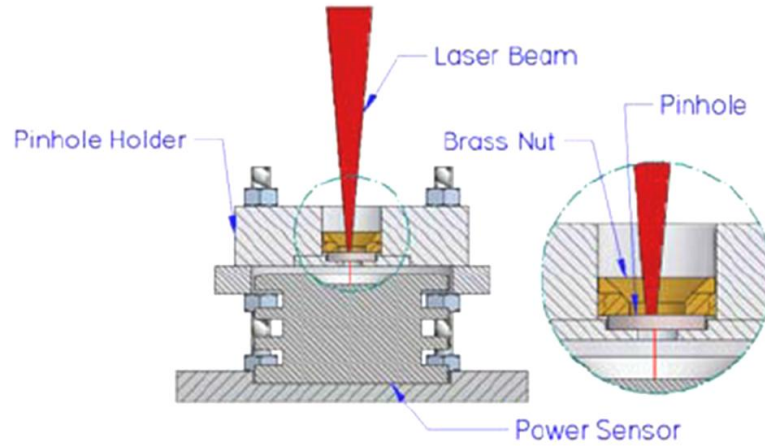


**Figure 2-2 Apparatus designed to measure beam profile in pinhole technique [14]**

By defining  $\Delta x$  and  $\Delta y$  as the measurement increments along  $X$  and  $Y$  axes, the total power can be calculated as:

$$P = \sum_i \sum_j \varphi_{i,j} \Delta x \Delta y \quad \text{Equation 2-1}$$

where  $P$  is the total power emitted by the laser. Equation 2-2 can be used to define  $\Psi_{i,j}$  - the Normalized Power Flux Distribution (NPF) [8]:

$$1 = \sum_i \sum_j \Psi_{i,j} \Delta x \Delta y \quad \text{Equation 2-2}$$

The power flux ( $\varphi_{i,j}$ ) at any point can thus be calculated from the total power ( $P$ ) and the Normalized Power Flux Distribution ( $\Psi_{i,j}$ ):

$$\varphi_{i,j} = P \Psi_{i,j} \quad \text{Equation 2-3}$$

It is therefore a critical parameter for understanding and modeling the LTW process. Typical data for  $\Psi$  from a diode laser at the focal point along and across the scanning direction are shown in Figure 2-3.

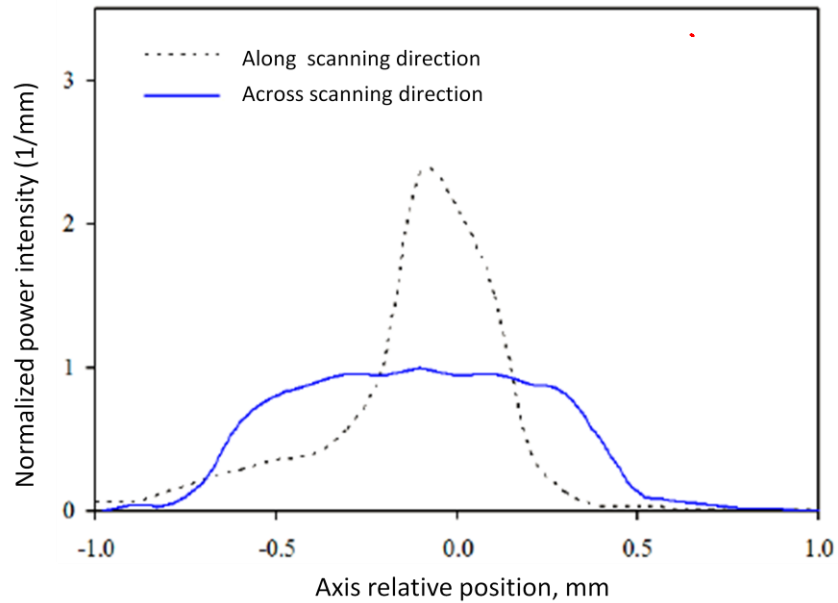


**Figure 2-3 Typical 1-D beam profile at a working distance of 82.5 mm for DLx16 diode laser [14]**

### 2.1.2 Laser Transmission Welding Variants

Laser transmission welding methods can be divided into three categories, depending on the method by which the laser energy is delivered to the work piece: simultaneous, quasi-simultaneous, and contour welding.

Simultaneous welding is defined by continuous irradiation of the entire weld interface by laser energy for the duration of cycle time. In this method, the entire weld seam heats up and starts to soften simultaneously. Under the clamping pressure, liquid material can flow out of the interface, allowing the components to move inwards towards the weld seam. This phenomenon is referred to as meltdown and it can help bridge the small gaps at the interface. The energy is often

delivered to the weld interface using a laser that is coupled to a large number of fibre-optic cables that are then placed around the periphery of the weld. The cost of the laser and fibre-optic system is an issue for large-scale welding such as intake manifolds or headlamps [1].

Given that plastics have relatively low thermal conductivity, it is possible to heat the surface up by repeatedly scanning the weld seam at a high speed using mirrors. This technique, which is referred to as quasi-simultaneous welding, increases the flexibility of the welding process. It is possible to melt-off any gaps between the parts as meltdown occurs. The laser beam spot area also increases as the incident angle decreases for large welding paths. Therefore, the power per unit area varies at different positions of the weld path. This can cause inconsistency in weld strength for large parts and can be considered as one of the disadvantages of this technique [6].

A third approach is contour welding. In contour welding, the laser beam moves once along the welding path. This technique can be achieved by moving the working piece relative to a single continuous laser beam. The advantage of this method is the ability to weld complex geometries since the laser can be programmed for different weld contours. However, since the laser beam passes once over the weld line, no meltdown can occur as it does in simultaneous or quasi-simultaneous variants. Contour welding also can lead to high temperature due to high energy flow to the parts and cause degradation at either interface or the surface of the transparent part. Therefore, choosing the right process condition is important in this welding technique.

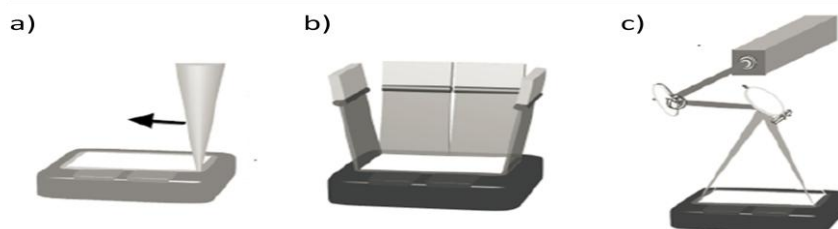


**Figure 2-4 Different methods for delivery of the laser beam to the joint interface: a) contour welding b) simultaneous welding, c) quasi-simultaneous welding [15]**

## 2.2 Fundamentals of Laser Transmission Welding in Polymers

As mentioned previously, laser welding is affected by the optical properties of polymers. These properties are based on the chemical nature of the polymer and its physical state (amorphous or crystalline). Important optical properties are reflection, scattering and absorption. For most LTW variants, it is desirable to bring the maximum energy flow to the weld interface in as concentrated a beam as possible. This energy flux is dependent on the initial laser energy and the area in which it is delivered to the assembly. As Figure 2-5 shows, the optical properties of the transparent part affect this flux as the light travels through the transparent part.

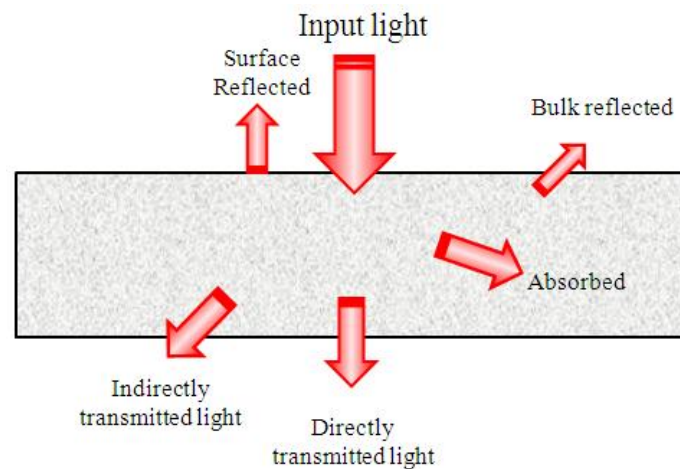


**Figure 2-5 Various possible interactions between the laser beam and polymer**

The energy flux may decrease by either loss of the energy, or increase in the area through which the energy is propagating. There are various reasons for this. Part of this energy gets lost due to back reflection either at the top/bottom surface of the polymer part or at various solid-solid interfaces (amorphous-crystalline or polymer-reinforcement) within the bulk polymer. The total

reflectance ( $R_T$ ) is defined as the ratio of the total reflected laser energy to the total input energy reaching the part's incident interface.

The non-reflected laser light enters the polymer bulk. Some of the light will be absorbed by the polymer as it passes directly through the part thickness. Some of it will be scattered by reflection and refraction at various solid-solid interfaces within the polymer. In the same manner as total reflectance, total absorption  $A_T$  is defined as the ratio of the total absorbed laser energy inside the polymer bulk to the total input energy reaching the part's incident interface. The remaining laser energy passes through the medium and reaches the interface and is referred to as the transmitted ratio  $T_T$ . These ratios are related according to Equation 2-4:

$$T_T = 1 - R_T - A_T \quad \text{Equation 2-4}$$

### 2.2.1 Optical Effects

#### Refraction and Reflection

As the light passes from one medium to another, it can get reflected or refracted from its original path. At the same time, the light changes speed. This can be described by Equation 2-5 [16].

$$n_2 / n_1 = v_1 / v_2 = \lambda_1 / \lambda_2 \quad \text{Equation 2-5}$$

where  $v_1$  is the speed of light in the first medium;  $v_2$  is the speed of light in the second medium;  $\lambda_1$  is the wavelength of light in the first medium;  $\lambda_2$  is the wavelength of light in the second medium ;  $n_1$  is the refractive index of the first medium and  $n_2$  is the refractive index of the second medium. The refractive index for a vacuum is equal to 1. The refractive indices for the other materials can be calculated and are shown in Table 2-1 Refractive indices for different plastics.

Snell's law relates the angles of incidence and refraction as light passes from one medium to another [16]:

$$n_1 / n_2 = \sin i / \sin r \quad \text{Equation 2-6}$$

where  $i$  and  $r$  are the angles of incident and refracted light respectively as shown Figure 2-6.

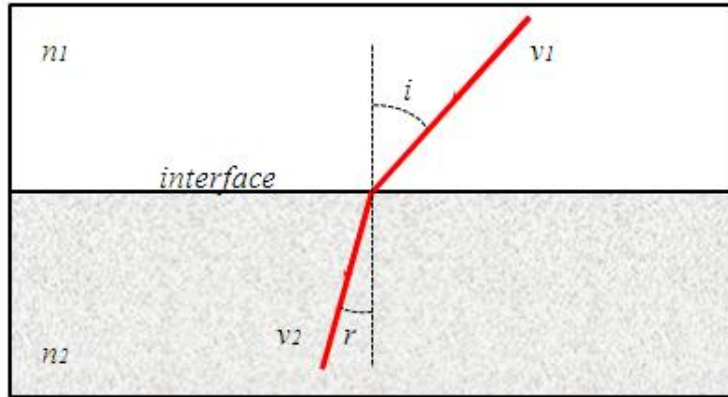


**Figure 2-6 Light refraction when passing the interface between two media**

Polymers that are semi-crystalline contain amorphous and crystalline phases. Hence, they exhibit multiple refractive indices [16]. Passing the light through these heterogeneous materials can result in refraction. This will lead to light scattering and bulk reflection. The refractive indices of amorphous and crystalline phases of semi-crystalline materials can be estimated by Lorenz-Lorentz equation:

$$\frac{n^2 - 1}{n^2 + 2} = \frac{4\pi}{3} \frac{N_A \rho}{M} \alpha \quad \text{Equation 2-7}$$

where  $\rho$  is the sample density;  $\alpha$  the polarizability tensor;  $N_A$  Avogadro's number; and  $M$  the molecular weight of polymer repeat unit [17]. Knowing the values for  $M$  and  $\alpha$ , average refractive indices of the semi-crystalline materials in amorphous or crystalline phase can be

calculated from their respective densities which are calculated in other studies [18]. Results for amorphous and crystalline PBT and PET are shown in Table 2-1.

Reflection will also occur at the air-polymer interface at both the top and bottom surface of the part and at interfaces between amorphous and crystalline phases. In theory, the ideal (specular) surface reflectance  $\eta_i$  of polymers can be calculated based on Fresnel's equation [16]:

$$\eta_i = \frac{(n_2 - n_1)^2}{(n_2 + n_1)^2} \quad \text{Equation 2-8}$$

where  $n_2$  is the refractive index of the material; and  $n_1$  is the refractive index of air. For amorphous materials, specular reflection value usually does not exceed 5% [13].

**Table 2-1 Refractive indices for different plastics**

<b>Polymer</b>	<b>Refractive Indices</b>	<b>Predicted Ideal Surface Reflectance (%)</b>
<b>Poly(propylene)</b>	1.48 [16]	3.7
<b>PET (Amorphous)</b>	1.57 [16]	4.9
<b>PET (Crystalline)</b>	1.66 [19]	6.1
<b>PBT (Amorphous)</b>	1.69 [20] [18]	6.5
<b>PBT (Crystalline)</b>	1.79 [20] [18]	8.0
<b>Poly(styrene)</b>	1.61 [16]	5.4
<b>Nylon6</b>	1.53 [16]	4.4

According to Table 2-1 and Equation 2-7, the theoretical specular reflectance of plastics should be in the range of 3.7% (for polypropylene) to 5.4% (for Polystyrene). However, for semi-crystalline materials, the total reflectance value is higher than this value due to the bulk reflection described earlier.

Several studies have been published regarding both surface and bulk reflection. Rhew et al. [12] investigated the reflectance of polycarbonate (PC) and high-density polyethylene (HDPE)

for various thicknesses and incident angles of the laser beam. This study indicated that by increasing the incident angle of the laser beam, the reflectance increases to 60% for both PC and HDPE as shown in Figure 2-7 and Figure 2-8.

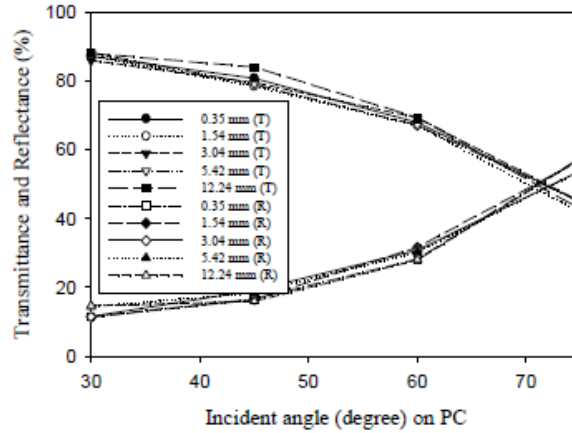


**Figure 2-7 Transmittance and reflection variation at different incident angles for polycarbonate (PC) [12]**

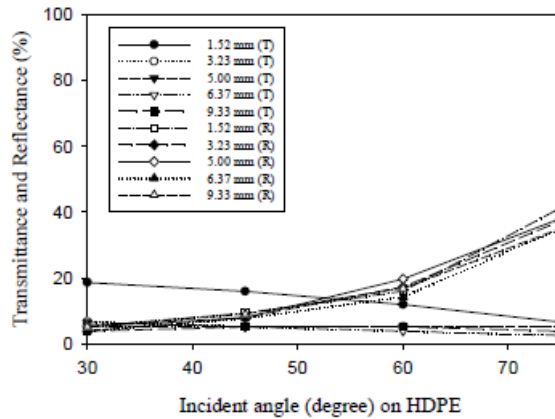


**Figure 2-8 Transmittance and reflection variation at different incident angles for high-density polyethylene (HDPE) [12]**

Wang et al. [21] in studies of optical properties of PC, PP and PA6 showed the effect of the thickness of the transparent part on reflection. In this study, the reflectance of the laser beam at different wavelengths was measured using an integrating sphere as shown in Figure 2-9. In this technique, an IR beam passes through a highly reflective sphere (referred to as an integrating sphere) and contacts a polymer part. Some of the light is reflected from the surface or the bulk of the polymer. It is captured by the detector and the total reflectance can be calculated.

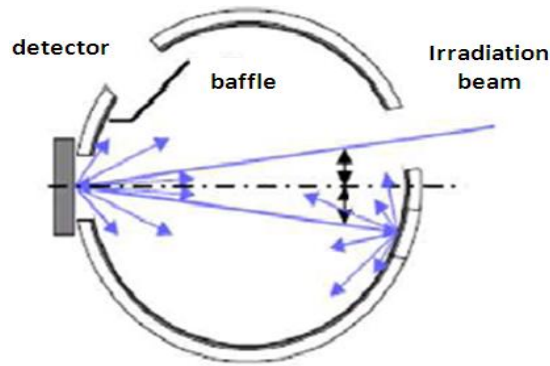


**Figure 2-9 Schematic view of an integrating sphere used for reflectance measurement [21]**

Figure 2-10 shows the bulk reflection for different wavelengths. Increasing the thickness of PA mXD6 containing 50% glass fibre from 0.5 mm to 2.0 mm increases the reflection by more than 20% at a near infrared wavelength of 1000 nm. According to this study, this is due to the back scattering caused by the glass fibres and amorphous-crystalline interfaces in the material [21]. Light scattering in the transparent part affects the transmitted energy flux by increasing the travel distance of the light due to numerous reflections/refractions of the beam along its path.

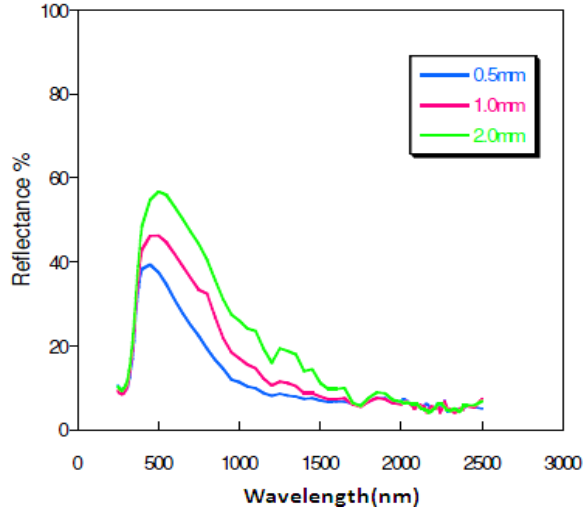


**Figure 2-10 Influence of the thickness on reflectance for PA mXD6 with 50% GF [22]**

### Scattering

Light inside the polymer can be scattered along its path due to the light reflection and refraction occurring inside the bulk. This phenomenon can cause widening of the power flux distribution compared to the original beam profile. Measuring the power flux distribution after passing the transparent polymer medium is important in order to assess scattering. Scattering was assessed by Potente et al. [23], who measured the power intensity of transmitted laser power through a 5.0 mm thick PP.

Scattering results from van der Vegte et al. [24] (Figure 2-11) show the intensity distribution of the transmitted laser beam for different materials. It can be seen that due to highly scattering nature of PBT, the transmitted laser beam has much wider distribution when compared with PA6 and PA46.

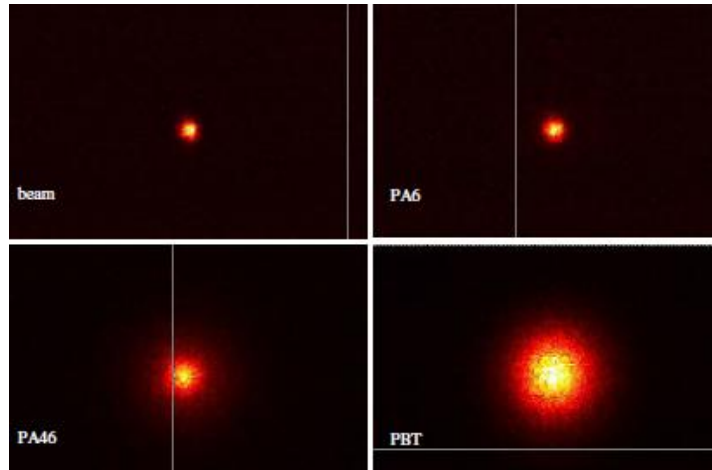


**Figure 2-11 Scattering behavior of different materials in interaction with laser beam [24]**

It is difficult to measure the transmitted power flux distribution using techniques such as knife-edge or pinhole due to overheating of the transparent material during the test [8]. To avoid this issue, Transverse Energy Density Distribution (TEDD) technique has been developed in our research group to determine the beam profile [8].

The TEDD technique involves placing a transparent part approximately 0.3 mm above a second thermoplastic part (not necessarily the same material) that contains a high level (~0.2 wt %) of carbon black. A series of scans are made over the parts at ever increasing powers at a constant scan speed. The width of the melted polymer on the CB part is measured for each scan. This data is used to estimate the power distribution of the scattered beam.

This technique assumes that, for a given scan speed, a certain power flux is required to melt the surface of the absorbing part. As the power is increased, a larger fraction of the scattered beam's width is able to deliver a power flux equal to or greater than this critical value. The width of the melted polymer on the absorbent part will thus increase with power. This basic concept, leads to Equation 2-9:

$$P_k \Psi^*\left(\frac{w_k}{2}\right) = P_0 \Psi^*(0) \quad \text{Equation 2-9}$$

where  $P_k$  is the laser power for a particular scan;  $\Psi^*(w_k/2)$  is the normalized power intensity of the scattered beam at the boundary of molten area at given laser power;  $w_k$  is the measured width of the molten area;  $\Psi^*(0)$  is the normalized power intensity at a the centre of the scattered beam ( $y = 0$ ); and  $P_0$  is the laser power that just caused melting of the absorbing part at  $y = 0$  [8]. This is shown in Figure 2-12, where the ABC line corresponds to the threshold power flux required to just melt the surface of the black part. When  $P = P_k$ , the power flux at point B should equal that at points A and C. Based on the equation 2-10, the normalized power distribution (NPDF) of the scattered beam at different positions  $\Psi^*(w_k/2)$  is equal to the ratio of the scanning power divided by the power at the onset of melting power multiplied by a scaling factor ( $\Psi^*(0)$ ) such that the area under the NPDF curve is unity. This value can be estimated by numerical integration of the distribution data after all the measurements are collected [8].

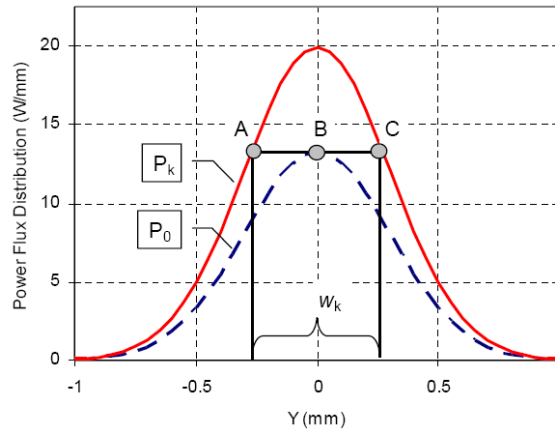


**Figure 2-12 Schematic graph of power flux distribution at different positions of the beam [8]**

The approach described above provides an empirical description of the scattered beam. Chen also presented a model to describe mathematically the beam profile of the scattered light [1]

as a function of the NPDF of the unscattered laser and the properties of the transparent material. In that work, the scattered beam profile was characterized by defining two new parameters: a scattering coefficient ( $\delta$ ) and a scattering standard deviation ( $\sigma$ ). As mentioned above, most high power diode laser beams are a collection of individual micro-beams. When assumed that a fraction ( $\delta$ ) of each micro-beam is scattered as it passes through the transparent part. The power intensity distribution of the scattered light from an individual micro-beam at the exit of the transparent part can be described using a Gaussian distribution having a standard deviation ( $\sigma$ ). The power loss due to absorption also occurs to both the scattered and unscattered fractions of the laser energy as they pass through the transparent part. The spatial distribution of the transmitted power from each micro-beam is summed to calculate the total transmitted power distribution. This is shown in Figure 2-13.

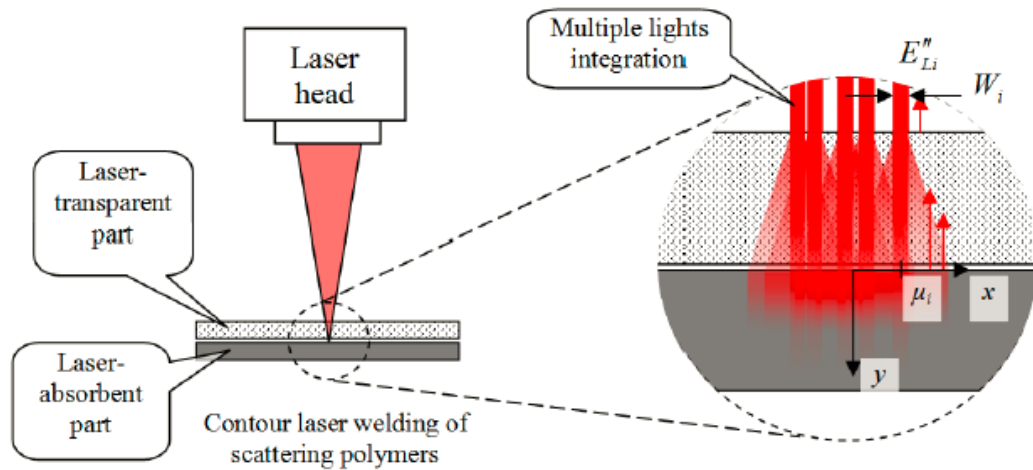


**Figure 2-13 Line energy intensity for the  $i^{\text{th}}$  laser point beam in contour welding [1]**

The non-scattered (direct) light power intensity distribution can be modelled by:

$$E''_{di}(x, y) = \begin{cases} \frac{P_{di}(y)}{v} \frac{1}{W_i} = (1 - \delta(y)) \frac{P_i(y)}{v} \frac{1}{W_i} & x \in ((x_i - \frac{W_i}{2}), (x_i + \frac{W_i}{2})) \\ 0 & x \notin ((x_i - \frac{W_i}{2}), (x_i + \frac{W_i}{2})) \end{cases}$$

where  $E''_{di}(x, y)$  (units of J/m<sup>2</sup>) is the direct light energy intensity from  $i$ -th laser micro-beam passing  $y$ -plane at point  $(x, y)$ ;  $v$  is the laser scan speed;  $W_i$  is the width of  $i$ -th micro-beam; and  $P_i(y)$  is the power of the  $i$ -th laser micro-beam at depth  $y$ . As shown in Equation 2-10, the direct light energy intensity is only effective directly below the  $x$ -position where the laser is shining. Outside this region, the energy intensity distribution provided by the direct light is zero. However, energy intensity distribution provided by the scattered light provides another energy intensity distribution as shown in Equation 2-11 [1]:

$$E''_{si}(x, y) = \delta(y) \frac{P_i(y)}{v} p_y(x - x_i) \quad \text{Equation 2-11}$$

where  $E''_{si}(x, y)$  is the scattered light energy intensity from  $i$ -th laser micro-beam passing through the  $y$ -plane at point  $(x, y)$ ; and  $p_y(x - x_i)$  is the 1-D Gaussian function for light intensity at point  $(x, y)$  in  $x$ -plane. The 1-D Gaussian function at depth  $y$  in  $x$ -plane is defined as [1]:

$$p_y(x - x_i) = \frac{1}{\sqrt{2\pi}\sigma(y)} e^{-\frac{(x-x_i)^2}{2\sigma^2(y)}} \quad \text{Equation 2-12}$$

The total energy density distribution is the sum of the direct and the scattered portions for all the point beams [1]:

$$E''(x, y) = \sum_{i=1}^{\infty} [E''_{di}(x, y) + E''_{si}(x, y)] \quad \text{Equation 2-13}$$

The scattering coefficient ( $\delta$ ) and scattering standard deviation ( $\sigma$ ) were fitted by Chen to experimental data obtained from Transverse Energy Density Distribution (TEDD) technique. More details regarding these two works are provided in Chapter 4.

Several research papers attempted to model the scattering of the laser beam by Lorenz-Mie theory [25] [26] [27] [28] [29] which is an analytical solution of Maxwell equations for the scattering electromagnetic radiation by spherical particles. In this method, several parameters are defined in order to describe scattering behavior of the light for one spherical particle. Two of these parameters are scattering cross section  $C_{sca}$  that gives the probability of photon scattering per unit path-length and normalized phase function  $p(\theta)$  which describes the probability density function for the azimuthal and longitudinal angles by which the scattering direction for the traveling photons is obtained. Knowing these parameters, it would be possible to establish scattering characteristics for a particular medium with a known geometry and particle concentration. The Lorenz-Mie theory is usually followed by Monte-Carlo method in order to demonstrate the scattering behavior of the polymer bulk interacting with a laser beam [25] [26] [27] [28].

## Absorption

Laser absorption is an inevitable phenomenon that occurs in LTW due to polymer's molecular structure. Absorption due to electron transitions  $\alpha_e$  can be defined with Urbach's rule [7]:

$$\alpha_e = A \exp\left(\frac{B}{\lambda}\right) \quad \text{Equation 2-14}$$

where  $A$  and  $B$  are inherent to each molecule and  $\lambda$  is the wavelength. Absorption values are high for the polymers containing aromatic structures. PMMA is a good example of a polymer with high transparency since it does not have any such group that absorbs light.

Ignoring any bulk-reflection effects and scattering, the intensity of the laser power passing through a material, at given depth follows Equation 2-15 [1]:

$$P''(y) = (1 - \eta)P_L'' e^{-K_E y} = P''(0) e^{-K_E y} \quad \text{Equation 2-15}$$

where  $P''(y)$  is the laser light intensity at the depth  $y$ ;  $\eta$  is the surface reflectance of polymer;  $P_L''$  is the intensity of normally incident light from laser head;  $K_E$  is known as the extinction coefficient. This parameter corresponds to the property that causes the extinction of the laser light while passing through the polymer. It consists of two parts:

$$K_E = A + S \quad \text{Equation 2-16}$$

where  $A$  is the laser absorption coefficient and  $S$  is the laser scattering coefficient. When absorption is much larger than the scattering, the extinction coefficient can be interpreted as only the absorption coefficient. Equation 2-15 is known as the Beer-Lambert or Bouguer law and is commonly used in the analysis of light transmission.

Based on the Beer-Lambert law for light transmission, the laser energy loss can be estimated at different depths to be:

$$\left| \frac{dP''(y)}{dy} \right| = (1 - \eta)P_L'' K e^{-K y} = K P''(y) = A P''(y) + S P''(y) \quad \text{Equation 2-17}$$

The generated heat can cause temperature rise at a given depth for both transparent and absorbing parts. Melting can occur depending on the energy intensity and the absorption

coefficient. Additives are often mixed with the base materials in order to increase absorption. Carbon black (CB), for instance, is one of the most common colored pigments used to increase the absorption coefficient. For transparent parts, it is desirable to have a low absorption coefficient in order to minimize energy loss and premature heating of the transparent part.

There have been several studies on absorption of polymers used in LTW. In most of these studies, the absorption is analyzed separately for transparent and absorbing parts. In case of laser transparent parts, transparency is one of the most crucial parameters. Several researchers have examined the transparency and absorption coefficient of amorphous polymers. Haferkamp et al. [30] studied the effect of thickness on various optical properties of different plastics including absorption ratio of PA6, PA6 GF30, PBT and PBT GF30. This study showed that the absorption for PBT using a diode laser ( $\lambda=808$  nm) is less than 5% and does not vary significantly with thickness. What causes the decrease in transmission, however, is the increase in the reflection from 50% in case of 0.5mm plaque, to nearly 80% in case of 2.0 mm plaque of PBT.

Chen has shown that the absorption coefficient of polycarbonate (PC) is negligible [31]. Kagan et al. [32], [33] studied the effect of glass fibres. They found that increasing the glass fibre content results in a higher absorption coefficient and consequently decreased transmission.

Van der Vegte and van Gurp [24] measured the transparency for different engineering plastics (PC, PA6, PA46 and PBT) at thicknesses of 2 mm and 3 mm. The transmission measurements were done in a wavelength range of 400 – 1100 nm with NIR-spectrometer at room temperature. 2-mm thick PBT and PA46 samples had the lowest transparency of approximately 28% at a wavelength of 600 nm. Transparency for PA6 plaques increased from 45% to 65% with increasing the wavelength from 600 to 1100 and, in the case of PC, transparency stayed at constant value of 90% for these wavelengths.

Bates et al. [22] examined the effect of part thickness on transmission for three different PA mXD6 compounds. It was observed that the transmission decreases rapidly with part

thickness for the blends reinforced with glass fibre. Similarly, Kagan et al. [33] investigated the effect of different colored pigments on semi-crystalline materials and determined their transmission at different wavelengths. The transmission decreased by increasing the thickness for different color pigments.

Von Busse et al. [34] investigated the effect of carbon black percentage on heating rate of the absorbing part during laser welding. This study showed that, for all welding variants, the heating rate is highly dependent on the carbon black content. The heating rate increased with increasing the carbon black content. Chen et al. [31] also showed that by adding absorbing elements such as carbon black pigments to PC, the transmission ratio drops exponentially with increasing thickness. The transmission behavior is also dependent on the polymer matrix used.

### 2.2.2 Process Parameters

Beside optical properties, LTW process parameters also have a large influence on the weld quality. Two of the most important process parameters in contour welding are laser power and laser scanning speed.

Chen studied the effect of powers and scanning speeds on the weldability of PC in which the absorbent part contained 0.05% CB. The data are shown in Figure 2-14 [1]. At low powers and high speeds, no material softening was visible. Softening of the absorbing part was observed when the ratio of power ( $P$ ) to speed ( $v$ ) was above a critical level. This ratio is referred to as the line energy ( $LE$ ):

$$LE = \frac{P}{v} \quad \text{Equation 2-18}$$

Several studies have shown that in order to reach to the onset welding, critical line energy is required [1] [11] [22] [35]. As the line energy is increased, the black part starts to melt and the welding process starts. Beyond a certain level, degradation of the polymer at the interface of the transparent and the black part can occur. Further increase of the line energy, not only causes the degradation at the surface of the black part, but may also cause degradation on the transparent side [1].

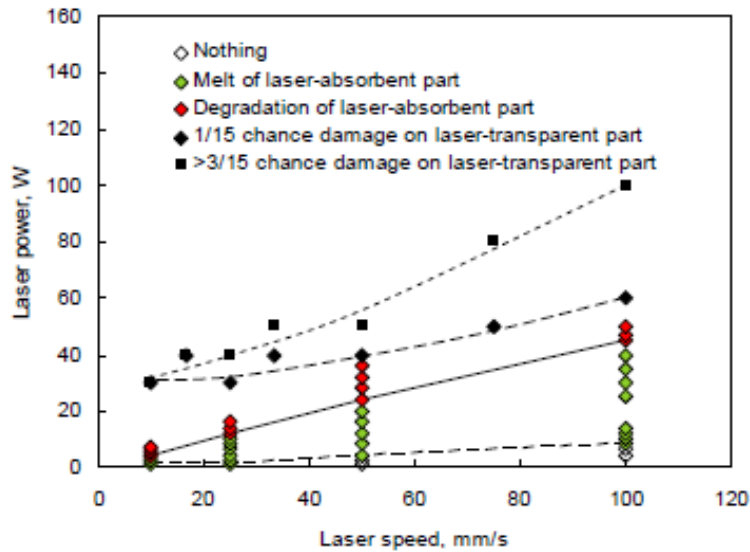


**Figure 2-14 Non-contact method measured LE causing surface damage to laser-transparent part, degradation and melting to laser-absorbent parts for PC with 0.05 wt. % CB [1]**

Weld strength measurement is the most commonly used technique to determine the quality of the weld. There are a number of different types of tests to determine the weld strength, each involving a different geometry. Figure 2-15 shows different welding setups used to measure the weld strength. The issue with the butt joint is the laser energy losses in thick sections of semi-crystalline polymer. Although the interface can be easily irradiated using a T-joint, energy losses occur if the scattered beam width exceeds the thickness of the black part. On the other hand, if the laser beam width at the weld seam is smaller than the width of the black part, the entire

contact area will not be molten. Many researchers have therefore used lap-joints for LTW. Such joints, however, typically do not allow for meltdown to occur [35].

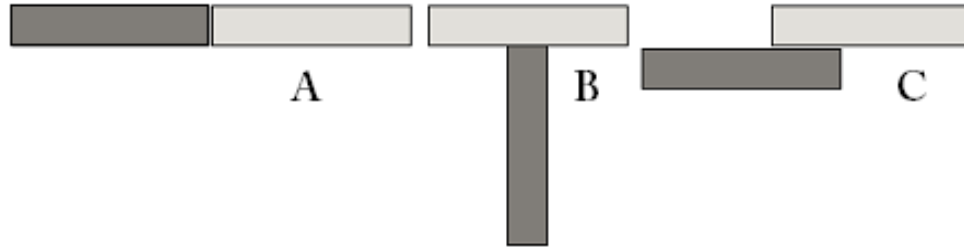


**Figure 2-15 Common joint types A) butt joint, B) T-Like joint , C) lap joint**

Chen [31] studied the effect of line energy on the weld strength of assemblies consisting of PC, PA6 and PA6GF with different CB levels for the absorbing part. This study showed that, above a certain line energy, the weld strength starts to decline. The results in this study agree with the weld strength measurement in other publications ( [11], [15], [22], [33], [36]). Typical results are shown in Figure 2-16.

The line energy values required for welding generally differ from one material to another. This is because the energy arriving at the weld interface varies in different materials because of their optical properties.

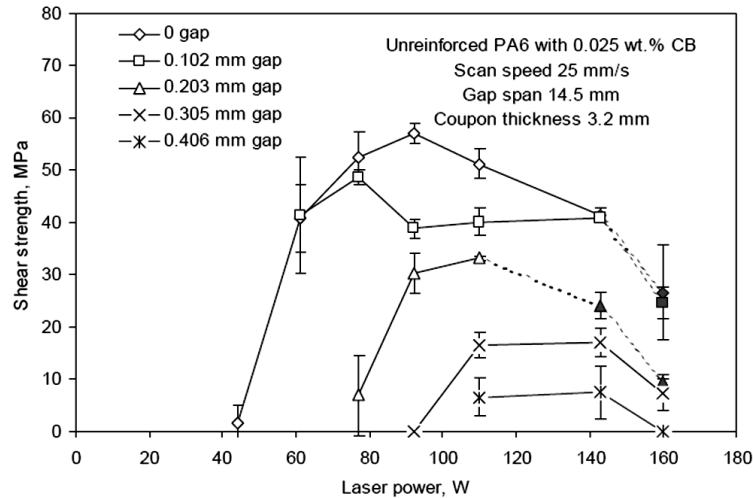


**Figure 2-16 Weld shear strength vs. laser scan power for different gap dimensions for 0.025% CB [1]**

Highly scattering materials, not only back-reflect more energy, but also increase the path length of the laser inside the bulk due to scattering, which significantly increases absorption. Scattering also causes the beam to widen, which in turn reduces the energy flux at the weld interface.

Grewell et al. [37] observed the effect of travel speed, power density and pressure on weld line width, consistency and strength for narrow weld joints (~100  $\mu\text{m}$  wide) of PC and PS polymers. During this study, it was noticed that, below a critical power level, the plastic sample under the laser beam starts to locally deform and then recovers by the time laser beam leaves the deformed zone. This effect is believed to be due to thermal expansion from heating by the laser followed by cooling.

The line energy is a useful tool to assess weld quality at different speeds and powers. However it also has some practical limitations. In case of low powers, low speeds would be required for welding. Low speeds will decrease the total irradiation to the point that energy losses due to conduction may be a significant fraction of the delivered energy. However,

experimental evidence suggests that it is a reasonable scaling parameter for laser speeds above 600 mm/min [1].

### **2.2.3 Modeling**

Weld quality is dependent on the temperature-time profile in the material – particularly at the interface. This is in turn related to: (i) physical and optical properties of the transparent and the absorbing parts, (ii) part geometry such as thickness, and (iii) process parameters such as laser power and scanning speed. Therefore, temperature distribution prediction at different positions on both parts is one of the key research areas in LTW.

Modeling can be grouped into analytical, finite difference, and finite element categories. Accuracy of the results mainly depends on the conditions applied in order to simplify the general differential equation for heat conduction. Therefore the key factor in modeling the thermal behavior is to provide good estimations of different boundary conditions, thermal and optical properties of the materials, and laser beam distribution during the process.

Chen [1] predicted the one-dimensional temperature distribution as a function of depth  $y$  for a given value of absorption coefficient just at the end of the heating phase. The proposed analytical model calculated the temperature rise of the laser-absorbent plaque around the weld interface for a non-contact method. He also presented a 3-D finite element model that simulated the heat transfer in contour laser transmission welding of PC, PA6, and PA6GF. The power required for the onset of welding and weld-line width was reasonably predicted. However, these models ended up significantly overestimating the temperature near the incident surface of the transparent part. The reason is due to under-estimation of the volume inside the transparent part in which the laser energy is absorbed. Although the amount of the absorbed energy can be calculated, the volume in which this energy is absorbed is not accurately known due to our poor understanding of scattering [38].

Speka et al. [39] presented a model to determine the temperature distribution in both transparent and absorbing parts made of PMMA-ABS/PC. The experimental temperature profiles were measured by IR thermography and were then compared with numerical simulations during heating and cooling phases modeled by COMSOL. Since the transparent material was amorphous, the bulk scattering effect was neglected. The extinction of the light was assumed to follow the Beer Lambert law. The model demonstrated a good agreement with the experimental data during the heating phase.

Geiger et al, [40] used a finite element model to estimate the temperature fields during laser transmission welding of plastics. The optical properties of materials such as PC, PA6, PP, and POM were experimentally calculated. The influence of the optical properties for both filled and unfilled material on the molten pool geometry was analyzed. The change in absorption coefficient due to temperature variation for unfilled material was reported to have a negligible influence on the formation of the molten pool geometry.

Mayboudi et al. [41] presented a 3-D thermal model for laser transmission welding of a PA6 lap joint with a moving laser beam. The distinction of this work compared to previous studies was that the complete 3-D beam profile was modeled including the effect of laser beam scattering by the transparent part.

## Chapter 3

### Material

#### 3.1 Review of Polyesters

The thermal behavior of a material plays a major role in laser transmission welding. Polymers can be divided into two major groups based on their thermal behaviors: thermosets and thermoplastics. Thermosets are polymers whose individual chains have been chemically linked by covalent bonds during polymerization or by subsequent chemical or thermal treatment during fabrication. This results in a network of cross-linked polymer chains. These links give the thermosets resistance against thermal softening, creep and solvent attack but these polymers cannot be thermally processed. For this reason, the thermosets cannot be used in welding [42] .

On the other hand, thermoplastics can be heat-softened. These materials can be recovered and re-melted by the application of heat and pressure. Amorphous thermoplastics consist of intertwined carbon chains. The binding forces are due to van der Waals and hydrogen-bond forces between molecules and mechanical entanglement between the carbon chains. These thermoplastics start to soften by temperature rise since the heat provides the energy for the chains to reach to higher entropy level. Semi-crystalline thermoplastics have a crystalline structure in the bulk of amorphous intertwined carbon chains. The existence of the crystalline structure causes the thermoplastic to stay more resistant to temperature. Therefore, unlike amorphous type, they start to melt above a certain temperature threshold known as the melting temperature.

Polyesters are thermoplastics with the ester functional group in their backbone [43]. The polyesters that find commercial applications are mostly linear except for some specially prepared branched polymers used in the preparation of polyurethanes. Linear polyesters became commercially important materials early in this century and still find many uses in industry.

Aromatic diacids and/or glycols with aromatic rings in the structures, yield polyesters with high melting and glass transition temperatures; while the aliphatic ones yield low melting solids or viscous liquids [43].

Although there are many types of polyesters, the term “polyester” as a specific material most commonly refers to polyethylene terephthalate (PET). This category of materials can be either found naturally, such as in the cutin of plant cuticles, or found in synthetics produced through step-growth polymerization. Natural polyesters and a few synthetic ones are biodegradable, but most synthetic polyesters are not [42].

The traditional route in the production of commercial PET is through two successive ester interchange reactions, as shown in the Figure 3-1. The first step (Figure 3-1.A) is the ester interchange of dimethyl terephthalate (DMT) and ethylene glycol at temperatures near 200°C during which methanol is removed and an oligomeric product (n=1-4) is obtained. In the second-stage esterification (Figure 3-2.B), increasing temperature causes the formation of high-molecular-weight PET during which ethylene glycol is distilled off [42].

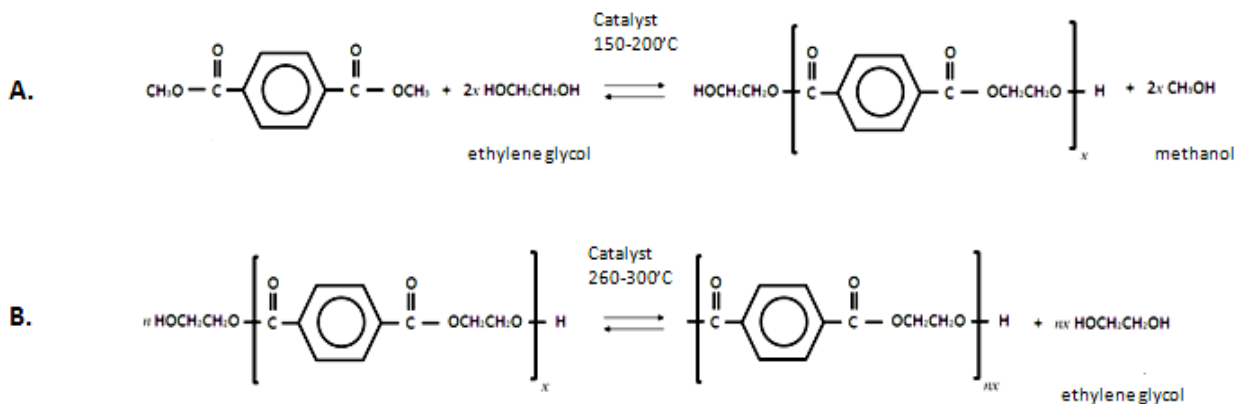


**Figure 3-1 Two steps in polymerization of poly (ethylene Terephthalate): A. Ester interchange of dimethyl terephthalic acid and ethylene glycol B. High-temperature esterification to yield high-molecular-weight polymer and ethylene glycol as a by-product [42]**

The other polyester of the same family is poly (butylene terephthalate) (PBT). This polymer is quite similar to polyethylene terephthalate (PET) structure wise. The only difference is the

number of the methylene ( $CH_2$ ) groups present in the repeat units of the molecule. PBT can be synthetically produced by either polymerization of butanediol and terephthalic acid or transesterification process of dimethyl terephthalate (DMT) as shown in Figure 3-2 [44].

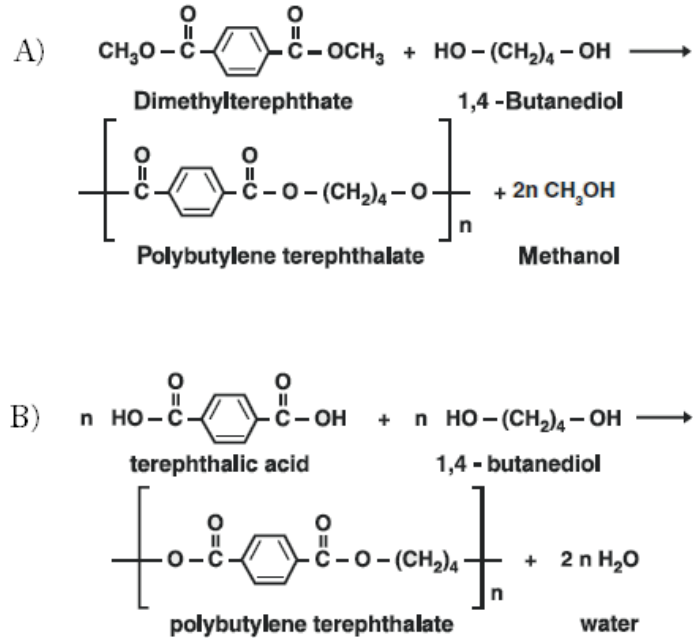


**Figure 3-2 PBT production processes A) DMT trans-esterification B) PTA polymerization**

The polymers with slow rate of crystallization such as PET are widely used as a textile fiber. Modified grades of PET have allowed this polyester to penetrate the beverage bottle market as well as other molding applications. In the non-bottle market, PET is in competition with poly(butylene terephthalate) (PBT). Principal applications for PBT include injection-molded parts for electrical and electronic use and for automotive markets. Both polyesters are moisture sensitive (hydrolytic instability), but have high strength, rigidity and toughness, excellent dimensional stability, low coefficient of friction, abrasion resistance, and good resistance to chemicals and grease.

Studies show that the half-time of crystallization for PET is 7-11 times longer than that for PBT [45]. Therefore, PET tends to crystallize more slowly than PBT. The reason for this is that the four-methylene groups in PBT lead to a quicker arraying of the molecular chains into folded state at a higher temperature in the cooling process than PET [46]. The higher crystalline content in PBT compared to PET, can lead to more light scattering as discussed in section 2.2.1. The hypothesis being tested in this research is whether blending of more amorphous PET into a PBT matrix will increase laser transparency and reduce scattering compared to the unblended PBT. These two materials are also melt-miscible and susceptible to trans-esterification. This phenomenon is related to the PBT/PET ratio and the time-temperature history of the material during molding and to some degree, during compounding and welding [47]. Due to time constraints, this trans-esterification effect was not studied during this research.

### **3.2 Materials Used in This Study**

Three different blends of nucleated PBT (Arnite® T) and PET (Arnite® A) were used in this research with PET as the dispersed phase. The experimented blends were 100/0, 90/10 and 75/25 ratios of PBT/PET. In order to perform laser welding trials, all blends were made in unpigmented versions and versions containing 0.1 weight % of carbon black. The latter materials were provided for use as the absorbent part of an LTW assembly. All materials were manufactured by DSM of the Netherlands and provided to the researchers as pellets in 25kg bags. As recommended by the company, all the materials were dried for 6 hours at 110°C before injection molding.

### 3.3 Plate Manufacturing

The three polyester blends were injection molded at Royal Military College using a 55-ton Engel injection-molder. Information on injection molding can be found in the brochure provided by the company [42]. The natural and CB-pigmented materials were injection molded into plaques having nominal thicknesses of 2 and 3 mm as shown schematically in Figure 3-3. The injection molding conditions were provided by DSM [48] and are given in Table 3-1. As recommended, since PET is in the dispersed phase of the blend, the temperature profile for injection molding of PBT was used in the process.

**Table 3-1 Temperature distribution at different positions of the injection molder for PBT (Arnite T) and PET (Arnite A) [48]**

Temperature at :	Mold [°C]	Melt [°C]	Nozzle [°C]	Front [°C]	Center [°C]	Rear [°C]
Arnite A	130-140	270-290	270-280	270-285	270-290	270-290
Arnite T	80-100	240-270	240-260	240-260	230-250	230-240

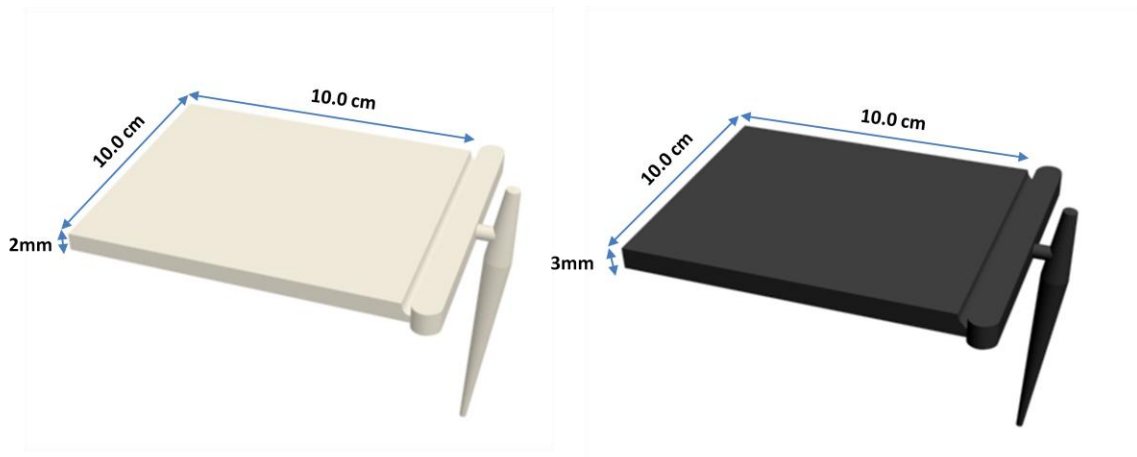


**Figure 3-3 Dimensions of the transparent part (left) and the absorbing part (right) made by injection molding**

In order to perform the laser welding trials, each plate was cut into 3 geometrically similar smaller plates with dimensions of 2.5 cm × 10.0 cm × 2 mm for the transparent parts and 2.5 cm × 10.0 cm × 3 mm for the absorbing parts.

### 3.4 Material Properties

#### 3.4.1 Thermal Properties

The heat capacities for three blends of PBT/PET with ratios of 100/0, 90/10 and 75/25 were measured by Modulated Differential Scanning Calorimetry (MDSC) using a DSC Q100 V9.9 manufactured by TA Instruments. The heat capacities (*c*) were measured over a range of temperatures between 20°C to 275°C. 275°C is 50°C above the melting temperature of PBT, and 25°C above the melting temperature of PET. The results are shown in Figure 3-4. Heat capacity and latent heat data from this figure are summarized in Table 3-2.

**Table 3-2 Thermal properties of the blends based on DSC studies**

Property	Units	PBT/PET (100/0)	PBT/PET (90/10)	PBT/PET (75/25)
<i>c</i> at 25°C	J/g K	1.5	1.3	1.3
<i>c</i> at 265°C	J/g K	2.3	2.2	2.0
Melting point of PBT phase	°C	226.0	225.0	223.9
Enthalpy of melting of PBT	J/g	45.6	38.1	27.2
Melting point of PET phase	°C	-	253.9	257.6
Enthalpy of melting of PET	J/g	-	5.2	16.3

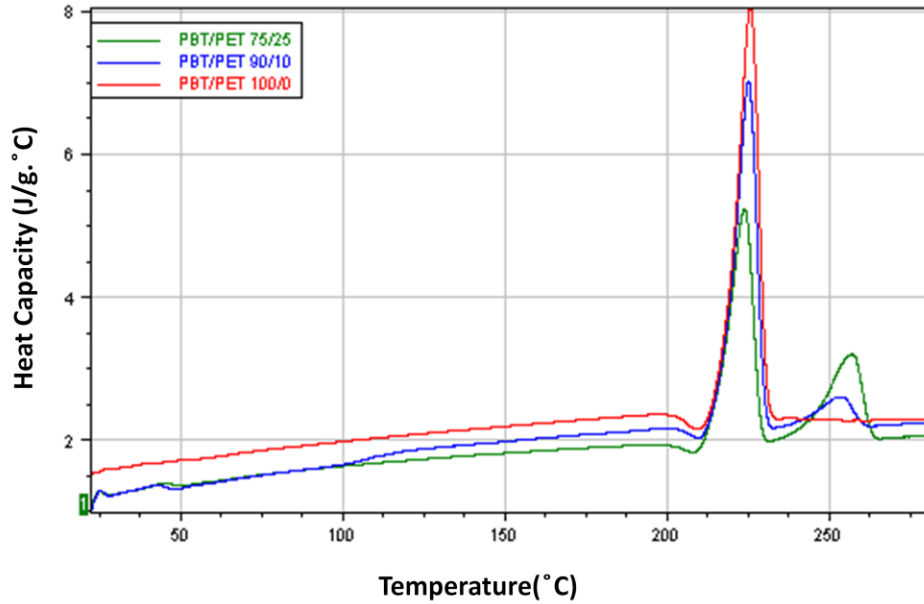


**Figure 3-4 Heat capacity variation at different temperatures from MDSC for three blends**

As shown in Figure 3-4, for the blends containing PET, two melting peaks are observed. The first one corresponds to melting of the PBT fraction and the second one, which occurs around 255°C, corresponds to melting of the PET component. The results achieved from experimental studies agree with the values from the literature review as shown in Table 3-3.

### 3.4.2 Physical Properties

Table 3-3 summarizes the physical properties of unreinforced PBT and PET. This data will be used later for thermal modeling. Additional information is found in Appendix A.

**Table 3-3 General properties of base polymers PBT and PET**

Properties	Units	PBT	PET	Data source
Heat Capacity of Melt	(J/kg.K)	2260	2050	[49]
Thermal Conductivity of Melt	(W/m.K)	0.109	0.24	[49]
Density	(kg/m <sup>3</sup> )	1300-1320	1380-1400	[49]
Average Thermal Expansion	( $\mu\text{m}/\text{m}^\circ\text{C}$ )	80	70	[50]
Melting point	( $^\circ\text{C}$ )	225	250	[49]
Efficient Thermal Diffusivity	(m <sup>2</sup> /s)	$4.65 \times 10^{-8}$	$4.22 \times 10^{-8}$	[49]

### 3.4.3 Degradation Analysis from TGA Test

Thermal Gravimetric Analysis (TGA) was performed for PBT/PET blends of 100/0, 90/10 and 75/25 on TA Instruments 2050 TGA located at Queen's University to determine the temperature at which the material degrades. The degradation results were used in the degradation model (described in Chapter 7). In the TGA test, the samples were cut into small specimens on the order of 5 mgr and were heated from the room temperature to 600°C at a heating rate of 10°C/min for all blends. The type of the purge plays a major role on the type of decomposition. Inert purge gases such as helium, nitrogen, and argon are suitable for determining purely thermal decomposition (pyrolysis). In these experiments, nitrogen was used as the purge gas during the experiment with purge flow rate of 60ml/min.

Figure 3-4 shows the mass of the sample relative to the initial mass as a function of temperature for the three blends. The figure has been cropped in order to magnify the mass

degradation of the samples. None of the three blends show any significant degradation until 360°C. By 500°C, nearly 90% of all the mass had degraded. The results indicate that the degradation rate for PBT is faster than for the blended materials. The degradation process becomes slower as the percentage of the PET in the blend increases.

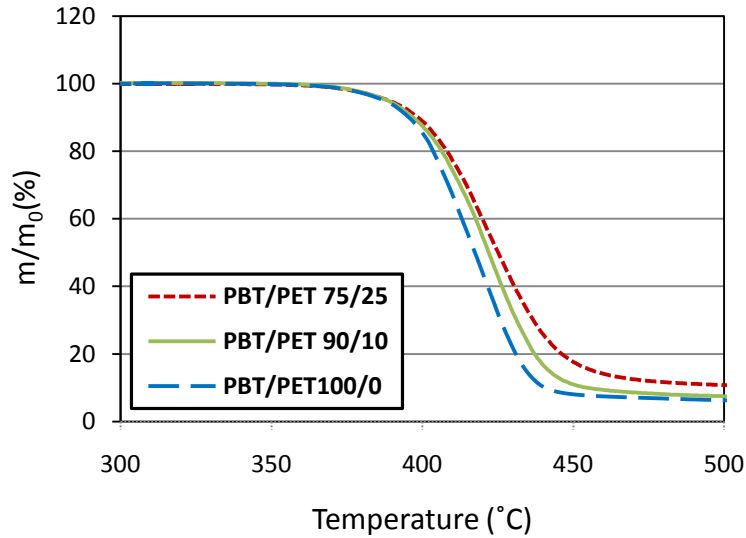


**Figure 3-5 Degradation analysis of three blends of PBT/PET**

### 3.4.4 Optical Properties

In this section, the optical properties of the materials are investigated. These properties include total transmission ( $T_T$ ), total reflectance ( $R_T$ ) and absorption coefficient for both transparent and the absorbing part. These tests were performed at the Department of National Defense's Quality Engineering Test Establishment in Ottawa using a Cary 5000 UV-Vis-NIR spectrophotometer by James Sauve from University of Ottawa.

## Reflection

In order to measure the total reflectance of the samples, an integrating sphere is used in reflectance mode as shown in Figure 3-6. Unlike the total transmission measurement, the beam is emitted through the sphere and hits the sample. The reflected beams are themselves reflected off the sphere until they are absorbed by the sensor.

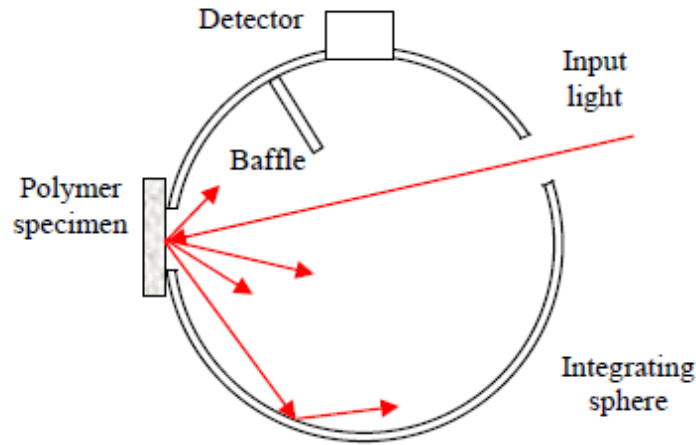


**Figure 3-6 Spectrophotometer measurement of total reflectance of polymer [1]**

The total reflectance of the sample is defined as:

$$R_T = \frac{P_{ref}}{P_{in}} \quad \text{Equation 3-1}$$

where  $P_{ref}$  is the reflected power absorbed by the sensor. The total reflectance in this study contains both the surface reflection and also the bulk reflection. Figure 3-7 shows the total reflectance values for different blends. The vertical dashed line in this and other similar figures corresponds to the wavelength of the diode laser (940nm) used in this research.

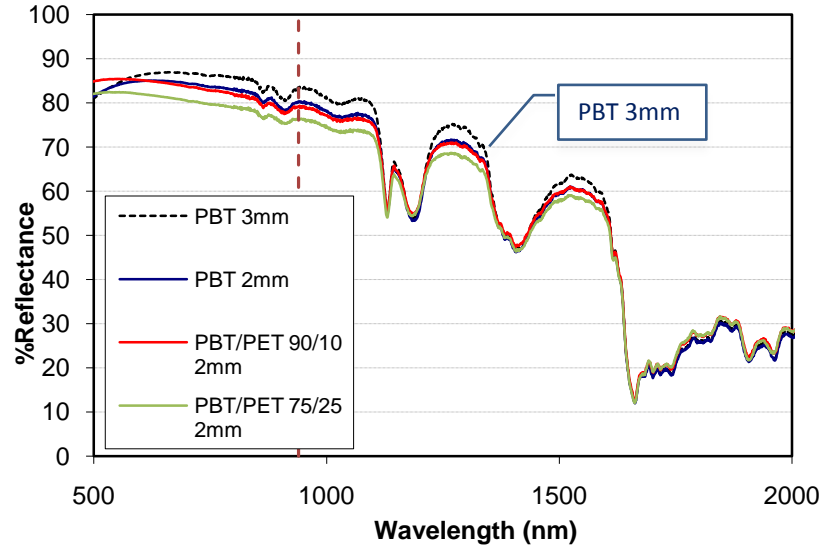


**Figure 3-7 Reflectance ratio at different wavelengths for three blends of PBT/PET 100/0, 90/10, 75/25**

According to Figure 3-7, the reflectance ratio at the diode laser wavelength is 76-83% for the materials and thickness used in this study. The reflectance for the three materials is summarized in Table 3-4. The results shown in this figure indicate that, by increasing the thickness of the transparent part by 1 mm, the total reflectance ratio increases from 80% to 83%. This can be attributed to bulk reflection described in 2.2.1. The reflectance decreases by adding more amorphous PET to the blend.

**Table 3-4 Reflectance values for 2mm plaques**

PBT/PET Ratio	Reflectance (%)
100/0	80.2
90/10	79.1
75/25	78.8

## Transmission

In order to measure the total transmission of the blends, the spectrophotometer was operated in transmission mode as shown schematically in Figure 3-8. As can be seen, a beam is emitted and passes through the specimen held at the entrance of the sphere. A portion of the light that passes through the sample enters a reflective sphere and ultimately gets absorbed by the detector.

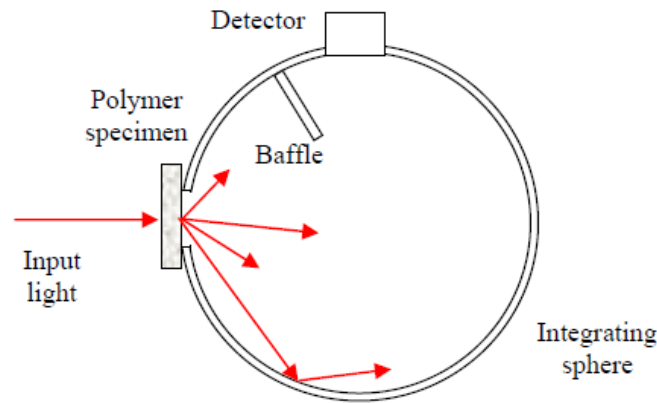


**Figure 3-8 Schematic view of the integrating sphere used in order to measure transmission for samples for various wavelengths [1]**

The transmittance is defined by Equation 3-2:

$$T_T = \frac{P_{out}}{P_{in}} \quad \text{Equation 3-2}$$

where  $P_{out}$  is the power of the laser light that passes through the sample and  $P_{in}$  is the measured laser incident power in the absence of the sample. Figure 3-9 shows the transmittance results for tests conducted on the PBT/PET blends. The vertical dashed line in this figure corresponds to the desired wavelength (940nm) used in latter studies.

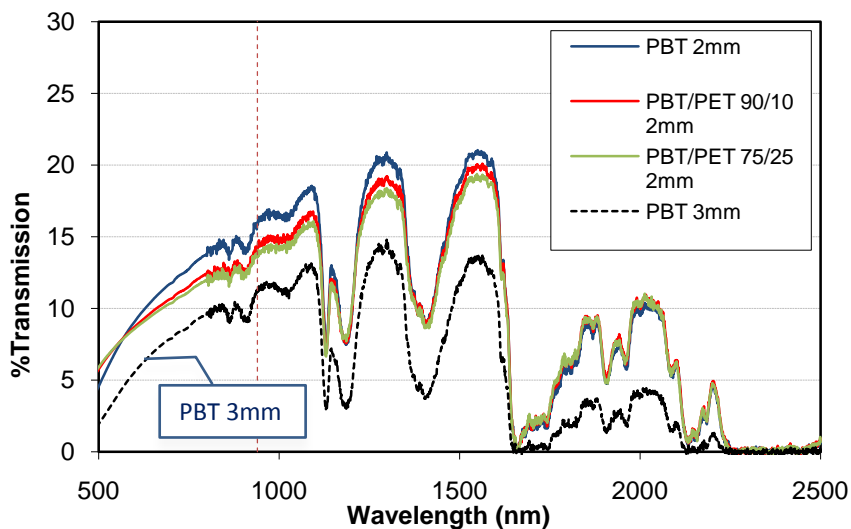


**Figure 3-9 Transmission ratio at different wavelengths for three blends of PBT/PET 100/0, 90/10, 75/25**

The laser used for the experimental studies in this work is a diode laser with wavelength of 940 nm. Based on the results from the total transmission analysis, adding more PET to the blend decreases the total transmission for this specific wavelength, from 16.0% to 13.9% for the 2mm plaques studied. The results are summarized in Table 3-5. The data shows that transmittance for these materials is approximately 10-20%, which is considerably smaller than other materials such as PC (89%), PA6 (64%) or PA46 (37%) [24]. High surface and bulk reflection ratio of the blends, due to the difference in refractive indices between the amorphous and crystalline phases, is likely the reason for this difference.

**Table 3-5 Transmission for 2 mm thick plaques**

PBT/PET Ratio	Transmission (%)
100/0	16.0
90/10	14.0
75/25	13.9

## Absorption

Based on the total transmittance and reflectance data, the total absorption can be calculated using Equation 2-5. It is shown in Figure 3-10. The vertical dashed line in this figure corresponds to the desired wavelength (940nm) used in latter studies.

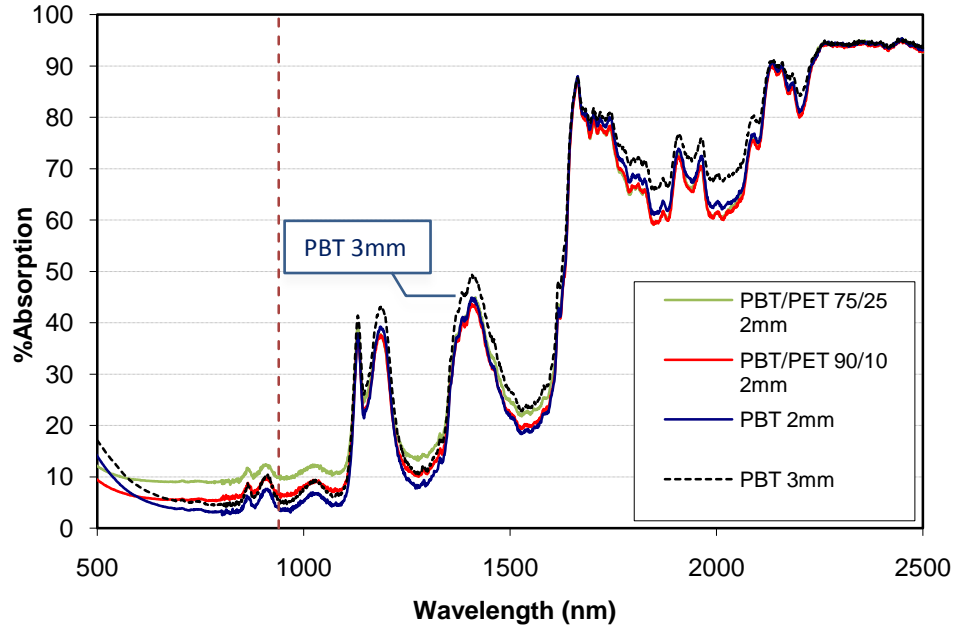


**Figure 3-10 Absorption ratio at different wavelengths for three blends of PBT/PET 100/0, 90/10, 75/25**

In the infrared part of the light spectrum, polymers exhibit selective absorbance as a function of wavelength. The infrared absorption in semi-crystalline polymers also provides information about the crystallinity since the ordered regions give different absorption bands due to differences in conformations [16]. According to Figure 3-10, the absorption ratio for PBT/PET 75/25 is slightly larger than PBT/PET 90/10 and PBT/PET 100/0 at the laser wavelength. This may be due to the higher absorption of PET due to its higher aromatic content (Equation 2-16) or may be due to increased side-scattering of blends containing high levels of PET; the latter results in a longer light path length and higher absorption.

## Chapter 4

### Assessment of Laser Beam Scattering

#### 4.1 Introduction

As discussed earlier once the laser beam starts to pass through the transparent part, the power per unit area changes due to scattering. This chapter describes the technique used to measure the power profile of the scattered beam after transmission through the transparent part. The experiments were conducted using a Rofin-Sinar DLx16 continuous wave 160 W diode laser (wavelength 940nm) and UW200 workstation which is shown in Figure 4-1.



**Figure 4-1 Rofin-Sinar DLx16 HP diode laser and welding fixture in UW200 Workstation [41]**

The motion system inside the workstation allows the sample to move in a 2-D X-Z plane at a maximum speed of 9000 mm/min. In this study, the samples traveled along the Z axis in order to determine the beam profile along the X axis. The laser head can move vertically along the Y axis in order to position the focal point on the desired plane. The pressure to press the

pieces together is provided by a pneumatically actuated fixture located on the motion system and is shown in Figure 4-1.

#### 4.2 Equipment/Method

The technique for measuring the power profile of the laser beam after transmission through the transparent part was developed by Zak et al. [8]. It is based on the relatively low thermal conductivity of thermoplastics and the relatively fast heating caused by the rapidly moving laser beam. It assumes that the local heat loss due to conduction will be negligible during the short interaction time with the laser beam and therefore there is a threshold amount of energy which must be delivered to the surface of the laser-absorbent part at any point heated by the laser beam in order for melting to take place.

As can be seen in the Figure 4-2, the laser-transparent part (L-Tr part) is separated from the laser-absorbent part (L-Ab part) which is PA6 containing 0.2 wt% CB, by parallel 0.3 mm thick metal shims to avoid contact between the parts after heating.

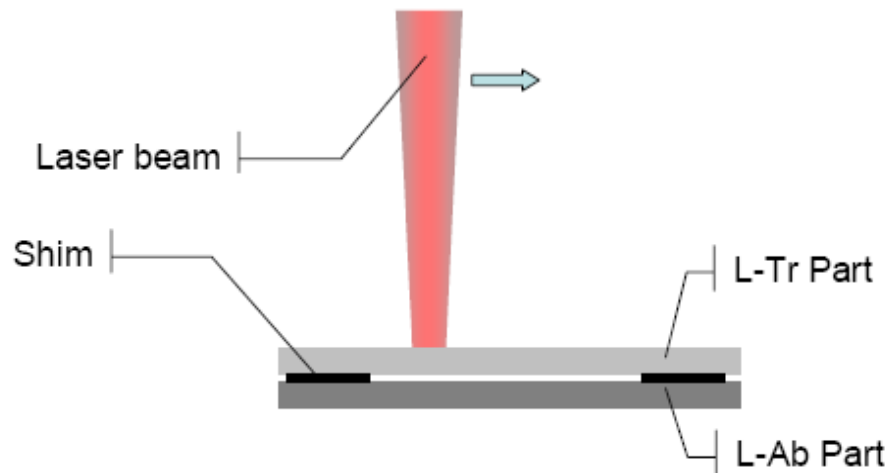


**Figure 4-2 Schematic view of laser scanning over the transparent part on a non-contact method [8]**

In this technique, the parts are exposed to a laser beam traversing at a constant speed (1000 mm/min in this case). The laser beam begins to scan over the transparent part, starting at a low power. After each scan, the laser power is increased incrementally and a new area is scanned. Initially, no melting is observed on the laser-absorbent part. Eventually, a threshold power is reached at which the first marks of melting are observed on the laser-absorbent part. This power is denoted as  $P_0$ . As the power is increased on subsequent scans, the width of the area that has melted on the laser-absorbent part increases. This is shown in Figure 4-3. For each power setting ( $P_k$ ), the width of the melted area ( $w_k$ ) on the laser-absorbent part is measured.

The reason for this change in width with power is the unevenly distributed power across the beam scan direction due to scattering. If the laser power was evenly distributed, the melt width would not be expected to change with laser power. However, the scattered transmitted light follows a Gaussian-like distribution where the maximum power intensity is located at the centre of the beam. By increasing the laser power, a greater fraction of this distribution, reaches the threshold energy in order to melt the surface of the absorbing part.

Figure 4-3 shows typical data for PBT/PET 75/25. The variation in width for a given scan line is attributed to variations in part thickness. Local increases in thickness cause more scattering of the laser light and a more narrow line. The thickness variations are believed to have been caused by the mould insert that did not sit completely flat inside in the mould cavity. The weld width was thus measured at 16 locations every five millimeters along the scanned line.

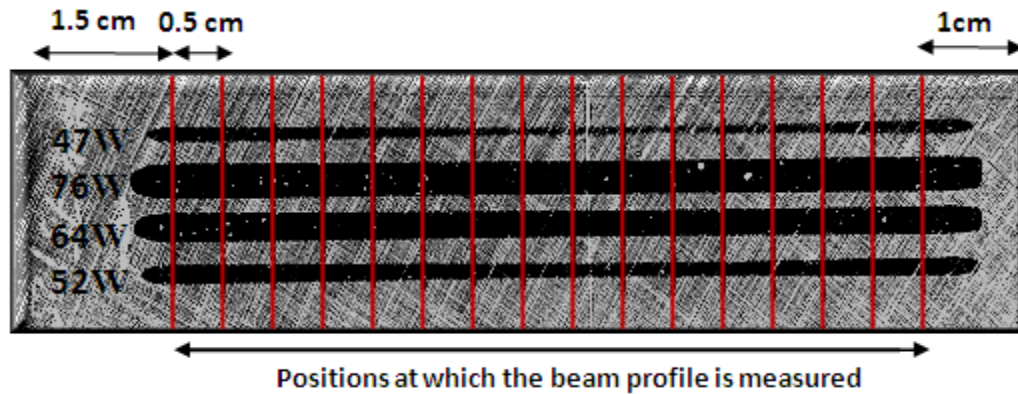


**Figure 4-3 Melt lines after laser scanning over the absorbing part for PBT/PET 75/25**

The plates were scanned optically on a flat-bed scanner at a high resolution (1200 dpi) and the line width ( $w_k$ ) measured at each of the 16 positions and for each power ( $P_k$  where  $k=1$  to  $n$ ).

In order to melt the surface of the absorbent part, a critical line energy intensity (or energy flux) is required. At this melting threshold, the critical line energy intensity at  $x=0$  is:

$$E''(0) = \frac{K_T P_0 \Psi^*(0)}{\nu} \quad \text{Equation 4-1}$$

where  $K_T$  is the transmittance (see section 2.2.1),  $P_0$  is the total applied power and is known as threshold power;  $\nu$  is the scanning speed of the laser; and  $\Psi^*(0)$  is the Transverse Normalized Power Flux Distribution (T-NPFD) at the centre of the beam and the weld interface ( $x=0$ ). For other powers ( $P_k$ ), the energy intensity at the edge of melted line ( $E''(w_k/2)$ ) must be equal to the critical energy intensity value ( $E''(0)$ ). Thus:

$$\frac{P_0}{P_k} \Psi^*(0) = \Psi^*\left(\frac{w_k}{2}\right) \quad \text{Equation 4-2}$$

The value for  $\Psi^*(0)$  plays the role of a scaling factor. It can be calculated from the area underneath  $P_0/P_k$  vs.  $w_k/2$  curve in the interval  $w_k/2=0$  to  $w_k/2=\infty$ . From this, the T-NPFD at any position  $\Psi^*(w_k/2)$  can be calculated from Equation 4-2. The difficulty is in reaching the lower ends of  $P_0/P_k$  vs.  $w_k/2$  curve in order to estimate  $\Psi^*(0)$ . This requires higher operating powers in order to measure this parameter accurately. As explained in Chapter 2, Chen's model (Equation 2-15) is able to describe the scattered beam profile of the laser beam passing through the polymer bulk by a summation of scattered and unscattered contributions from the discretized input beam from the laser. This model divided the line energy intensity received by the absorbent part into direct and scattered line energy intensity. Therefore:

$$E''\left(\frac{w_k}{2}\right) = \sum_{i=1}^{\infty} \left[ E''_{di}\left(\frac{w_k}{2}\right) + E''_{si}\left(\frac{w_k}{2}\right) \right] = \frac{K_T P_0 \Psi^*(0)}{\nu} \quad \text{Equation 4-3}$$

where  $E''_{di}(w_k/2)$ , is the line energy intensity received by the absorbent part by the direct portion of the  $i$ -th laser beam; and  $E''_{si}(w_k/2)$  is the line energy intensity received by the absorbent part by the scattered portion of the  $i$ -th laser beam. These last two terms are summed over the number of small discretized laser beams. The direct light intensity has a non-zero value inside the boundaries of the laser beam and zero value outside of the boundary:

Equation 4-4

$$E''_{di}(x) = \begin{cases} \frac{P_{di}}{\nu} \frac{1}{W_i} = (1-\delta) \frac{K_T P_i}{\nu} \frac{1}{W_i} & x \in \left( (x_i - \frac{W_i}{2}), (x_i + \frac{W_i}{2}) \right) \\ 0 & x \notin \left( (x_i - \frac{W_i}{2}), (x_i + \frac{W_i}{2}) \right) \end{cases}$$

where  $W_i$  is the width of  $i$ -th discretized beam;  $\delta$  is defined as the ratio of the scattered power to the total power of the beam at the interface and  $P_i$  is the laser power of  $i$ -th discretized beam before transmission. The scattered light intensity is also described as:

Equation 4-5

$$\begin{aligned} E''_{si}(x) &= \frac{1}{v} \int_{-\infty}^{+\infty} P''_{si}(x, z) dz = \frac{P_{si}}{v} \int_{-\infty}^{+\infty} p_0((x - x_i), (z - z_i)) dz \\ &= \delta \frac{K_T P_i}{v} p_0(x - x_i) = \delta \frac{K_T P_i}{v} \frac{1}{\sqrt{2\pi}\sigma} e^{-\frac{(x-x_i)^2}{2\sigma^2}} \end{aligned}$$

where  $p_0(x - x_i)$  is a 1-D Gaussian function that corresponds to the power distribution of  $i$ -th beam with scattering standard deviation of  $\sigma$ . By combining Equations 4-4 and 4-5 with Equation 4-3, one obtains:

Equation 4-6

$$E''(x) = \sum (1 - \delta) \frac{K_T P_i}{v} \frac{1}{W_i} + \sum \delta \frac{K_T P_i}{v} p_0(x - x_i) = \frac{K_T P_0 \Psi^*(0)}{v}$$

Equation 4-6 can be rewritten as:

$$\frac{P_k}{P_0} \frac{1}{\Psi^*(0)} \left[ (1 - \delta) \Psi\left(\frac{w_k}{2}\right) + \sum \delta \Psi(x_i) W_i p_0\left(\frac{w_k}{2} - x_i\right) \right] = 1 \quad \text{Equation 4-7}$$

Equation 4-7 is used to describe the beam profile. The parameters  $\Psi^*(0)$ ,  $\delta$  and  $\sigma$  in equation 4-7 were fitted to experimental data using a MATLAB code found in Appendix B. Inputs to the model consisted of:  $P_0$ ,  $P_k$ - $w_k$  pairs, the T-NPDF of the unscattered laser beam  $\Psi(w_k/2)$  as well as the width of the discretized beam segment ( $W_i$ ).

### 4.3 Results/Discussion

The threshold powers ( $P_0$ ) were measured at the locations shown in Figure 4-3 and plotted in Figure 4-4. It can be seen that the threshold power is consistently highest towards the middle of the plaque and lowest towards the edge. This might suggest that the middle of the plaque requires more energy in order to melt the surface. This may be attributed to variation of part thickness across the plaque.

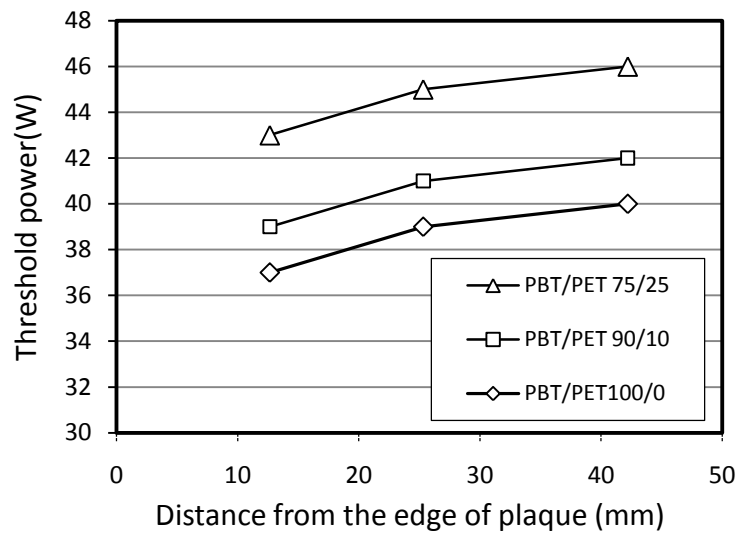


**Figure 4-4 Threshold power variation in three different locations along the scanning direction for PBT/PET 100/0, 90/10 and 75/25**

Figure 4-5 shows the thickness distribution for the transparent parts made of PBT/PET 100/0, PBT/PET 90/10 and PBT/PET 75/25. The thickness is seen to be greater in the middle of the plaque than near the edges. The uneven thickness of the plates is attributed to the 4 mm mould insert that was placed in the mould cavity in order to reduce the cavity depth from 6 mm to 2 mm; it is conjectured that it did not sit completely flat inside in the mould cavity.

According to the results shown in Figure 4-4 and Figure 4-5 it can be concluded that the threshold power increases with thickness. This is attributed to the energy loss due to absorption and bulk reflection as described in 3.4.3.

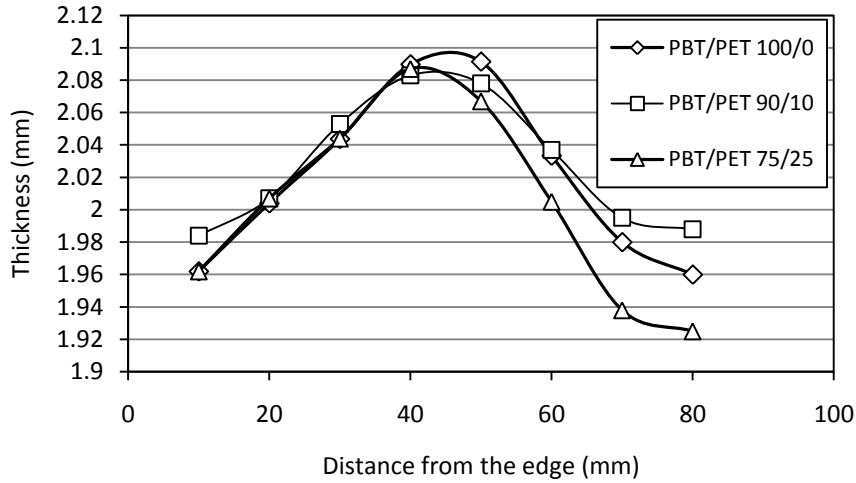


**Figure 4-5 Thickness distribution for the transparent part with nominal dimensions of 2.5 cm × 10 cm × 2 mm**

It is also interesting to note that the threshold power increases with the amount of PET in the blend. There may be two reasons for this. One is the transmittance ratio difference between the blends containing PET as shown in Figure 3-9. Therefore, less power is transmitted to the surface of the absorbing part. As described in section 3.4.4, The transmission ratio for PBT/PET 75/25 is 2.1% less than the 16.0% ratio which is reported for PBT/PET 100/0. This difference in transmission is consistent with measured threshold powers. The other reason is the transmitted flux received at the weld interface. The received flux may be lower in the blends containing PET due to the scattering nature of this material. These blends can cause the transmitted light to scatter more; therefore the energy delivered to weld per unit area decreases for these materials.

The beam profile has been calculated at two locations: (i) 12.6 mm from the edge near the start of the scan where the plaque thickness is a minimum and (ii) 42 mm from the edge in the middle of the scan where the plaque thickness is a maximum. The values of the three model parameters  $\sigma$ ,  $\delta$  and  $\frac{1}{\Psi^*(0)}$  fitted to this data are found in Table 4-1.

There are several interesting conclusions that can be drawn from this table. For all materials and locations,  $\delta$  varies from 0.97 to 0.99 which is a very high value. For comparison, the scattering coefficient for a 3.2 mm plaque of PA6 0GF is equal to 0.64. On the other hand, the same parameter for PA6 30GF (another highly scattering material) with the same thickness is reported to be 0.99 [1]. This shows that the fraction of scattered light in case of PBT/PET blends is comparable to other glass filled materials. The value of  $\sigma$ , which describes the distribution of the scattered energy, does not appear to follow any significant trend. However, a slight increase of this parameter can be seen when moving to the centre of the plaque, where the maximum thickness is observed. The scattering standard deviation for PA6 is equal to 0.9 mm and for PA6 30GF is equal to 1.13 mm as reported in previous studies [1]. Based on these results, it can be said that the area over which the light is scattered, is significantly higher than other semi crystalline materials even those containing glass fibres.

**Table 4-1 The beam profile distribution at 12 mm and 42 mm distance from the edge of the plate**

<i>Material</i>	$\sigma$	$\delta$	$1/\Psi^*(0)$	$R^2$	<i>Distance (mm)</i>
<b>PBT/PET 100/0</b>	1.41	0.98	2.6313	0.9963	12
<b>PBT/PET 100/0</b>	1.43	0.98	2.6313	0.9938	42
<b>PBT/PET 90/10</b>	1.41	0.97	2.5641	0.9914	12
<b>PBT/PET 90/10</b>	1.47	0.98	2.7027	0.9948	42
<b>PBT/PET 75/25</b>	1.39	0.99	2.7027	0.998	12
<b>PBT/PET 75/25</b>	1.47	0.98	2.7027	0.9963	42

Based on the model parameters, the estimated power distribution of the scattered laser beam is shown in Figure 4-6, Figure 4-7 and Figure 4-8 for each blend. Each figure shows the power distribution of a blend at two different thicknesses. For reference, the unscattered power profile from the laser is also given in each figure.

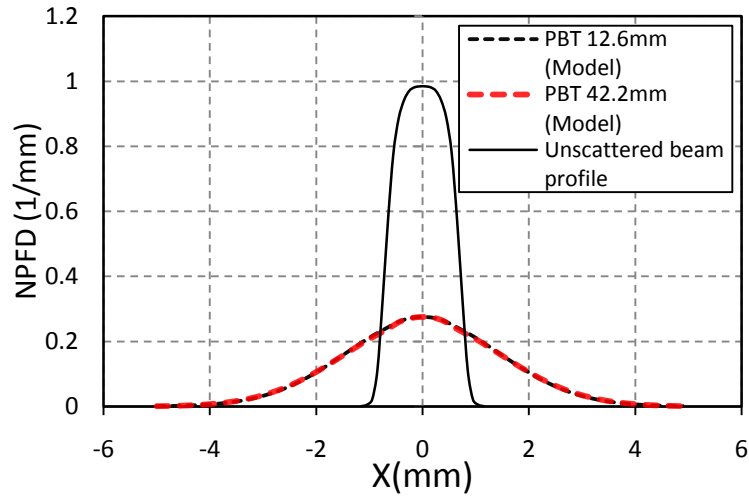


**Figure 4-6 Normalized power distribution after the scattered laser gets absorbed by the black part (PBT/PET 100/0) for 12.6mm and 42.2mm distance from the edge**

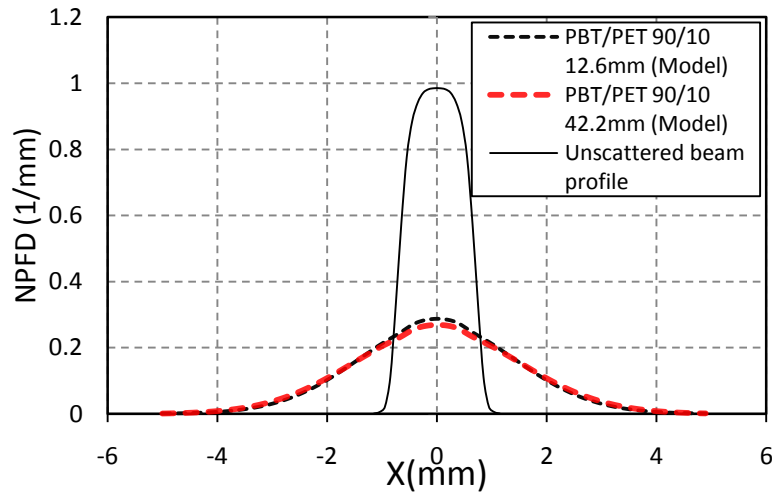


**Figure 4-7 Normalized power distribution after the scattered laser gets absorbed by the black part (PBT/PET 90/10) for 12.6mm and 42.2mm distance from the edge**

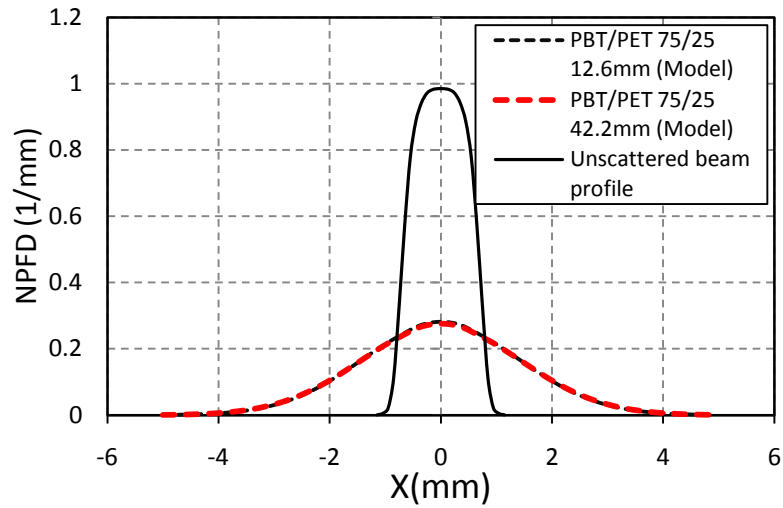


**Figure 4-8 Normalized power distribution after the scattered laser gets absorbed by the black part (PBT/PET 75/25) for 12.6mm and 42.2mm distance from the edge**

The relative energy distribution at the weld interface is obtained by multiplying the NPDF by the transmission presented in Figure 3-8 and Table 3-5. Figure 4-9 demonstrates the relative energy distribution of the transmitted laser light based on the scattering quality and transparency of the three materials. The energy distributions at the weld interface for all three materials are similar.

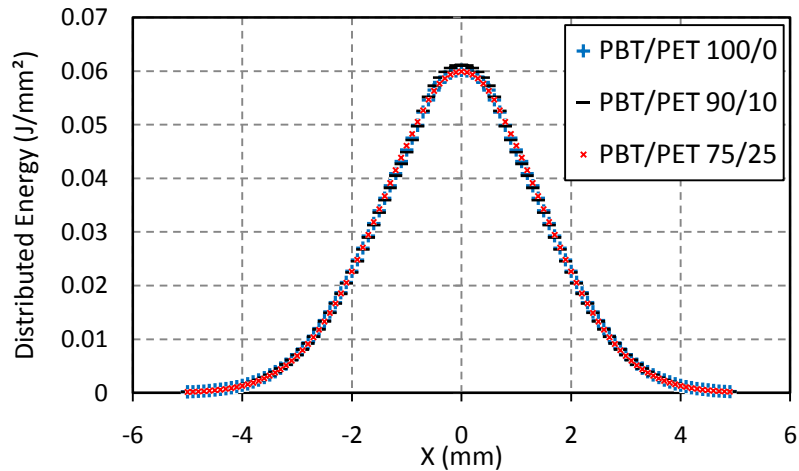


**Figure 4-9 Normalized power distribution of all three blends at 12.66 cm distance away from the edge of the part**

One of the issues with the analysis used to estimate the distribution of the scattered light is the lack of  $P_0/P_k$  vs.  $w_k/2$  data at large values of  $w_k/2$ . This required the use of a semi-empirical model involving scattered and direct light developed by Chen [1]. In the case of more transparent materials as in the work of Zak et al. [8], it is possible to estimate the scaling factor  $1/\Psi^*(0)$  more directly by calculating the total area underneath the  $P_0/P_k$  vs.  $w_k/2$  rather than estimating it numerically. More transparent materials require less input energy in order to melt or soften the interface. However, for materials with low transparencies like the PBT/PET blends, higher energies were required. At very high energies, burning and melting of the incident transparent surface was observed. This limited our ability to perform experiments at the highest powers and therefore made it impossible to estimate the scaling factor by calculating the total area underneath the  $P_0/P_k$  vs.  $w_k/2$  curve. By way of example, Figure 4-10 shows  $P_0/P_k$  vs.  $w_k/2$  data for PA6 containing 0%GF [1] and for PBT.

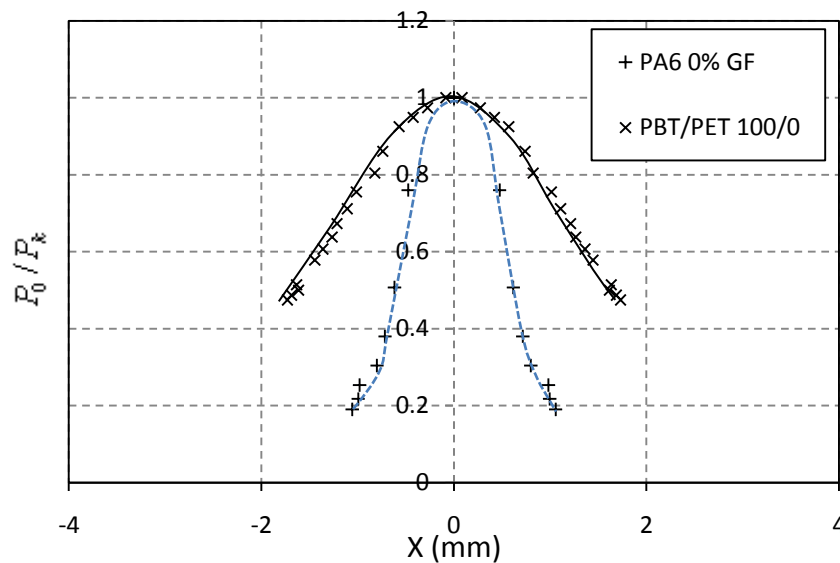


**Figure 4-10 Comparing the relative power ( $P_0/P_k$ ) vs. melt width for PBT/PET 100/0 and PA6-0GF**

It is clear that the PA6-0GF data covers a much larger fraction of the complete  $P_0/P_k$  range. In retrospect, it may have been possible to use a black part with lower melting temperature in order to lower the energy required for the onset of melting. This way, it would have been possible to obtain more  $P_0/P_k$  data at the edges of the NPDF profile. Since the estimation of  $1/\Psi^*(0)$  affects the estimations of  $\sigma$  and  $\delta$ , having a wider range of  $P_0/P_k$  vs.  $w_k/2$  data would improve the accuracy of this beam profile technique.

Additional information on scattering can be obtained by more closely examining some of the melt-width data obtained using this technique. Figure 4-11, Figure 4-12 and Figure 4-13 present the melt-width at the centre and the beginning of the laser scan for the three blends. The melt-width value starts to grow from zero at the threshold power for all the cases. At any given power, the melt-width is highest for the pure PBT material. As suggested earlier, this is partly due to the higher transmission of the PBT. However, due to difficulties in accurately assessing the normalized power flux distribution discussed above, the wider melt width may also be due to a less scattered beam in the PBT material since less scattering nature of PBT increases the energy distribution per unit area of the absorbing part.

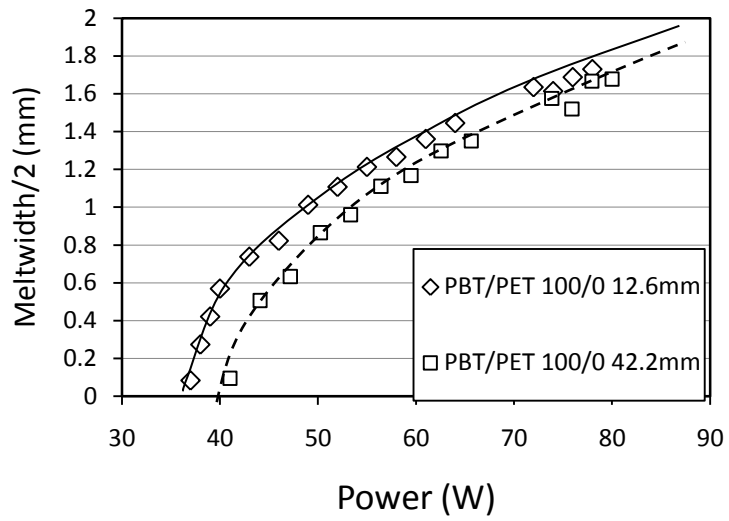


Figure 4-11 Half of melt-width variation at the edge and the middle of PBT/PET 100/0 part

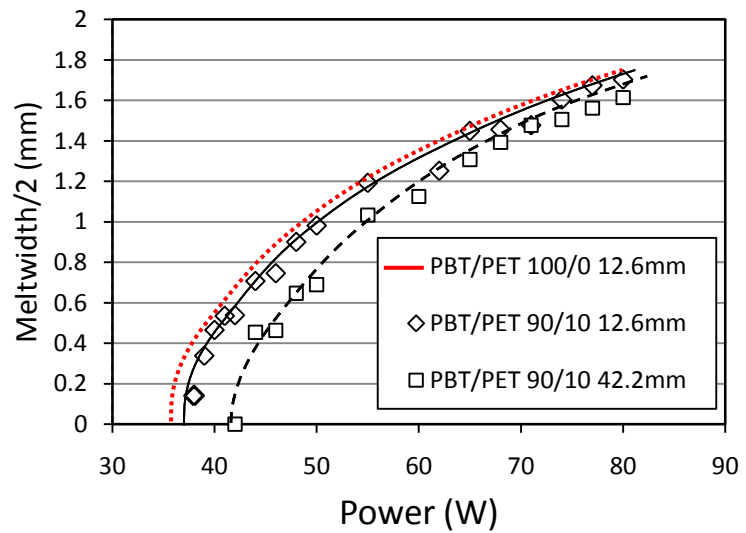
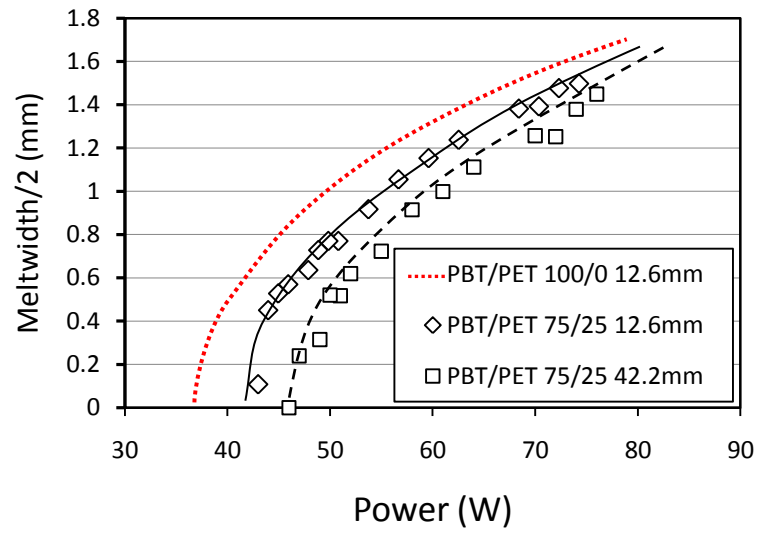


Figure 4-12 Half of melt-width variation at the edge and the middle of PBT/PET 90/10 part



**Figure 4-13 Half of melt-width variation at the edge and the middle of PBT/PET 75/25 part**

## Chapter 5

### **Weld Strength Study**

#### **5.1 Introduction**

For a given material, the weld quality depends on parameters such as laser power and laser scanning speed. Different values for these parameters will create different responses at the weld interface. Any of the following may take place. They may: not melt the interface, cause partial melting with bonding, create a weld, or, in the extreme case, cause polymer degradation. The combination of laser power and speed can also affect the transparent component. As described in 2.2.2, excessively high line energies have been observed to cause degradation on the surface of the transparent component. Therefore, in order to analyze the quality of the weld, it is essential to determine the region of line energy (ratio of power and scan speed) at which welding will occur.

This chapter describes different responses of the polymer at different line energies. Section 5.2.1 describes the method used to assess the material responses as a function of power and speed in order to determine the process window. Section 5.2 describes the technique used to assess the weld strength of lap joints. Finally, in Section 5.3, the results for both are presented and discussed.

## 5.2 Equipment/Method

### 5.2.1 Process Window Study

In order to determine the appropriate region for laser transmission welding, the process window was identified for three blends of PBT/PET. The parts were first cut into small plaques of dimensions of 25mm×80mm×2mm for the transparent part and 25mm×80mm×3mm for the corresponding black absorbing part. The transparent and absorbing parts were mated under pressure using the fixture shown schematically in Figure 5-2. Welding trials were conducted at 4 scanning speeds (500, 1000, 1250, and 1500 mm/min). At each scanning speed, the laser beam made a series of 15 mm long scans over the mated parts. Each scan was separated by a distance of 10 mm as shown in Figure 5-1. With each scan, the power was increased in increments of 5 watts.

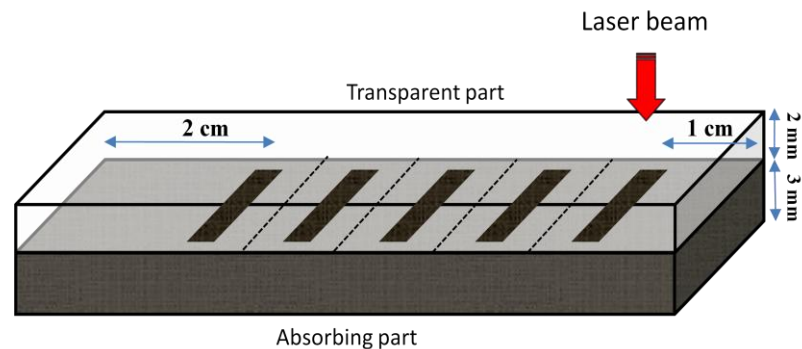


**Figure 5-1 Schematic view of the transparent and absorbing part used for operating window test**

The assembly was then cut with a lab-scale Jobmate© 6-in bandsaw between the welds in order to assess the quality of the joints. The melting region was identified by the first marks of melting at the weld interface. The upper boundary of melting region was very weak joints that

could be easily detached. The surface of the transparent part was also analyzed visually for any kind of marks created by the laser beam.

### 5.2.2 Weld Strength Study

Once the weld process window was determined, the strength of lap welds was measured. The fixture used to weld the assemblies is shown schematically in Figure 5-2. Each weld was 10 mm long and started/ended 5 mm away from the edges of both transparent and absorbing parts. The weld line was oriented parallel to the test pull direction. Orienting the weld line in this manner was recommended by Chen et al. [35].

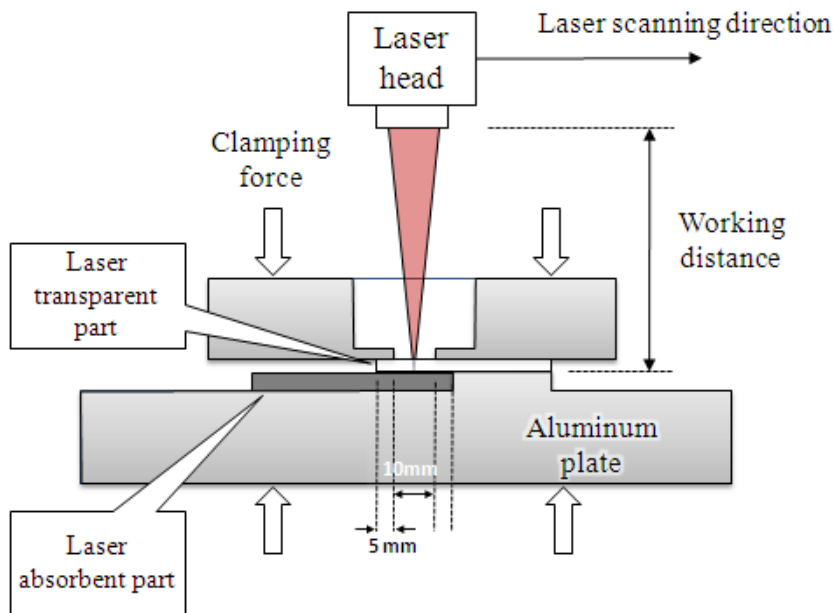


**Figure 5-2 Schematic view of the apparatus used for making the overlapped welds**

Welding was performed at a range of powers (35 to 100 W) and at constant speed of 1000 mm/min. These conditions were selected based on the results from the process window

study. The focal point of the laser was positioned at the top surface of the transparent part in order to bring the highest flux of energy inside the polymer bulk before getting scattered due to the scattering nature of the polymer. During the scanning trials, room temperature air was blown on the surface of the transparent part in order to cool it down. This was observed to minimize surface degradation on the transparent part.

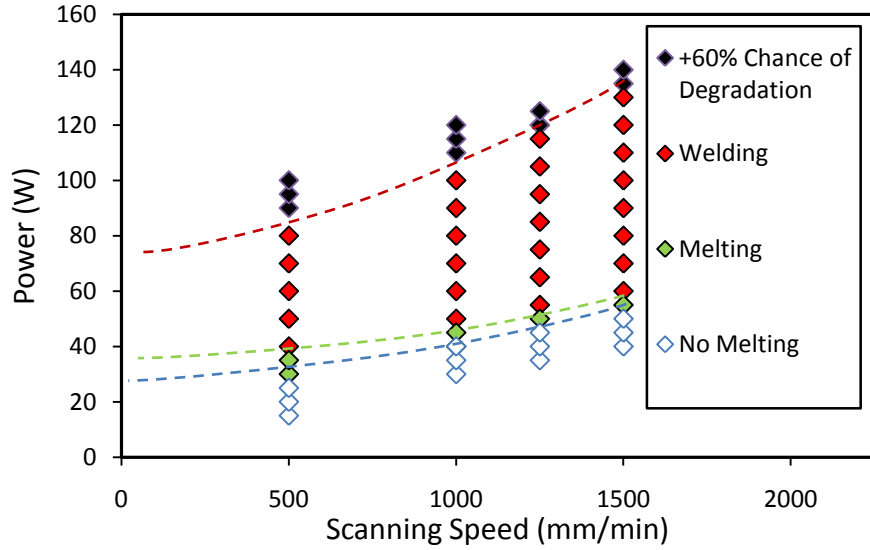
As suggested by Chen [1], the weld-line was oriented along the Z axis of the laser beam in order to create the widest weld seam possible (see section 4.1). Since the beam is wider along the X axis, this creates a wider weld line. The wider weld lines result in stronger joints.

Five replicate runs were made for each power level and material. The welded assemblies were tested on an INSTRON 4206 Universal testing machine located at RMC. All tests were performed at a cross-head speed of 5 mm/min.

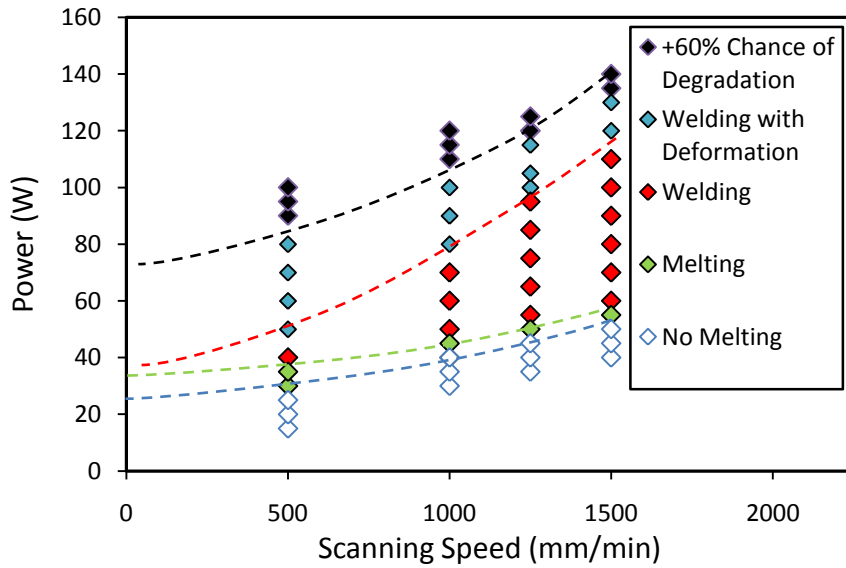
### **5.3 Results and Discussion**

Figure 5-3, Figure 5-4, and Figure 5-5 show the process window study for all three blends of PBT/PET 100/0, 90/10 and 75/25. The plots show the power-scan speed combination required for different phenomena including melting, welding, and surface deformation and degradation for the transparent part. At low line energies, the energy delivered to the absorbing part is not high enough to melt the weld interface. By increasing the line energy (whether by decreasing the scanning speed or increasing the power) the delivered energy starts to increase. Therefore, as it can be seen in Figure 5-3, the weld interface starts to melt. However, this energy is not high enough to cause melting on the transparent part due to conduction. Increasing the line energy provides additional energy and causes welding. Further increases can cause degradation of the incident surface of the transparent part. The degradation zone in Figure 5-3, Figure 5-4 and

Figure 5-5, denotes burn marks on more than 3 of the 5 specimens (60% chance of degradation). For those blends containing PET, the top surface of the transparent parts also started to deform locally above a critical line energy while the laser was scanning over it as shown in Figure 5-5.



**Figure 5-3 Operating window for PBT/PET 100/0**



**Figure 5-4 Operating window for PBT/PET 90/10**

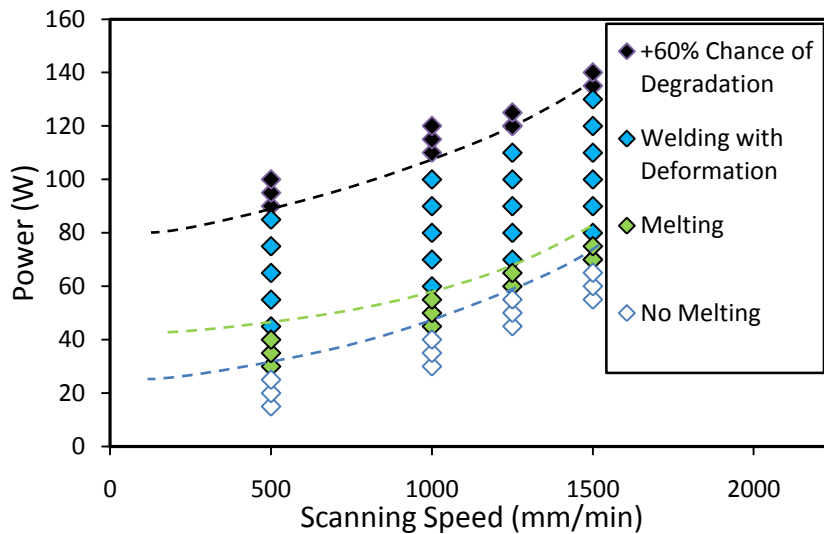


**Figure 5-5 Operating window for PBT/PET 75/25**

For all materials, the power required to induce any given phenomenon increases with scanning speed. At low scanning speeds, the total irradiation time is large and energy losses due to conduction may be a significant fraction of the delivered energy. As the speed is increased, any given phenomenon can be described by a line of constant slope having a zero intercept. This suggests that line energy can be used to describe these events at higher scan speeds.

By comparing the process windows of all three blends, it can be seen that increasing the PET-content in the blend, causes narrower process window. The onset of melting and welding in these blends are higher than that of the pure PBT. This is likely due to the higher melting point of crystalline PET versus PBT. Furthermore, at higher powers, PET-containing blends are subject to deformation of the transparent surface. Typical marks are shown in Figure 5-6 for the PBT/PET 75/25 material. These marks do not appear to be related to degradation that has been observed by others [1].

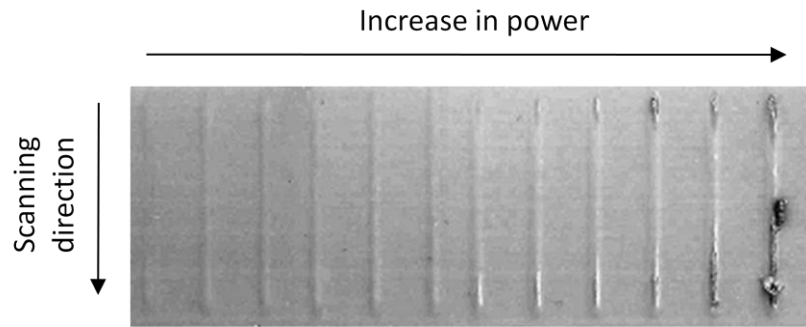


**Figure 5-6 Deformation on the transparent part for PBT/PET 75/25 by increasing the power**

As it can be seen in Figure 5-6, these ribs become more and more visible at higher powers. They also appear to intensify as the ratio of PET in the blend is increased. On the other hand, no significant marks were observed on the transparent PBT plaques until reaching the surface degradation zone. Grewell et al. [37] observed similar effects during welding trials for PC and PS polymers described in section 2.2.2. According to their study, the surface deformation started to recover by the time the laser was turned off. The laser position and recovered marks are shown in Figure 5-7. The laser arrow in this figure shows the position of the laser beam while scanning across the transparent part, and the recovered arrow shows the region that has been scanned earlier. It can be seen that the marks at the recovered region are attenuated. This phenomenon as described in 2.2.2 is believed to be due to thermal expansion from heating by the laser followed by cooling.

Figure 5-8 shows the maximum load at break as a function of power for each of the three materials. For all materials, the strength is observed to increase at low powers. As discussed previously, the power required to achieve a weld goes up with increasing levels of PET in the blend. Based on Figure 5-9, the blend containing the most PET (PBT/PET 75/25) could support the lowest maximum load of approximately 1000N. Conversely, pure PBT and the 10% PET

reached over 1100N. As shown in Figure 5-8 for all three blends, the maximum load starts to decline after reaching the peak value. Previous studies have shown that this may be the onset of degradation at the weld interface [1] [22].

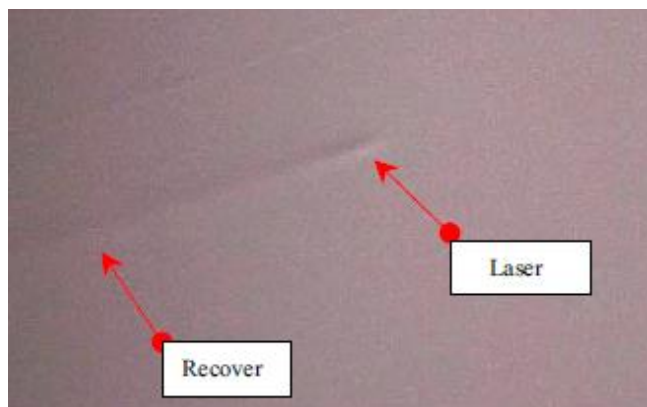


**Figure 5-7 Photograph showing "recovery" after heating for PS [37]**

In order to further analyze the drop off in strength at high powers, the fracture surfaces were examined using ImageJ 1.42q image processing software after scanning the fracture surfaces at a resolution of 1200 dpi. Figure 5-9 shows the fracture surface of the weld for PBT/PET 100/0 at  $P=80W$  and at  $P=90W$ . The weld made at 80W is relatively homogenous.. However at 90W, the aspect at the centre of the weld is significantly different than the sides. It is believed that material at the centre underwent thermal degradation. As discussed in 4.3, once the laser beam passes the semi-crystalline medium and is scattered, the NPDF of the transmitted beam shows a maximum at the center of the distribution. Therefore, the center of the weld experiences higher transmitted energies and consequently higher temperatures which are believed to cause thermal degradation of the polymer.

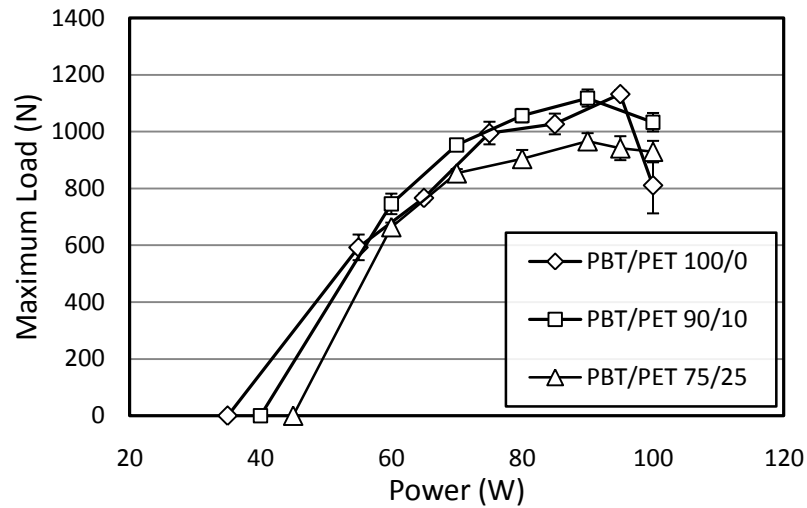


**Figure 5-8 Maximum load at different laser powers, with scanning speed of 1000 mm/min for three blends of PBT/PET 100/0, 90/10, 75/25**

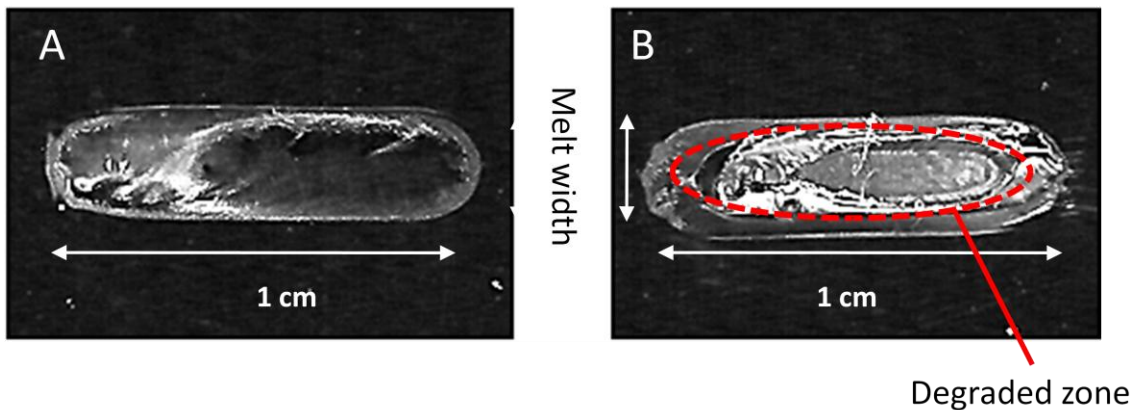


**Figure 5-9 Weld interface for PBT/PET 100/0 with A) Scanning power of 80W and B) Scanning power of 90W**

Although the force at break for a weld provides useful information on the load carrying capability of the joint, it does not always provide an accurate picture of weld quality. Low weld strengths can be compensated for by wide weld widths. It is therefore insightful to calculate the

apparent shear strength of the assembly. This requires knowledge of the weld area. Figure 5-10 shows the weld width as a function of laser power. It was measured after scanning the fractured surfaces at 1200 dpi and using ImageJ 1.42q software for image analysis. The data shows that, for all materials, the weld width increases with increasing power. The reason for this is that by increasing the power, a greater fraction of the transmitted beam has sufficient energy flux to cause melting of the absorbing part. It is observed that, for the same power, the weld width is almost 0.5 mm bigger for PBT than the other two blends. For the other two blends the one with 10% PET has slightly larger weld-width than the one with 25% PET. This can be due to two possible reasons. First, according to the transmission data presented in 3.4.3, the transmission ratio for pure PBT is slightly higher than the blends containing PET and consequently more energy is received by the absorbing part. The second reason is due to lower overall melting temperature for pure PBT. By adding more PET to the blend, more energy is required to melt the PET crystalline fraction that has a higher melting temperature than PBT.

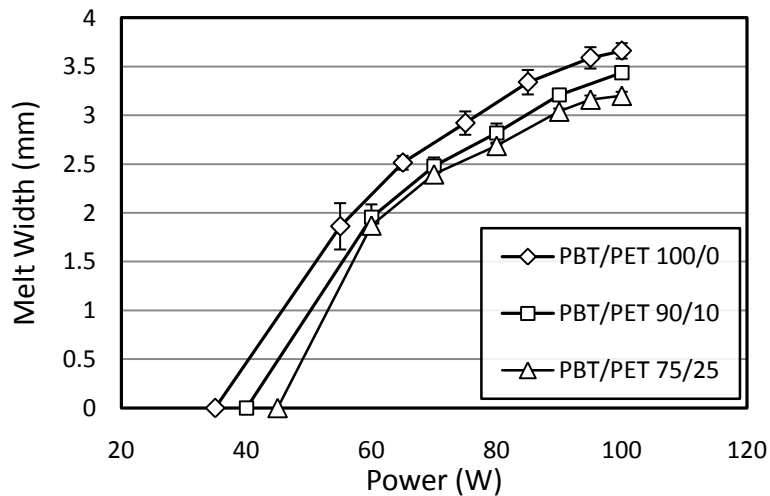


**Figure 5-10 Melt width at different laser powers, with scanning speed of 1000 mm/min for three blends of PBT/PET 100/0, 90/10 75/25**

The apparent weld shear strength ( $\tau$ ) is defined as [16]:

$$\tau = \frac{F}{a} \quad \text{Equation 5-1}$$

where  $F$  is the force applied to the overlap joint causing failure and  $a$  is the weld area. Figure 5-11 presents the maximum shear strength for three blends. The results show that the blend with 10% PET has the highest apparent shear strengths relative to the other two.

In order to determine their bulk tensile strength, tensile tests were carried out for all three blends using the INSTRON 4206 Universal testing machine located at RMC. Details for these tests can be found in Appendix C. Table 5-1 shows the summary of the tensile strength results. It can be seen that the measured tensile strength values for all three blends, fall within the range of 55-80 MPa strength values for pure PBT reported in other references [48]. By comparing these results with the shear strength of the welded specimens, it can be seen that the weld strength is 51% of the bulk strength for PBT/PET 100/0, 59% for PBT/PET 90/10, and 53% for PBT/PET 75/25.

**Table 5-1 Average load at break and tensile test for three blends**

<b>Material</b>	<b>Average load at yield (N)</b>	<b>Average tensile strength (MPa)</b>
PBT/PET 100/0	1004	66.4
PBT/PET 90/10	1003	66.3
PBT/PET 75/25	1008	66.6

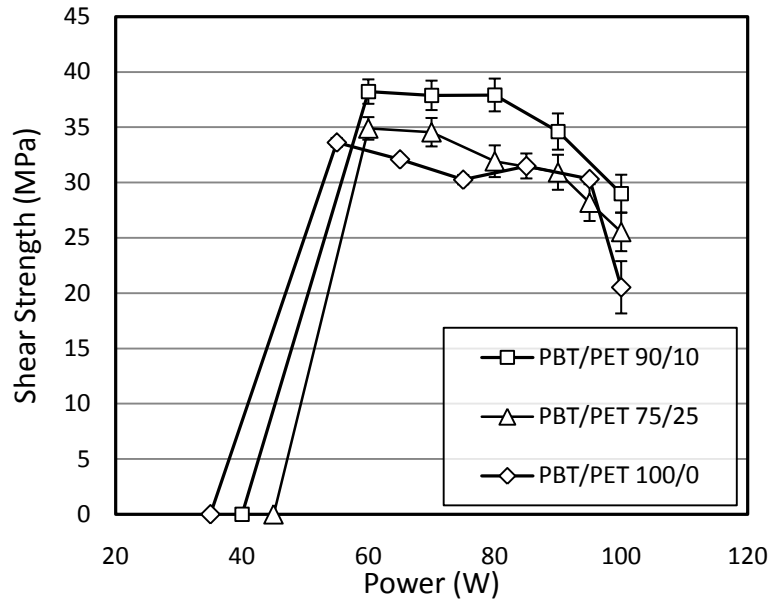


**Figure 5-11 Shear strength at different laser powers, with scanning speed of 1000 mm/min for three blends of PBT/PET 100/0, 90/10, 75/25**

The weld shear strength for PBT material, increases to a maximum of  $P=60W$  and then decreases at higher powers. This might be due to degradation occurring at the weld interface. As shown in the TGA analysis (section 7.3), PBT was observed to be less thermally stable compared to PET. Shear strength for materials containing PET is relatively higher and starts to drop at higher powers that can be addressed to higher thermal stability of these materials.

## Chapter 6

### **Thermal Modeling**

This section provides an introduction to the finite element simulation (Section 6.1), presents the assumptions applied to the model used in this research (Section 6.2), and finally presents and discusses the results for the PBT/PET blends (Section 6.3).

#### **6.1 Introduction**

Thermal modeling of the LTW process predicts the temperature in the assembly as a function of time and location. The purpose of this thermal simulation is to estimate the maximum temperature as a function of time in the assembly during welding. This information will be used as an input to a model of thermal degradation developed in the next chapter.

In this work, a 2-D transient thermal model examines the effects of optical properties of both transparent (transmission) and the absorbent (absorption due to the CB level) parts on the temperature distribution in the heat affected zone during the LTW. Given the difficulties in estimating the heat generation (due to laser light absorption) in the transparent part (see section 2.2.2), no light is assumed to be absorbed in the transparent part. The measured total transmission through the transparent part is used to calculate the laser energy arriving at the weld interface. The Beer-Bouguer-Lambert equation is then used in the absorbent part to calculate energy absorption as a function of depth and absorption coefficient. Heat is lost from this absorption zone by conduction into the both transparent and absorbent parts.

The general heat transfer equation is:

$$c\rho \frac{\partial T}{\partial t} = k\nabla^2 T + Q \quad \text{Equation 6-1}$$

where  $k$  is the thermal conductivity of the sample;  $c$  is the specific heat capacity;  $\rho$  is the density of the sample and  $Q$  is the generated heat due to the laser light absorption by the black part. The total laser power loss per unit depth  $y$  in a polymer can be calculated from equation 6-2 as described in section 2.2.2:

$$Q = \left| \frac{dP''(y)}{dy} \right| = (1-\eta)P_L'' K_E e^{-K_E y} \quad 0 < y < D_a \quad \text{Equation 6-2}$$

This lost electromagnetic energy is all converted into heat at a given depth and causes the temperature rise at depth  $y$  of the polymer. Equation 6-2 is the equation used in order to calculate the laser-generated heat in the absorbing part.

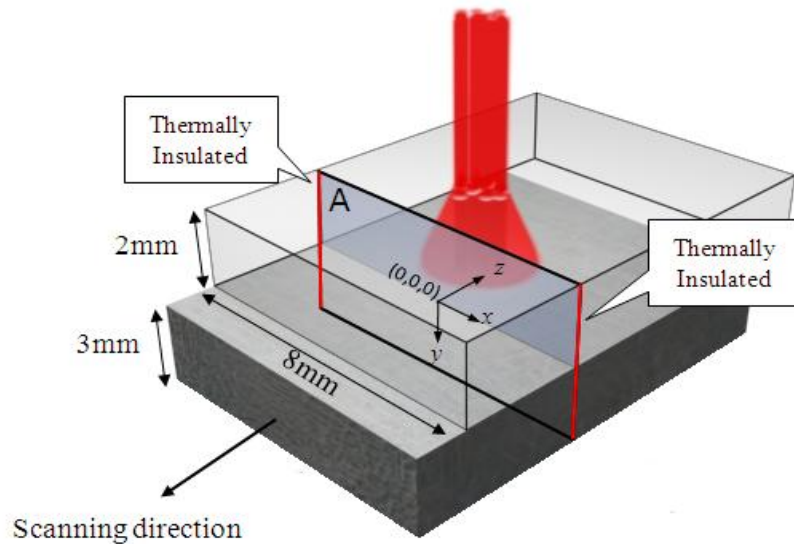


**Figure 6-1 Schematic view of the scattered laser beam passing plane A in a 2-D case of laser transmission welding**

As shown in Figure 6-1, the 2-D transient thermal model calculates the temperature distribution on the plane A which is parallel to  $xy$  plane and perpendicular to the scanning direction of the laser beam. The simulation starts with the beam located behind the plane and ends several seconds after it completely passes through the plane.

## 6.2 Method

### 6.2.1 Material Properties

The material properties used in the model can be divided into optical properties and thermal properties. The optical properties such as the scattering coefficient ( $\delta$ ) and scattering standard deviation ( $\sigma$ ) were measured in Chapter 4. Other optical properties such as transmission and reflection of the blends were presented in Chapter 3. These parameters are summarized in Table 6-1. Those properties varying with temperature, such as heat capacity ( $c$ ), density ( $\rho$ ) and thermal conductivity ( $k$ ) were measured and presented in Appendix A.

**Table 6-1 Summary of optical properties for three blends of PBT/PET 100/0, 90/10 and 75/25**

	<b>PBT/PET 100/0</b>	<b>PBT/PET 90/10</b>	<b>PBT/PET 75/25</b>	<b>Method</b>
<b>Scattering Standard Deviation(<math>\sigma</math>) [mm]</b>	1.37	1.32	1.39	Beam profile model
<b>Scattering Coefficient (<math>\delta</math>) [1]</b>	0.99	0.97	0.99	Beam profile model
<b>Transmission (<math>K_T</math>) [1]</b>	0.165	0.140	0.138	NIR Spectrophotometer
<b>Extinction coefficient (<math>K_E</math>) for absorbing part [1/mm]</b>	9.0-19.0	19.0	19.0	Fitted to the experimental data

The extinction coefficient for the absorbing part ( $K_E$ ) was used as a fitting parameter. A series of sensitivity studies were conducted in order to find the value of  $K_E$  that, when used with PBT, predicted temperature profiles that were consistent with the experimental weld width data. This will be discussed in more detail in section 6.3.

### 6.2.2 Input Laser Beam Energy Distribution

The laser beam modeled here scans over the top surface of the transparent part at a scanning speed of 1000 mm/min – the same speed as that used for mechanical testing. Different computational simulation runs were performed at laser powers ranging from 50W to 100W. In the model, the focal point was set to contact the assembly at the top surface of the transparent part. This is consistent with the experimental work described in Chapter 5. Figure 6-2 shows the 2-D normalized power distribution of the unscattered beam on the top surface of the transparent part. This distribution was obtained by using the pinhole technique as explained in Chapter 2.

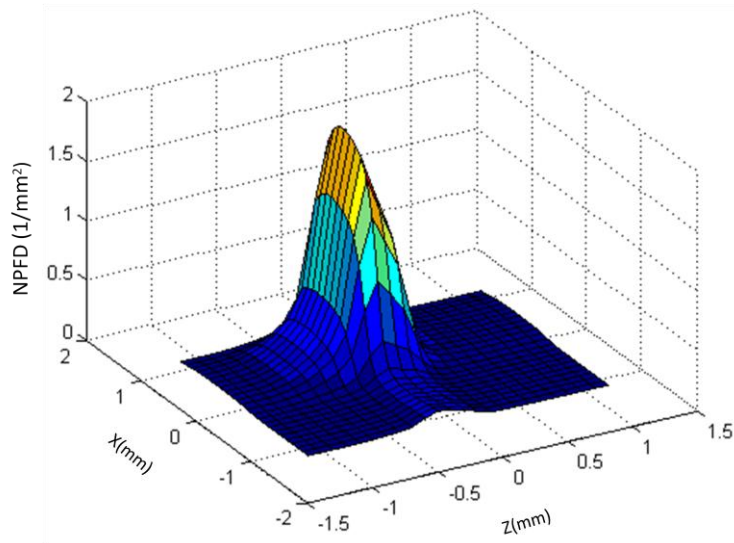


**Figure 6-2 2-D NPDF of unscattered laser beam at 82.5mm distance from laser head [14]**

The temperature on plane A was simulated for 15 seconds. This is the time it takes the laser beam to travel 250 mm along the z axis. The beam starts 16.5 mm behind the plane to avoid any energy reaching this plane at time zero.

### 6.2.3 Software and Mesh optimization

In order to simulate the heat transfer problem, COMSOL Multiphysics 3.5 software was used. A Lenovo laptop SL510 Personal Computer with 2.0 GHz Core 2 Duo CPU and a 4 GB of RAM was used to run this commercial code.

A free mesh with triangular element geometry was used for this model. The red spot shown in Figure 6-3 is where the centre of the mesh is located. The growth rate coefficient was set to be 1.03. In order to make sure the temperature distribution was not going to be affected by the mesh size in the FE method, the model was run with different minimum mesh sizes at the centre of the weld interface and the maximum temperature at that position was calculated for PBT at a constant power of 100W and an extinction coefficient value of 19.

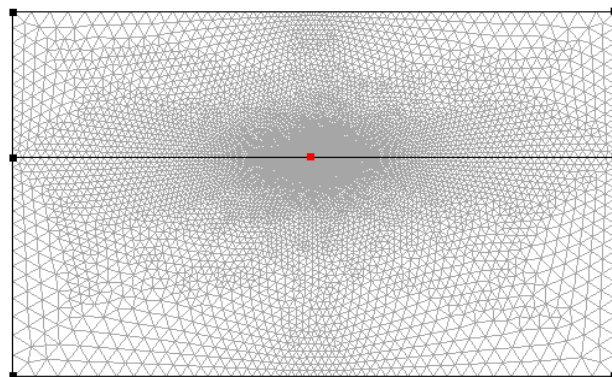


**Figure 6-3 Mesh grid on plane A**

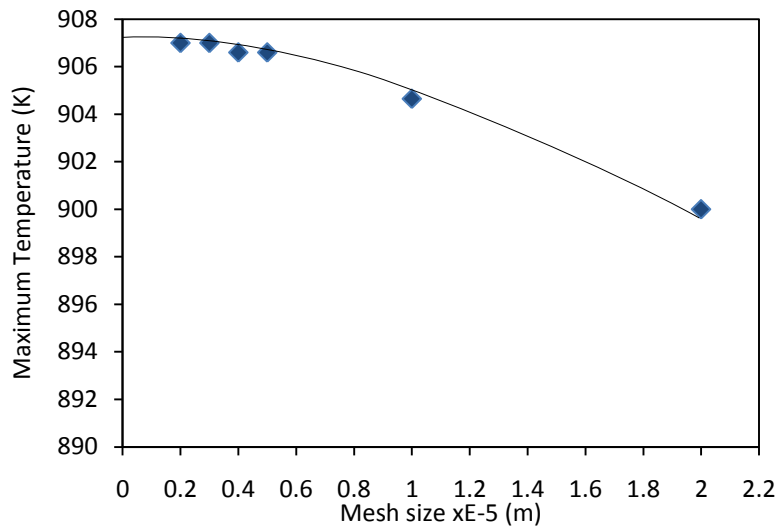


**Figure 6-4 Maximum temperature at the centre of the weld as a function of mesh size**

The results of this grid size sensitivity study are shown in Figure 6-4. The results show that the maximum temperature at the center of the weld varied by less than 1 K at mesh sizes below 0.005mm. Therefore, a minimum size of 0.003 mm was selected for this study. There were 15665 elements with 31486 degrees of freedom in this 2-D coupled model with a maximum mesh size of 0.01 mm in the controlled meshing area as well as a default mesh growth rate of 1.03. For these conditions, the solution convergence time was approximately 4 minutes.

### 6.3 Results and Discussion

The extinction coefficient of the absorbent part was not known with any precision. It was estimated using a sensitivity study. The width of the PBT weld was simulated by calculating the maximum distance between points along the x-axis at  $y=0$  that had reached the temperature of 225°C or higher. This corresponds to the melting temperature of PBT. In other words, it is assumed that a weld will only form when the temperature has reached this nominal value. These

estimated weld widths were then compared with experimental values (as reported section 5.3). This is consistent with the approach of Chen [1]. Figure 6-5 shows a comparison of simulated widths as a function of power for a range of extinction coefficient values as well as experimental data.

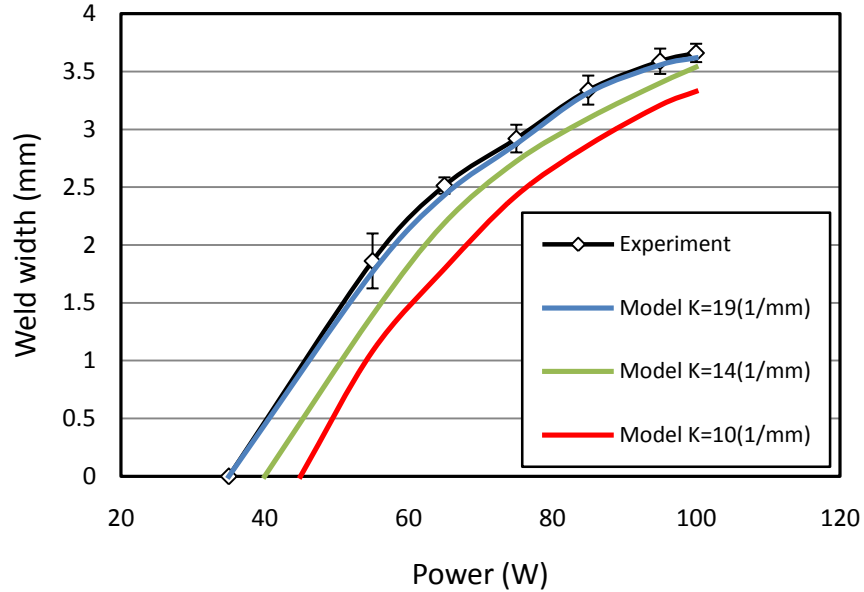


**Figure 6-5 Sensitivity study to estimate extinction coefficient for the black part for PBT/PET 100/0**

As shown in Figure 6-5, comparison between the experimental values of the weld widths and the results from the model suggests that a value of  $K_E=19.0$  (1/mm) can be used to accurately model experimental data. For the purposes of this exploratory study, this value was then used for all three blends.

Using a  $K_E$  value of 19.0 (1/mm), Figure 6-6 shows the predicted simulated temperature field of PBT at a power of 100W after an exposure time of 1 sec. This time corresponds to the time at which the laser beam just passed the plane (given the scanning speed of 1000 mm/min).

The wide temperature distribution across the beam scanning direction corresponds to highly scattering quality of the transparent part. Using this data and similar data for the other materials, it is possible to obtain a plot of temperature versus time at the weld interface.

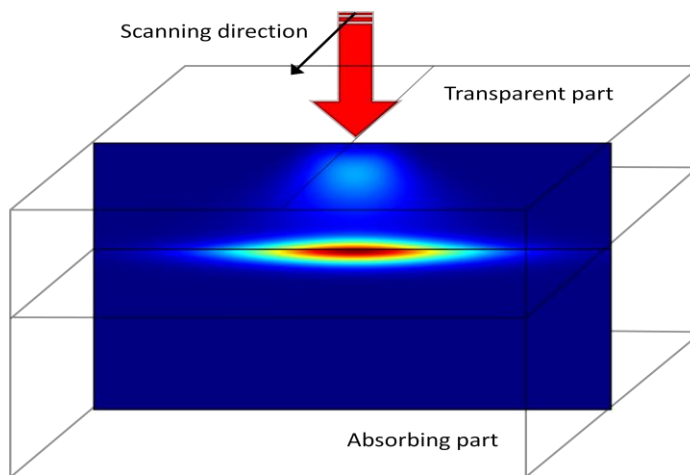


**Figure 6-6 Temperature distribution at the weld interface from the FE model for PBT at  $t=1\text{sec}$**

The temperature as a function of time at a point 0.035 mm below the weld interface (where the maximum temperature is reached) is shown in Figure 6-7, Figure 6-8, and Figure 6-9 for the three materials. For any given power, the temperature rises from the initial temperature of 23°C, to a maximum at  $t=1\text{sec}$ , which is the time at which the laser beam just passed through plane A. These maximum temperatures for three powers of 55, 70 and 100 watts are presented in Table 6-2. At high powers, very high temperatures are quickly reached but only for a very short period. Under the highest power conditions this has been observed to cause visible material degradation. However, it is not clear how much degradation would occur theoretically at lower temperatures given the short exposure times. These temperature-time profiles will be used to estimate degradation using a kinetic degradation model presented in the next chapter.

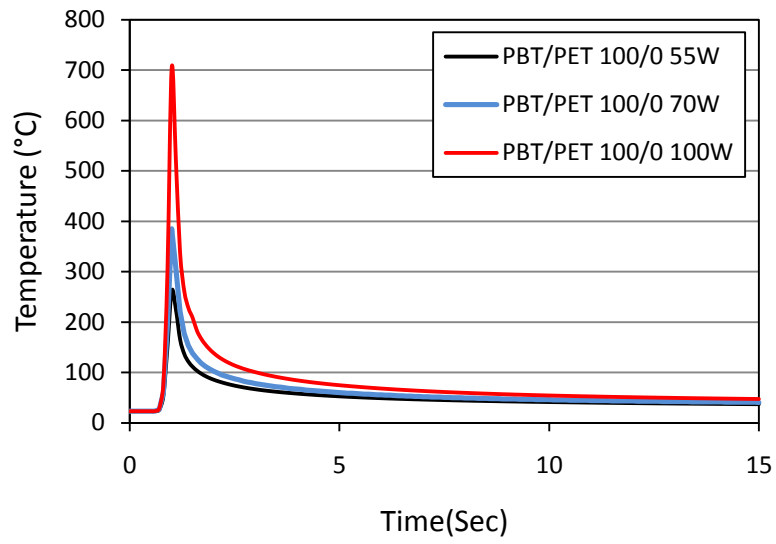


**Figure 6-7 Temperature predicted by the FE model at the centre of the weld 0.035mm below the interface for PBT/PET 100/0**

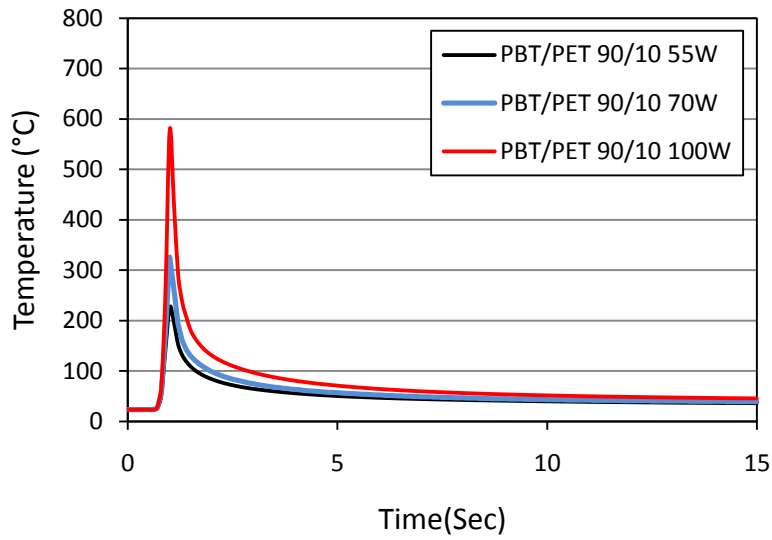


**Figure 6-8 Temperature predicted by the FE model at the centre of the weld 0.035mm below the interface for PBT/PET 90/10**

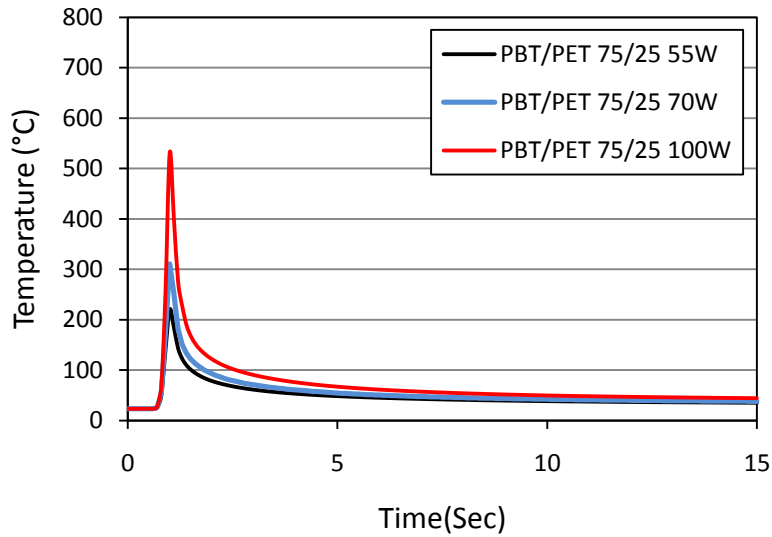


**Figure 6-9 Temperature predicted by the FE model at the centre of the weld 0.035mm below the interface for PBT/PET 75/25**

**Table 6-2 Maximum temperature predicted by the model for three blends using 55, 70, and 100W laser power settings**

<b>Power:</b>	<b>55W</b>	<b>70W</b>	<b>100W</b>
<b>PBT/PET 100/0</b>	262 °C	385 °C	704 °C
<b>PBT/PET 90/10</b>	226 °C	326 °C	578 °C
<b>PBT/PET 75/25</b>	220 °C	311 °C	531 °C

## Chapter 7

### Degradation Analysis

#### 7.1 Introduction

As discussed in Chapter 2, several events take place during the laser welding once the laser hits the very top surface of the transparent part. Part of the laser power gets reflected and the remainder passes the polymer or is absorbed inside the transparent part. The transmitted laser power is transformed into heat once it is absorbed by the black part. However, excessive heat generation may cause a large increase in temperature and may lead to polymer degradation in either absorbent or transparent side.

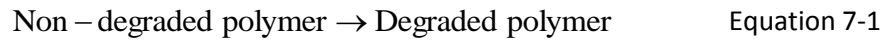
It is therefore important to investigate the degradation of polymer at the weld interface, depending upon: (a) the polymer (as different polymers will have different thermal stability depending on their composition and additives) and (b) the temperature-time profile (thermal history) experienced by the material during welding.

The kinetics of polymer degradation, unlike polymerization kinetics, is complicated by the occurrence of competitive, rather than consecutive reactions [43]. It is often studied using Thermo-Gravimetric Analysis (TGA). The evaluation of kinetic parameters from a TGA plot is difficult because the temperature as well as the composition of the system is changing. TGA either alone or in combination with Differential Thermal Analysis (DTA such as DSC) has been the chief diagnostic tool used to study the thermal decomposition of polymers. Because TGA consists of a reaction rate study at a succession of temperatures, the technique should be capable of providing information on reaction rates, reaction orders ( $n$ ), energies of activation ( $E$ ), and pre-

exponential factors ( $F$ ) for the degradation of polymeric materials [50]. It is acknowledged that degradation such as a decrease in molecular weight can occur without any weight loss as measured by TGA. This degradation analysis only considers molecular degradation in which volatile components are released. This would lead potentially to voids in at the weld interface after LTW.

In order to determine the performance of the polymer at high temperatures, the Freeman-Carroll method is proposed to analyze the data from TGA. The activation energy,  $E$ , and reaction order,  $n$ , of the investigated polymer degradation can be obtained by using this method [51].

If the decomposition of polymer A can be modeled by an  $n^{\text{th}}$  order irreversible reaction:



The kinetic rate equation for this reaction is assumed to follow:

$$-\frac{dC_A}{dt} = K_R C_A^n \quad \text{Equation 7-2}$$

where  $C_A$  is the concentration of non-decomposed polymer; and  $K_R$  is the temperature dependent rate constant given by the Arrhenius equation:

$$K_R = F e^{-\frac{E}{RT}} \quad \text{Equation 7-3}$$

where  $F$  is the frequency factor;  $E$  the activation energy;  $R$  the gas constant and  $T$  the absolute temperature.

For a reaction at a constant volume:

$$C_A = \left(\frac{m}{m_0}\right) \left(\frac{\rho}{Mw}\right) \quad \text{Equation 7-4}$$

where  $\frac{m}{m_0}$  is the ratio of non-decomposed material at time  $t$  ( $m$ ) to that initially present in the sample ( $m_0$ ),  $\rho$  the sample density and  $Mw$  the molecular weight. The non-decomposed fraction is redefined using:

$$\gamma = \frac{m - m_f}{m_0 - m_f} \quad \text{Equation 7-5}$$

where  $\gamma$  is the non-decomposed fraction of the sample; and  $m_f$  is the final mass after complete polymer degradation. This latter quantity accounts for material that does not degrade and does not lead to a weight change after degradation. It can be easily seen from Equation 7-5 that, in case of full degradation of the material when  $m_f = 0$ , the non-decomposed fraction is similar to ratio of the mass at time  $t$  and the initial mass.

These equations can be combined to yield:

$$-\frac{d(\gamma)}{dt} = A' e^{-\frac{E}{RT}} (\gamma)^n \quad \text{Equation 7-6}$$

where  $A'$  combines constant parameters such as  $F$ ,  $Mw$ ,  $\rho$  and  $n$ . Taking the natural logarithm of both sides yields:

$$\ln\left(-\frac{d\gamma}{dt}\right) = \ln A' - \left(\frac{E}{R}\right)\left(\frac{1}{T}\right) + n(\ln \gamma) \quad \text{Equation 7-7}$$

The term  $\ln A'$  can be eliminated from this equation by subtracting off values obtained at a reference time ( $t_r$ ) to obtain:

$$\frac{\Delta\left(\ln\left(-\frac{d\gamma}{dt}\right)\right)}{\Delta(\ln \gamma)} = n - \frac{E}{R} \frac{\Delta\left(\frac{1}{T}\right)}{\Delta(\ln \gamma)} \quad \text{Equation 7-8}$$

where

$$\Delta(\ln(-\frac{d\gamma}{dt})) = \ln(-\frac{d\gamma}{dt}) \Big|_t - \ln(-\frac{d\gamma}{dt}) \Big|_{t_r} \quad \text{Equation 7-9}$$

$$\Delta(\frac{1}{T}) = \frac{1}{T} \Big|_t - \frac{1}{T} \Big|_{t_r} \quad \text{Equation 7-10}$$

$$\Delta(\ln \gamma) = \ln \gamma \Big|_t - \ln \gamma \Big|_{t_r} \quad \text{Equation 7-11}$$

The differential terms are achieved by subtracting Equation 7-7 from a reference condition where  $T=T_r$  and  $t=t_r$ .

The order of the reaction and the activation energy of the reaction are determined according to Equation 7-8 by plotting the experimental data of  $\Delta(\ln(-\frac{d\gamma}{dt}) / \Delta(\ln \gamma))$  vs.

$\Delta(\frac{1}{T}) / \Delta(\ln \gamma)$ . The frequency factor can then be obtained using Equation 7-7. According to this

equation, the frequency factor would be the intercept of a plot of  $\ln(-\frac{d\gamma}{dt}) - n(\ln \gamma)$  against  $1/T$ .

These calculations were performed using the TGA data for each material presented in section 3.4.3 and a MATLAB code found in Appendix D.

During LTW, the temperature at the interface varies as a function of time. In order to determine  $T = T(t)$ , a two-dimensional (2D) finite element (FEM) thermal model of the process was developed. This 2D FEM model was described in Chapter 6.  $T = T(t)$  will depend on the location in the weld as all points have different thermal histories. For the purpose of this exploratory work, this position was assumed to be along the centre of the beam at the weld interface and 0.035 mm under the weld interface. According to the thermal model, this location has the maximum temperature in the absorbing part during the laser transmission welding at any given time and is therefore the most likely to undergo thermal degradation.

Once  $T = T(t)$  is known, Equation 7-6 can be rewritten as:

$$-\frac{d\gamma}{dt} = A'e^{-\frac{E}{RT(t)}}\gamma^n \quad \text{Equation 7-12}$$

Solving equation 7-12, results in:

$$\frac{1}{1-n}\gamma^{1-n} = -A' \int_0^{t_{\max}} e^{-E/RT(t)} dt + C \quad \text{Equation 7-13}$$

At  $t=0$ , the value for the integral becomes zero and  $\gamma = 1$ . Therefore, by replacing the constant value  $C$ , the final equation is:

$$\gamma^{1-n} = (n-1)A' \int_0^t e^{-E/RT(t)} dt + 1 \quad \text{Equation 7-14}$$

Equation 7-14, is the equation that is used in order to model the degradation during welding.

## 7.2 Equipment/Method

The TGA method and data were presented in Appendix E.

## 7.3 Results/Discussion

The TGA results from Chapter 3 are reproduced in Figure 7-1.

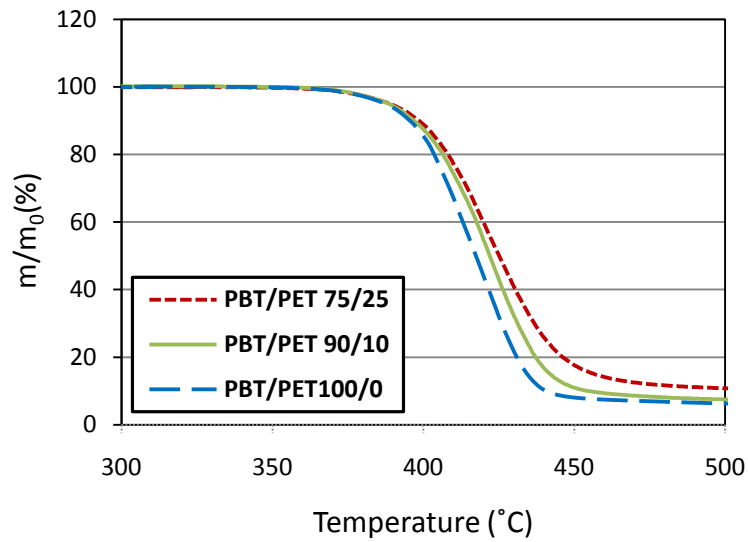


**Figure 7-1 TGA results for the three blends of PBT/PET**

Differential Thermal Analysis (DTA) in other studies has also shown higher material weight loss at a lower temperature for PBT compared to PET [52]. During the degradation process, cyclic oligomers of PBT start to form at temperatures below 290°C due to the presence of butylene unit. In contrast, in the case of thermally degraded PET samples, these oligomers were not observed [53].

The mass-temperature-time data are used to calculate the order of the reaction ( $n$ ), activation energy ( $E$ ), and the frequency factor ( $A'$ ) as discussed in Section 7.1. The results are shown in Figure 7-2, Figure 7-3, and Figure 7-4.

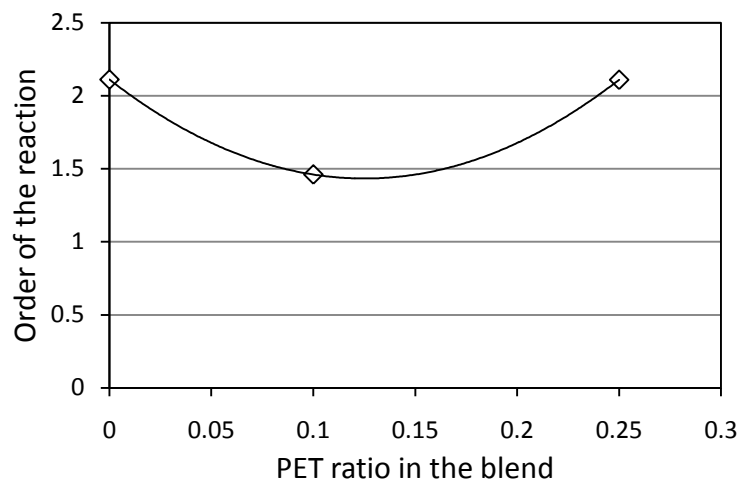


**Figure 7-2 Order of the reaction for blends of PBT/PET 100/0, 90/10, 75/25**

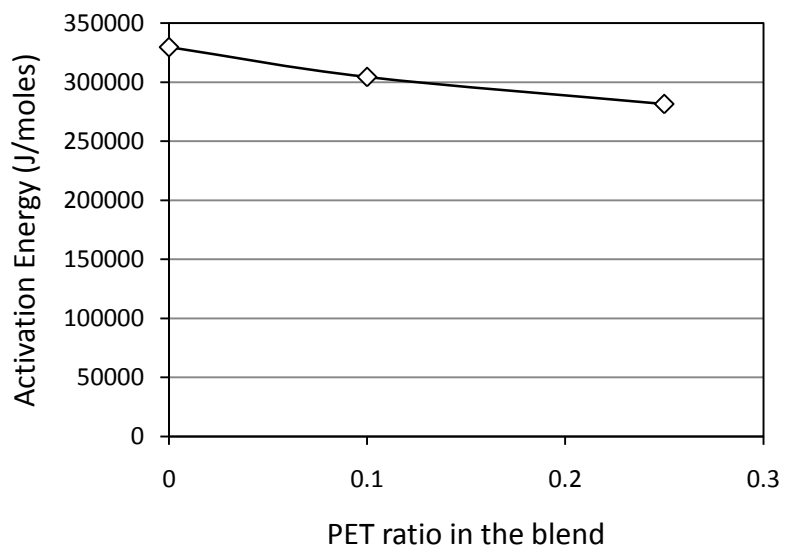


**Figure 7-3 Activation energy for blends of PBT/PET 100/0, 90/10, 75/25**

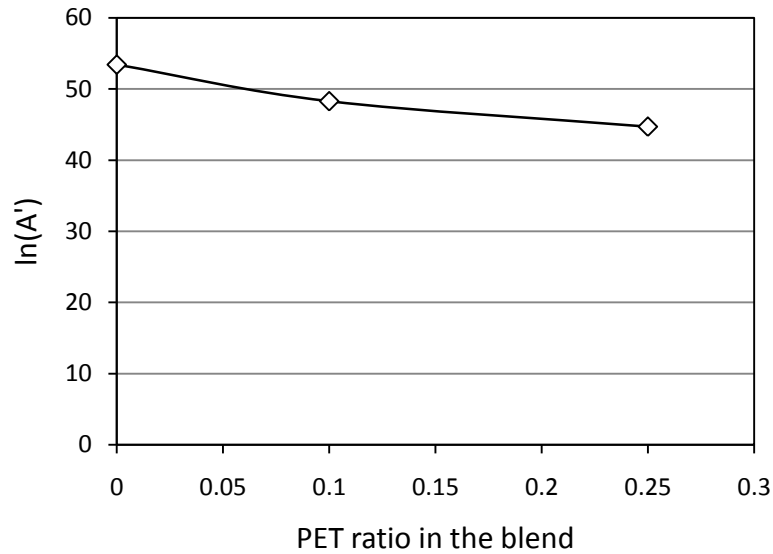


**Figure 7-4 Frequency factor for blends of PBT/PET 100/0, 90/10, 75/25**

Table 7-1 presents the results achieved from TGA analysis and compares them with results from other sources using Freeman-Carroll method in order to analyze the degradation data.

**Table 7-1 Results obtained from TGA data compared to other references**

Material :	PBT [54]	PBT/PET 100/0 [experiment]	PBT/PET 90/10 [experiment]	PBT/PET 75/25 [experiment]
$E(KJ/Moles)$	250	330	304	281
$n$	2.3	$2.1 \pm 0.3$	$1.5 \pm 0.2$	$1.8 \pm 0.2$
$\ln A' (1/min)$	47	53	48	45

The experimental TGA values of  $m/m_0$  were then predicted for each material using the respective fitted values of  $n$ ,  $E$ , and  $A'$ , Equations 7-13 and a heating rate of 20 K/min. Figure 7-5, Figure 7-6 and Figure 7-7 show the predicted values and the experimental TGA data for

PBT/PET 100/0, 90/10 and 75/25 respectively. The fit of the model to the experimental data is good and serves to validate this modeling approach.

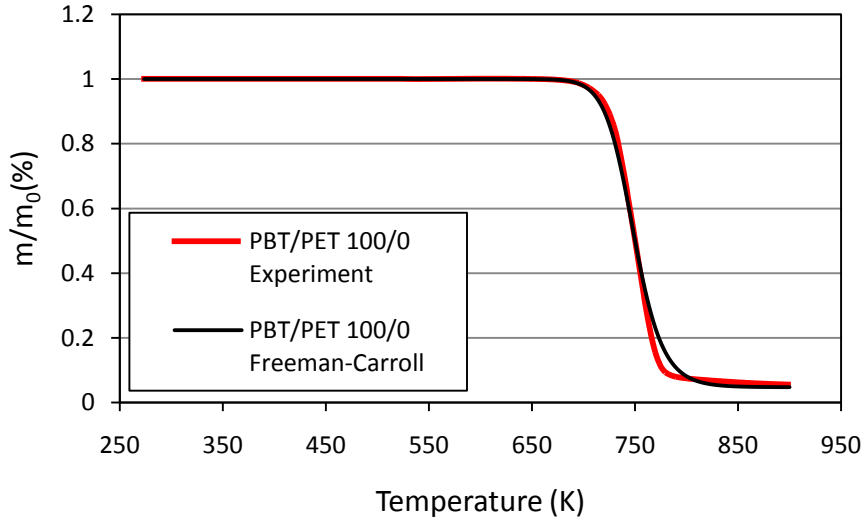


**Figure 7-5 Degradation model validation for PBT/PET 100/0**

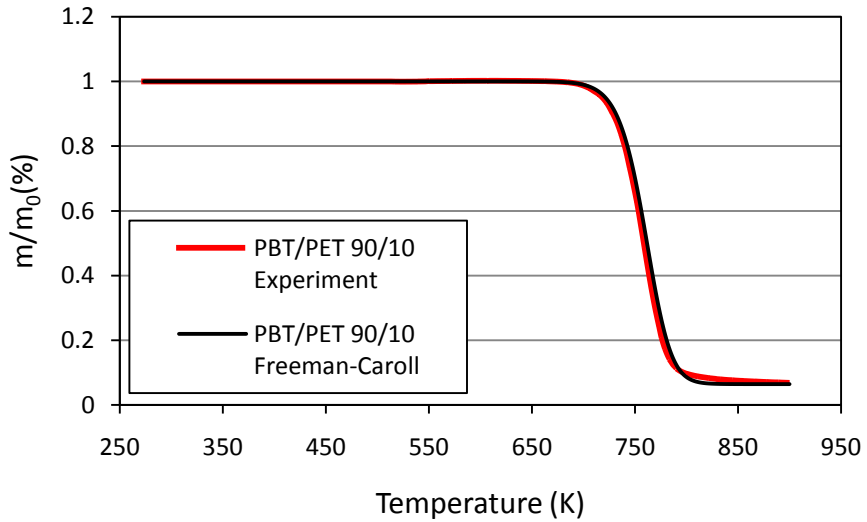


**Figure 7-6 Degradation model validation for PBT/PET 90/10**

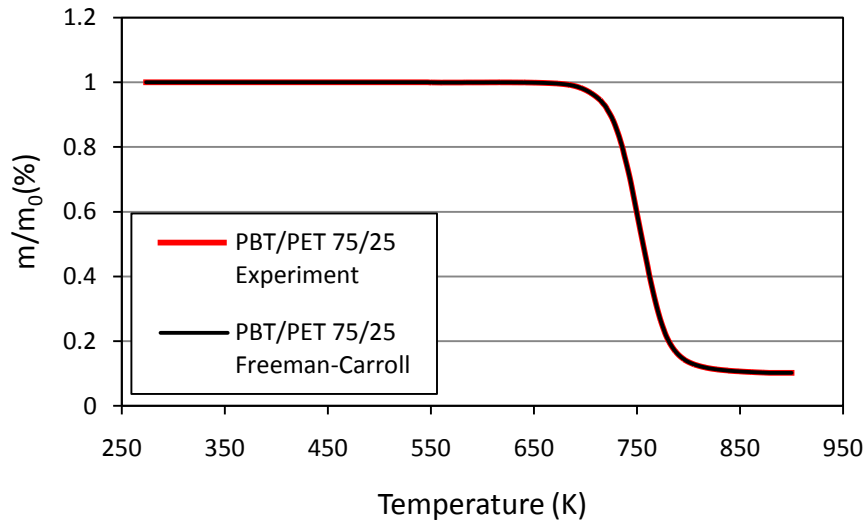


**Figure 7-7 Degradation model validation for PBT/PET 75/25**

The next step is to use the same reaction parameters ( $n$ ,  $E$ , and  $A'$ ) to predict the value of  $m/m_0$  at the weld-line after being exposed to a temperature-time profile predicted by the 2D FEM model. Figure 7-8 shows the temperature-time profile predicted during a laser scan at  $P=100\text{W}$  at a speed of  $1000\text{ mm/min}$  for PBT. A maximum temperature near  $700^\circ\text{C}$  is predicted during the process; however, the high temperature lasts for a very short time. As shown in Figure 7-1, such temperature can degrade the interface; however, since the interface experiences this temperature for a fraction of a second, the question is how much has degraded during this process. Similar temperature profiles were developed for the three materials at a range of powers between  $75$  and  $105\text{ W}$  at a constant scan speed of  $1000\text{ mm/min}$ . These temperature-time profiles are found in Appendix E.

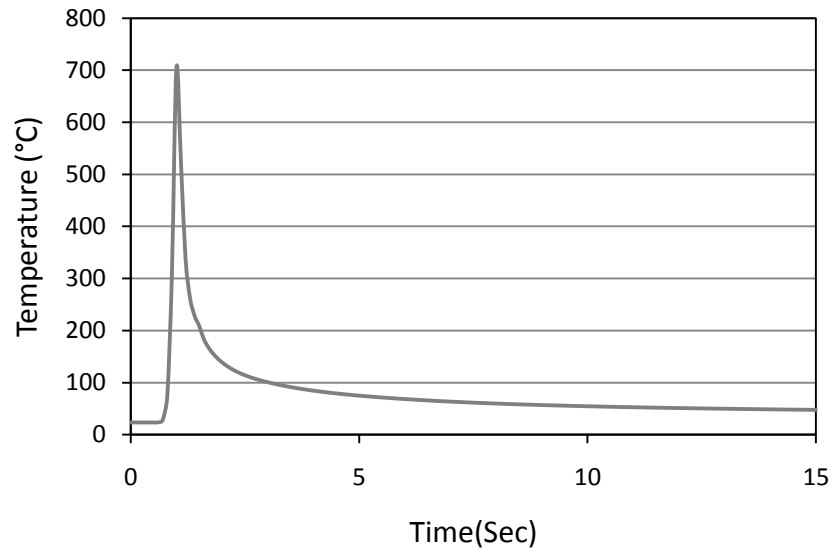


**Figure 7-8 Temperature predicted by the FE model for a laser scan for PBT at 100 W**

Figure 7-9, Figure 7-10, and Figure 7-11 show the fraction of non-degraded ( $m/m_o$ ) material for three blends of PBT/PET 100/0, 90/10 and 75/25 for each power level.

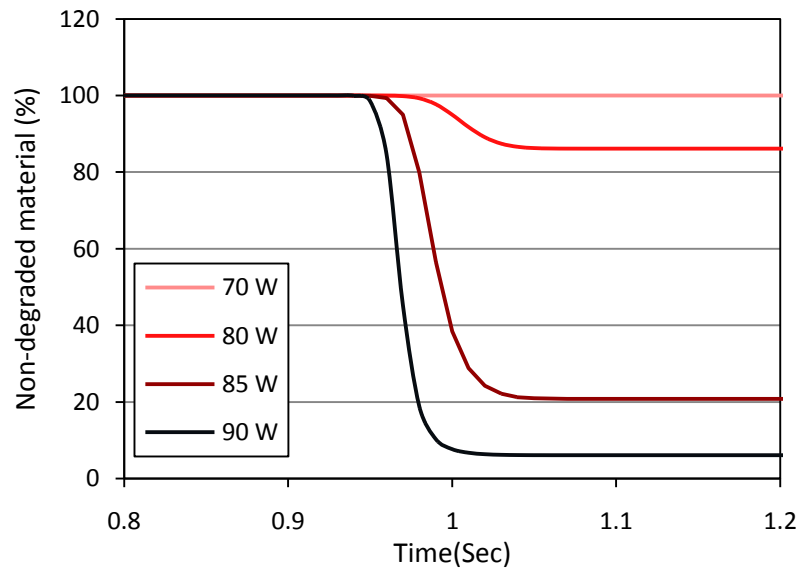


**Figure 7-9  $m/m_o$  at different powers as a function of time for PBT/PET 100/0**

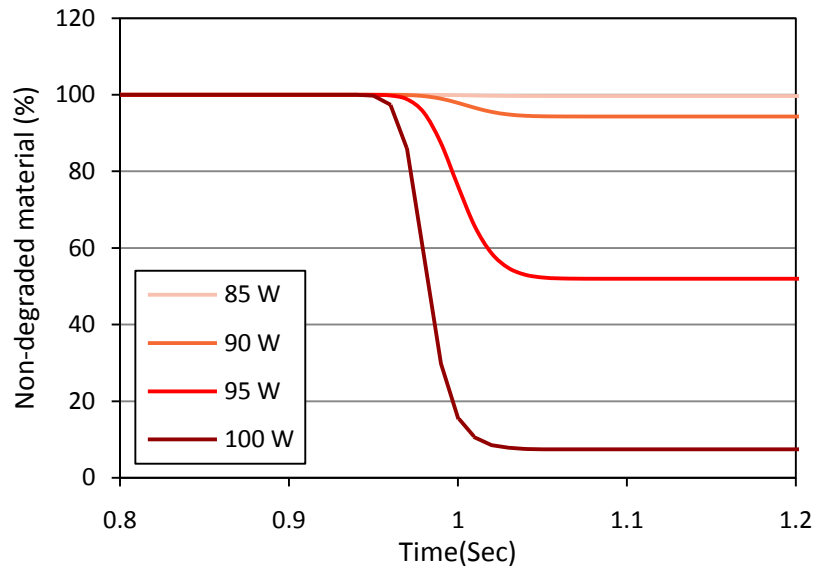


**Figure 7-10  $m/m_o$  at different powers as a function of time for PBT/PET 90/10**

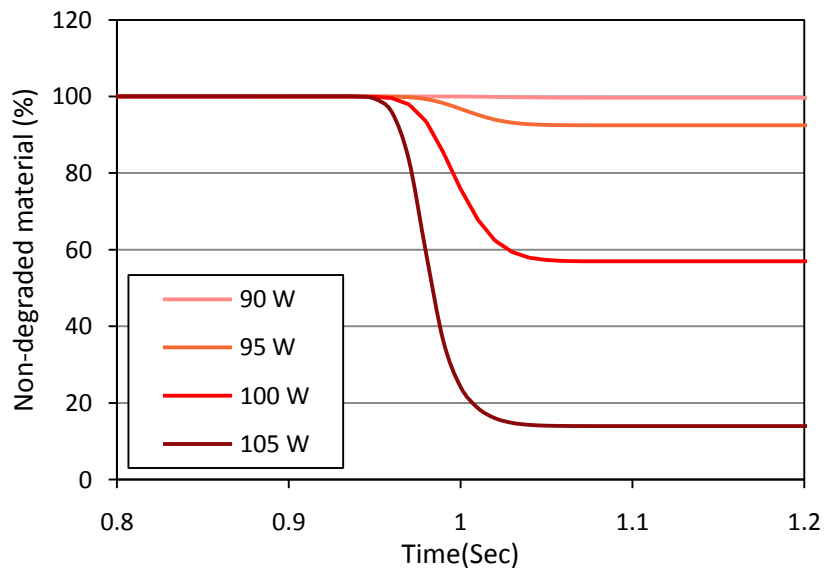


**Figure 7-11  $m/m_o$  at different powers as a function of time for PBT/PET 75/25**

Figure 7-9, Figure 7-10, and Figure 7-11 show that degradation is dependent on laser power and time at a constant speed of 1000 mm/min. For all three blends, no significant

degradation (above 1%) was observed up to approximately 80W. The power at which significant degradation started was in the range of 80-95 W depending on the level of PET. As expected from the TGA results, increasing the PET level increases the power level at which degradation is predicted. Comparing the degradation data with the strength test study in Chapter 5, it can be seen from Figure 7-12 that the weld strength starts to decline at powers in the range of 80-95 W, where significant degradation is predicted by this model. These results are very encouraging as they allow the upper power limit to be rationally estimated using a simple kinetic model. More work is however necessary to confirm its validity with other polymers

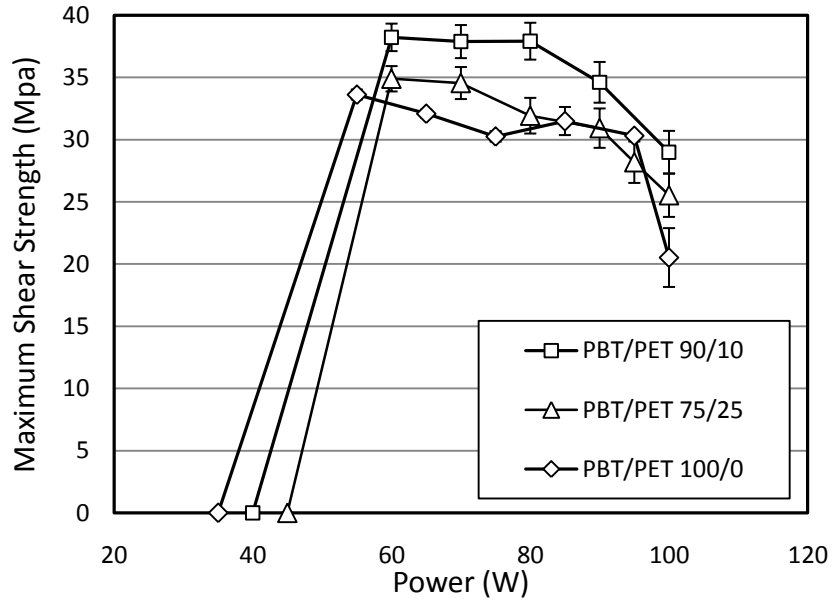


**Figure 7-12 Shear strength as a function of power for three blends of PBT/PET**

## Chapter 8

### **Conclusions and Recommendations**

#### **8.1 Conducted Work**

Three different blends of polybutylene terephthalate and polyethylene terephthalate (PBT/PET) were studied in this work. The scattered beam profile of these materials was measured experimentally using TEDD technique. In order to reach the total NPDF profiles, Chen's method of modeling beam profile was adapted. The results from this study were used as input for the 2-D FEM thermal model in order to determine the temperature distribution inside the polymer bulk during laser welding. This model predicted a temperature-time profile that subsequently was used in a simple degradation model to estimate the degradation occurring during laser welding.

#### **8.2 Contributions**

Following are the major contributions of this work:

- Examination of a range of PBT/PET blends as a material for Laser Transmission Welding for the first time
- Application of the Chen's model of laser beam scattering in order to estimate more accurately the beam profiles after passing through the laser-transmitting part
- Development of a novel model by which thermal degradation at the weld interface can be predicted. This can help to identify more accurately and reliably the welding process window and to achieve optimum weld strengths

### 8.3 Conclusions

The results obtained through the NIR spectrophotometer study showed that transmission decreases slightly with increasing level of PET in the blend. Increase in PET ratio also increases the absorption. This might be due to higher aromatic content of PET in comparison with PBT; however, this may be slightly offset by lower total reflection of blends containing higher levels of PET.

Using the Transverse Energy Density Distribution (TEDD) technique for determining the beam profiles of transmitted laser beam shows that all of the materials scattered significantly more than other unfilled semicrystalline polymers such as PA. This may be due to the larger difference between refractive indices in the amorphous and crystalline phases of both base materials and the blends. This is consistent with the high total reflection of these materials compared to polymers such as nylon. It is also consistent with the increase in scattering observed with glass-fibre-reinforced polymers.

No significant difference in scattering was observed between 3 blends using the TEDD technique. This may be due in part to difficulties measuring  $P_0/P_k$  vs.  $w_k/2$ . A modified technique was developed to partially overcome this issue. It used a semi-empirical approach developed by Chen to estimate the shape of the scattered beam from information related to the initial beam shape.

Data on the threshold power required to cause melting as well as the melt width on a PA surface also suggest that blends of PET actually increase scattering. However the increased absorption in these transparent blends may also be responsible for these phenomena.

Power required forming a weld increased as PET ratio in the blend increased. This is due to higher melting point of PET and due to increase in absorption. Similarly at any given power, the weld width was always larger for pure PBT.

All PBT/PET materials exhibited maximum weld strength in the 34-39 MPa range. The highest strength was observed with the two blends containing PET with 90/10 giving the best results. This is partially due to the lower weld width at any given power and also due to increase in thermal stability of blends containing PET. In all three cases, the weld strength started to drop with further increase in laser power. This was due to degradation occurring at the weld interface as pointed out in previous studies.

Deformation of the incident surface of the transparent part was observed in blends containing PET. Small ribs were formed and became progressively larger as either the line energy or PET level was increased. Due to its higher absorption, blends containing higher levels of PET may locally melt/soften resulting in the observed deformation.

Methods such as Freeman-Carroll can provide a reasonable estimation of the onset of thermal degradation at weld interface. Historically, thermal modeling could predict the conditions required for the onset of welding, Now by combining the temperature distribution at given positions at different times with the degradation model provided by the Freeman-Carroll method on TGA data, a better estimate of the processing window can be obtained.

#### **8.4 Recommendations**

It is recommended that the beam profile for these materials be measured by TEDD technique using black materials with lower melting temperatures. This results in lowering the threshold power of melting and consequently covering the larger fraction of the beam profile. The

model presented in this work can then be used to determine the NPDF profiles with higher precision.

TGA analysis can be conducted followed by application of the proposed model in order to predict the degradation occurring at the weld interface for materials other than the ones studied in this thesis. It would also be helpful to investigate other polymer thermal degradation models and compare them with Freeman Carroll method to select the best model that can interpret degradation caused by laser welding.

## **Bibliography**

- [1] Chen, M. (2009). *Gap Bridging in Laser Transmission Welding of Thermoplastics*. Kingston: Queen's University, Department of Mechanical Engineering.
- [2] *Laser Plastic Welding - The latest evolution in joining technology from the leading system supplier*. (n.d.). Retrieved from [http://www.laserquipment.com/\\_mediafiles/1787-neue-themenbroschuere-englisch.pdf](http://www.laserquipment.com/_mediafiles/1787-neue-themenbroschuere-englisch.pdf)
- [3] Blais, L. (2009). *Introduction to Laser Welding*. Quebec: Centre Specialise de Technologie Physique du Quebec inc.
- [4] Engen, P. v., Lupp, F., Bolognese, L., Hempel, M., Palfelt, B., Bachmann, F., et al. (2009). *New Advances in Polymer Laser Welding*. DSM Co.
- [5] Prabhakaran, R., Kontopoulou, M., Zak, G., Bates, B. J., & Baylis, B. K. (2006). Contour Laser – Laser-Transmission Welding of Glass Reinforced Nylon 6. *Journal of Thermoplastic Composite Materials, Vol.19* , 427-333.
- [6] Kristskiy, A., Zak, G., & Bates, P. (2009). Laser Welding of Nylon Tubes to Plates Using Conical Mirrors. *ANTEC* , 1289-1294.
- [7] Baumer, S. (2005). *Hanbook of Plastic Optics*. Wiley-VCH.

- [8] Zak, G., Mayboudi, L., Chen, M., Bates, P. J., & Birk, M. (2010). Weld line transverse energy density distribution measurement in laser transmission welding of thermoplastics. *Journal of Materials Processing Technology*, Vol. 210, No. 1 , 24-31.
- [9] Ion, J. C. (2005). *Laser Processing of engineering materials*. Elsevier.
- [10] Potente, H., & Becker, F. (2002). A Step Toward Better Understanding The Heating Phase of Laser Transmission Welding. *Polymer Engineering and Science* , 365-374.
- [11] Prabhakaran, R., Kontopoulou, M., Zak, G., Bates, P., & Baylis, B. (2004). Laser Transmission Welding of Unreinforced Nylon 6. *ANTEC* , 1205-1209.
- [12] Rhew, M., Mokhtarzadeh, A., & Benatar, A. (2003). Diode laser characterization and measurement of optical properties of polycarbonate and high-density polyethylene. *ANTEC* , 1056-1060.
- [13] Ilie, M., Kneip, J. -C., Mattei, S., Nichici, A., Roze, C., & Girasole, T. (2007). Thorough-transmission laser welding of polymers - temperature field modeling and infrared investigation. *Infrared Physics & Technology* 51 , 73-79.
- [14] Mayboudi, L., Chen, M., Zak, G., Birk, A., & Bates, P. (2006). Characterization of Beam Profile for High-Power Diode Lasers With Application to Laser Welding of Polymers. *ANTEC*, (pp. 2274-2276).

- [15] Russek, U. A. (2003). Innovative trends in laser beam welding of thermoplastics. *the 2nd international WLT-Conference on Laser in Manufacturing* (pp. 105-111). Munich: LIM.
- [16] David, D. J., & Misra, A. (2000). *Relating Materials Properties to Structure*. Lancaster, Pennsylvania: TECHNOMIC.
- [17] Shabana, H. M. (2004). Refractive index-structure correlation in chemically treated polyethylene terephthalate fibres. *Polymer Testing* 23 , 291-297.
- [18] Kalfoglou, N. K., & Papadopoulou, C. P. (1997). Blends of an Amorphous Copolyester with Poly(butylene Terephthalate). *Eur. Polym. J. Vol.33, No.2* , 191-197.
- [19] Chang, C. L., Chiu, W. Y., Hsieh, K. H., & Ma, C. -C. (1993). The Molecular Orientation and Mechanical Properties of Poly(ethylene Terephthalate) Under Uniaxial Extension. *Journal of Applied Polymer Science, Vol.50* , 855-862.
- [20] Hsu, S. L., & Chang, C. (1985). Spectroscopic Analysis of Poly(p-phenylene benzobisthiazole) Films. *Journal of Polymer Science: Polymer Physics Edition, Vol. 23* , 2307-2317.
- [21] Wang, C. Y., Bates, P. J., & Zak, G. (2009). Optical properties characterization of thermoplastics used in laser transmission welding: Transmittance and reflectance. *ANTEC* , 1278-1282.

- [22] Bates, P. J., Druart, M. -E., Chen, M., Zak, G., & Billiet, J. (2007). Influence of Part Thickness, Glass Fiber content and Line Energy on Laser Transmission Welding of Polyamide mXD6. *ANTEC* , 2783-2787.
- [23] Potente, H., & Becker, F. (2002). A Step Towards Understanding the Heating Phase of Laser Transmission Welding in Plastics. *Polymer Engineering and Science, Vol.42 (2)* , 365-374.
- [24] Vegte, E. v., Gulp, M. v., Hoekstra, H., & Stroeks, A. (2007). Engineering Plastics for Laser Welding. *ANTEC* , 1899-1905.
- [25] Jacques, S. L., & Prahl, S. A. (1998). Mie theory model for tissue optical properties. *ECE532 Biomedical Optics* .
- [26] Ilie, M., Kneip, J. -C., Mattei, S., Nichici, A., Roze, C., & Girasole, T. (2007). Laser beam scattering effects in non-absorbent inhomogenous polymers. *Optics and Lasers in Engineering 45* , 405-412.
- [27] Ilie, M., Cicala, E., Grevey, D., Mattei, S., & Stoica, V. (2009). Diode Laser Welding of ABS: Experiments and Process Modelling. *Optics and Laser Technology 41,5* , 608-614.
- [28] Aden, M., Roesner, A., & Olowinsky, A. (2010). Optical Characterization of Polycarbonate: Influence of Additives on Optical Properties. *Journal of Polymer Science: Part B: Polymer Physics, Vol. 48* , 451-455.

- [29] Uemura, Y., Chikaishi, K., & Yamazaki, T. (1979). Mie Scattering from Sphere Structures in Polymer Blends. *Journal of Applied Polymer Science, Vol.23* , 2695-2699.
- [30] Haferkamp, H., Busse, A. v., Haberstroh, E., Bunte, J., Hustedt, M., & Lutzeler, R. (2004). Utilisation of a thermo graphic process in order to mine the deterministic laser weldability of plastics at different wavelengths. *Welding and Cutting 3* , 43-49.
- [31] Chen, M., Zak, G., & Bates, P. J. (2005). Laser absorption coefficient measurement of amorphous polymer for Laser Transmission Welding. *ANTEC* , 2291-2295.
- [32] Kagan, V. A., Bray, R., & Chambers, A. (2003). Forward to better understanding of optical characterization and development of colored polyamides for the infra-red/laser welding: Part I - Efficiency of polyamides for infrared welding. *Journal of Reinforced Plastics and Composites, Vol. 22, No. 6* , 533-547.
- [33] Kagan, V. A., Bray, R. G., & Kuhn, W. P. (2002). Laser Transmission Welding of semi-crystalline thermoplastics - Part I: Optical Characterization. *Journal of Reinforced Plastics and Composites, 21(12)* , 1101-1122.
- [34] Busse, A. v., Fargas, M., & Bunte, K. (2005). Optimization of Laser Transmission Welding of Polymers Using Thermography. *ANTEC* , 1014-1018.
- [35] Chen, M., Zak, G., Bates, P. J., Baylis, B., & McLeod, M. (2007). Method of Evaluating Shear Strengths in Contour Laser Transmission Welding. *SAE International, Paper # 2007-01-0571* .

- [36] Schulz, J., & Haberstroh, E. (2000). Welding of polymerers using a diode laser. *ANTEC* , 1196-1199.
- [37] Grewell, D., Jerew, T., & Benatar, A. (2002). Diode Laser Microwelding of Polycarbonate and Polystyrene. *ANTEC* , 1039-1044.
- [38] Chen, M., Zak, G., Bates, P. J., Kamal, M. R., & Al-Wohoush, M. (2009). Finite Element Modeling and Microstructure Analysis for Contour Laser Transmission Welding of Glass Fibre Reinforced Nylon 6. *ANTEC* , 1295-1300.
- [39] Speka, M., Mattei, S., Pilloz, M., & Ilie, M. (2008). The infrared thermography control of the laser welding of amorphous polymers. *NDT&E International 41* , 178-183.
- [40] Greiger, M., Frick, T., & Schmidt, M. (2009). Optical properties of plastics and their role for the modeling of the laser transmission welding process. *Prod. Eng. Res. Devel* , 49-55.
- [41] Mayboudi, L., Zak, G., Birk, A., & Bates, P. (2007). A 3-D Thermal Model of Laser Transmission Contour Welding for a Lap Joint. *ANTEC* , 2813-2817.
- [42] Fried, J. R. (1995). *Polymer Science and Technology*. Prentice Hall.
- [43] Ravve, A. (1995). *Principles of Polymer Chemistry*. New York: Plenum Press.
- [44] *PBT Polybutylene Terephthalate Process*. (n.d.). Retrieved from Lurgi GmbH: [http://www.lurgi.com/website/fileadmin/pdfs/brochures/PBTProcess\\_en.pdf](http://www.lurgi.com/website/fileadmin/pdfs/brochures/PBTProcess_en.pdf)

- [45] Shi, Y., & Wu, M. (1995). Synthesis and properties of Poly(tetramethylene)-co-ethylene terephthalate)-poly(tetramethylene ether) segmented copolymers. *Polymer International* 0959-8103/95 , 357-363.
- [46] Run, M., Song, A., Wang, Y., & Yao, C. (2008). Melting, Crystallization Behaviors, and Nonisothermal Crystallization Kinetics of PET/PTT/PBT Ternary Blends. *Journal of Applied Polymer Science*, Vol.104 , 3459-3468.
- [47] Jacques, B., Devaux, J., Legras, R., & Nield, E. (1996). NMR Study of Ester-Interchange Reactions during Melt Mixing of Poly(ethylene terephthalate)/Poly(butylene terephthalate) Blends. *Journal of Polymer Science: Part A: Polymer Chemistry* , Vol 34, 1189-1194.
- [48] DSM. (2005). *PBT & PET Polyesters General Information on Properties*. DSM Engineering Plastics.
- [49] *DSM Engineering Plastics - Arnite (R) A06 300 (PET), Arnite (R) T06 200 (PBT)*. (2010). Retrieved from Campus Plastics:  
<http://www.campusplastics.com/en/datasheet/Arnite%C2%AE+A02+306/DSM+Engineering+Plastics/50/3a313e2c>
- [50] Ethrenstein, G. W., Riedel, G., & Trawiel, P. (2004). *Thermal Analysis of Plastics, Theory and practice*. Munich: Hanser Gardner.

[51] Segal, E., & Fatu, D. (1976). Some variants of the Freeman-Carroll method. *Journal of Thermal Analysis and Calorimetry* , 65-69.

[52] Montaudo, G., Puglisi, C., & Samperi, F. (1993). Primary thermal degradation mechanisms of PET and PBT. *Polymer degradation and stability* 42 , 13-28.

[53] Samperi, F., Puglisi, C., Alicata, R., & Montaudo, G. (2004). Thermal degradation of poly(butylene terephthalate) at the processing temperature. *Polymer degradation and stability* 83 , 11-17.

[54] Li, F., Xu, X., Li, Q., Li, Y., Zhang, H., Yu, J., et al. (2006). Thermal degradation and their kinetics of biodegradable poly(butylene succinate-co-butylene terephthalate)s under nitrogen and air atmospheres. *Polymer degradation and stability* 91 , 1685-1693.

## Appendix A

### A.1- Thermal Properties

Thermal properties of the materials are one of the major concerns in thermal modeling of laser transmission welding. The general differential equation of temperature distribution at the weld interface of the parts during laser welding is:

$$k\nabla^2 T + c\rho \frac{\partial T}{\partial z} + Q = 0 \quad \text{Equation A-1}$$

Where  $k$  is the thermal conductivity of the sample;  $c$  is the specific heat capacity and  $\rho$  is the density of the sample. According to this equation, parameters such as thermal conductivity, density, and heat capacity play a major role on solving this equation.

#### - Heat Capacity

The heat capacities for three blends of PBT/PET with ratios of 100/0, 90/10 and 75/25 were measured by Modulated Differential Scanning Calorimetry (MDSC) using a DSC Q100 V9.9 manufactured by TA instrument located at Dupuis hall, Queen's university was used in order to determine the heat capacity variation of the samples over a range of temperatures between 20°C to 275°C. 275°C is 50°C above the melting temperature of PBT, and 25°C above the melting temperature of PET. The results are shown in Figure A-1. Heat capacity and latent heat data from this figure are summarized in Table A-1.

Table A-1 Thermal properties of the blends based on DSC studies

Property	Units	PBT/PET (100/0)	PBT/PET (90/10)	PBT/PET (75/25)
$c$ at 25°C	J/g K	1.546	1.271	1.308
$c$ at 265°C	J/g K	2.280	2.200	2.018
Melting point of PBT phase	°C	225	225	225-255
Enthalpy of melting of PBT	J/g	45.18	37.82	27.3
Melting point of PET phase	°C	-	255	255
Enthalpy of melting of PET	J/g	0	5.2	15.58

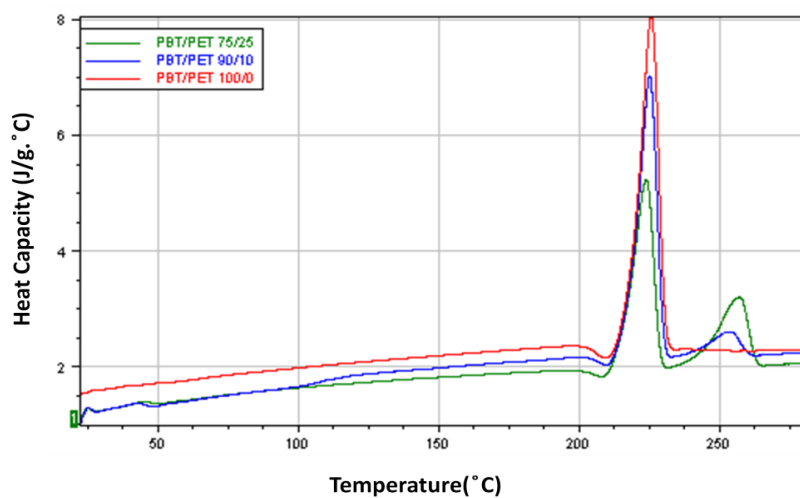


Figure A-1 Heat capacity variation at different temperatures resulted from MDSC for three blends

The results achieved from experimental studies, agrees with the values from the literature review [49].Based on these results it can be seen that by adding more PET to the blend, the latent heat of melting at the melting point of the PBT starts to decline and that of the PET starts to increase.

- Heat Conductivity

Thermal conductivity is the amount of heat that passes in unit time through a plate with particular area and thickness, in order to provide one Kelvin temperature difference with the other side of the plate. The values reported at different references indicated the thermal conductivity for the melting phase of both PBT and PET [49]. Therefore it was necessary to determine the thermal conductivity variation in the solid phase as well. For this reason, experiments were conducted over a temperature range of 32~105°C using thermal conductivity instrument UNITHERM™ Model 2022 (Anter Corporation) at RMC following ASTM E1530. The results are shown in Table A-2, Table A-3 and Table A-4. It is observed that the thermal conductivity of each blend at solid phase is twice as big as the conductivity at the melting phase provided by other references.

**Table A-2 Thermal conductivity for the range of 31~104°C for PBT/PET 100/0**

Material		Temperature (°C)	Thermal Conductivity K, W/(m K)
PBT/PET 100/0	Measured	31	0.185
		47	0.217
		64	0.231
		84	0.234
		104	0.241
		Average for solid ( $\leq 225$ )	0.2216
	Reference	Melting ( $\geq 225$ )	0.109

**Table A-3 Thermal conductivity for the range of 31~104°C for PBT/PET90/10**

Material		Temperature (°C)	Thermal Conductivity K, W/(m K)
PBT/PET 90/10	Measured	32	0.230
		47	0.235
		65	0.252
		84	0.247
		104	0.242
		Average for solid ( $\leq 225$ )	0.241
	Reference	Melting ( $\geq 225$ )	0.1221

**Table A-4 Thermal conductivity for the range of 31~104°C for PBT/PET 75/25**

Material		Temperature (°C)	Thermal Conductivity K, W/(m K)
PBT/PET 75/25	Measured	31	0.247
		47	0.252
		64	0.262
		84	0.260
		104	0.267
		Average for solid ( $\leq 225$ )	0.257
	Reference	Melting ( $\geq 225$ )	0.142

- Thermal Expansion Coefficient

The density value for each blend varies at different temperature due to the non-zero thermal expansion coefficients for both materials [49]. The density of a material can be defined by equation A-2:

$$\rho = \frac{\rho_{ref}}{1 + 3\alpha(T - T_{ref})} \quad \text{Equation A-2}$$

Where  $\rho_{ref}$  is the density value at reference temperature ( $T_{ref}$ ); and  $\alpha$  is the linear thermal expansion coefficient. It is assumed the reference density, and the thermal expansion coefficient of each blend, vary linearly with increasing the ratio of the PET in the blend. It should also be noted that the thermal expansion coefficient itself, varies with temperature. Figure A-2 shows the temperature dependence of this parameter for both base materials [50].

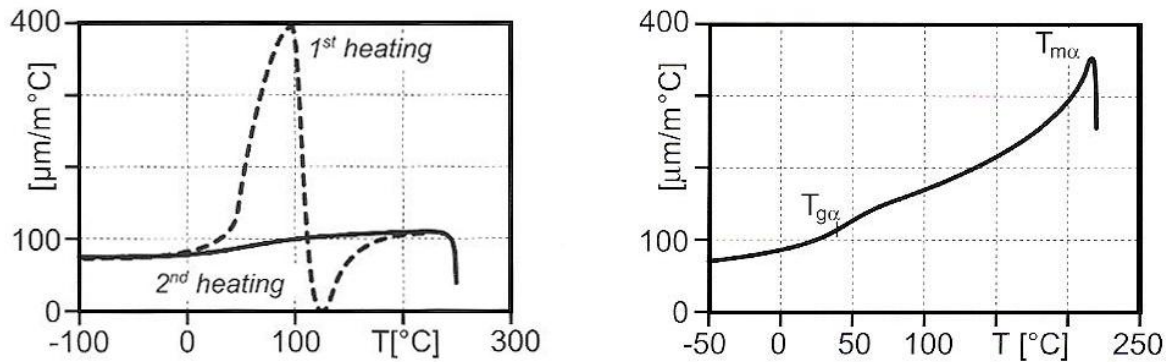


**Figure A-2 Linear expansion coefficient vs. temperature for PET(left) and PBT(right)**

## Appendix B

This appendix presents a MATLAB code which was used in order to generate parameters such as  $\delta$ ,  $\sigma$  and  $1/\Psi^*(0)$  that can define the beam profile of the scattered beam after passing through the polymer bulk of the transparent part.

```
function element_maker(data)

%-----^^^-----
%
% In this part , the coefficients for the EXP function inside the sum
% are made and added to an array called "data_new" in order to keep the
% original data array , untouched.
%-----^^^-----
%
clc

%Defining Constants and Variables:

sigma2=0;
upperend=5; %The Far right end of the scattered beam profile (mm)
lowerend=5; %The far left end of the scattered beam profile (mm)
Constant_Grid=500 ;
MAX_Sigma =3 ;
MAX_Taw =4;
Estimated_Scattered_Power=0;
Estimated_Direct_Power=0;
%Delta=0.95;
Descretized_Power_Ratio=1/26; %The beam is divided into 26
descretized beams
Scan_Speed=1/60; % Equal to 1000 mm/min (The operation
speed)
Descretized_Beam_Width=2.65/26; %The maximum length of the beam coming
from the laser head is divided into the number of descretized beams
Flag=1 ;
Flag2=0;
Value = 0;
j=1;
Initial_Power=0 ;
EXCEL1=0;
Plot_Precision=0.1 ;
Sum_of_Power_Ratio=0;
Average_Power_Ratio=0;
```

```

Power_Ratio= 0 ;
%-----^^^-----
-
%During the while, it checks if we've reached to the end of the data
table
%by checking whether the po/pi of the jth datapoint is equal to one or
not
%then after the while , j is reported as the number of the measured
%datapoints in the function
%-----^^^-----
-

while (data(j,3)~=1)
    j=j+1;
    Sum_of_Power_Ratio=Sum_of_Power_Ratio+data(j,3) ;
end
Total_Datapoints=j*2;
Average_Power_Ratio=Sum_of_Power_Ratio/j ;
data_new=data;

j=1 ;
while (data(j,6)~=0)
    j=j+1;
end
Total_Unscattered_Beam_Points=j;
%-----^^^-----
-
% Generating the constant values to the power of the exp function
inside
% the summation. Since the X values or the melt widths are measured and
% are saved in the input array of the program , the values of the power
% of the EXP part of the Gaussian function are calculated and later on
% going to be divided by the assumed Sigma values.
%-----^^^-----
-
for j=1:Total_Datapoints
    for i=8:8+Total_Unscattered_Beam_Points
        data_new(j,i)=-((data_new(j,4)-data_new(i-7,6))^2)/2 ;
    end
end

%-----^^^-----
--
% Checking whether the user wants to enter the values for Sigma, Delta
& & Tau
% manually or wants it to be measured by certain grid.
%-----^^^-----
--
while (Flag~=0)
    clc

```

```

ans=input('Would you like to enter the values for Sigma & Taw
manually ?[Y/N] ', 's');
if ((ans=='Y') | (ans=='y'))
    clc;
    sigma2=input('Enter the value for scattering standard
deviation(Sigma): ');
    Delta2=input('Enter the value for scattering
coefficient(Delta): ');
    taw2=input('Enter the value for the scaling factor(Taw): ');
    Flag=0;
end
if ((ans=='N') | (ans=='n'))
    Constant_Grid=input('Please enter the mesh for calculating
Sigma,Delta and Taw: ');
    Flag=0;
end
end
%-----^^^-----
% In this part , a matrix of estimated values for the power intensity
% is made by variance of Sigma and Taw , between 0.1 to 5 in 0.1 steps
% then the sum of squares matrix is made at different Sigma & Taw.
%-----^^^-----

%-----
%Initial values for Sigma , Taw , and F(x):
min_value(1,1)=4; % Sigma
min_value(1,2)=1.0*Constant_Grid; % Taw
min_value(1,3)=100; % Least Square
min_value(1,4)=0; % Delta
%-----

clc
summation =0;
Area = 0;
CTR = 1 ;
MAX_delta=1;

if ((ans=='N') | (ans=='n'))
    disp('Calculating the minimum sum of squares in respect to various
values for Sigma and Taw...')
    for taw=1:MAX_Taw*Constant_Grid
        for sigma=1*Constant_Grid:MAX_Sigma*Constant_Grid
            for Delta=0.92*Constant_Grid:(MAX_delta*Constant_Grid-1)
                %-----
                for i=1:Total_Datapoints

Scattered_Constant=(Delta/Constant_Grid)*Descretized_Beam_Width*(1/sqrt
(2*pi))*(1/(sigma/(Constant_Grid))) ;
                    summation =0;
                    for j=1:Total_Unscattered_Beam_Points
                        summation=summation +
data_new(j,7)*exp(data_new(i,j+7)/((sigma/(Constant_Grid))^2));
                    end
                end
            end
        end
    end
end

```

```

        sum = summation ;
        Estimated_Scattered_Power =Scattered_Constant*sum_ ;
        for q=1:Total_Unscattered_Beam_Points-1
            if data_new(i,4)>data_new(q,6) &&
data_new(i,4)<data_new(q+1,6)
                Value=data_new(q,7)+(data_new(q,6)-
data_new(i,4))*(data_new(q+1,7)-data_new(q,7))/(data_new(q,6)-
data_new(q+1,6));
                Estimated_Direct_Power=(1-
(Delta/Constant_Grid))*Value;
            end
        end
        if data_new(i,4)<data(1,6) ||
data_new(i,4)>data(Total_Unscattered_Beam_Points-1,6)
            Estimated_Direct_Power=0 ;
        end
        Total_Estimated_Power
=(Estimated_Scattered_Power+Estimated_Direct_Power)*(1/(taw/Constant_Gr
id)) ;
        tmp(i)=(data_new(i,3)-Total_Estimated_Power)^2 ;      %
tmp(i) = Squared difference of the estimated values and the measured
ones
        end
        %-----Ending the Total Data points loop-----

Y_Final(sigma+1,Delta+1)=sum(tmp(1:Total_Datapoints))/(Total_Datapoints
-3) ; % Y_Final is the sum of square for each Sigma and Delta value
z=sum(data_new(1:Total_Datapoints,3)-
Average_Power_Ratio)^2/(Total_Datapoints-1);
        if Y_Final(sigma+1,Delta+1)<min_value(CTR,3)
            CTR=CTR+1 ;
            min_value(CTR,1)=sigma/Constant_Grid ;
            min_value(CTR,2)=1/(taw/Constant_Grid) ;
            min_value(CTR,3)=Y_Final(sigma+1,Delta+1);
            min_value(CTR,4)=Delta/Constant_Grid;
            min_value(CTR,5)=1-Y_Final(sigma+1,Delta+1)/z;
            Flag2=0;
        end
    end
    %-----Ending the Delta loop-----
end
%-----Ending the Sigma loop-----
end
%-----Ending the Taw loop-----
disp('Scattering standard deviation(Sigma):'); % Sigma
disp(min_value(CTR,1));
disp('Scattering scaling factor(Taw):'); % Taw
disp(min_value(CTR,2));
disp('Sum of Square :'); % Sum of square
disp(min_value(CTR,3));
disp('Scattering coefficient(Delta):'); % Delta
disp(min_value(CTR,4));

```

```

disp('Press any key to continue...');
disp('RSquare:'); % Rsquare
disp(min_value(CTR,5));
disp('Press any key to continue...');

pause ;

%-----^^^-----
%   Checking if the user wants to save the data in an Excel spreadsheet
%-----^^^-----
Flag=1 ;

while (Flag~=0)
    clc
    ans=input('Would you like to save the values for the least squares
in a spreadsheet ?[Y/N] ','s');
    if ((ans=='Y') | (ans=='y'))
        clc;
        disp('Please Wait...');
        xlswrite('Least_Square',Y_Final);
        disp('The values for least square has been saved in
Least_Square.xml in the same folder.');
```

Least\_Square.xml in the same folder.');

```

        Flag=0;
    end
    if ((ans=='N') | (ans=='n'))
        Flag=0;
    end
end
taw2=min_value(CTR,2) ;
sigma2=min_value(CTR,1);
Delta2=min_value(CTR,4);
end

%-----^^^-----
---
%Measures the estimated NPDF values at the given range and saves the
data
%in the "Estimated_Chart" Array
%-----^^^-----
---
counter=0 ;

for X=-lowerend:Plot_Precision:upperend
    counter=counter+1 ;
    summation =0 ;
    for i=1:Total_Unscattered_Beam_Points
        Xi=1.15-(i-1)*0.1 ;
        di=-((X-Xi)^2)/(2*sigma2^2);
        summation=summation + data_new(i,7)*exp(di);
    end
    for q=1:Total_Unscattered_Beam_Points-1
        if X>data(q,6) && X<data(q+1,6)
```

```

        Value=data_new(q,7)+(data_new(q,6)-X)*(data_new(q+1,7)-
data_new(q,7))/(data_new(q,6)-data_new(q+1,6))
        Estimated_Direct_Power=(1-Delta2)*Value ;

    end
end
if X<data(1,6) || X>data(Total_Unscattered_Beam_Points-1,6)
    Estimated_Direct_Power=0;
end

Scattered_Constant=Delta2*Descretized_Beam_Width*(1/sqrt(2*pi))*(1/sigm
a2) ;
    Estimated_Scattered_Power =Scattered_Constant*summation ;
    Total_Estimated_Power
=(Estimated_Scattered_Power+Estimated_Direct_Power) ;
    Estimated_Chart(counter)= Total_Estimated_Power;
end

X=-lowerend:Plot_Precision:upperend;
%-----=Drawing of the estimated P./Pi Vs X=-----
----
set(gcf,'color',[1 1 1]);
    grid on;
plot(X,Estimated_Chart,'g','LineWidth',2);
title('NPDF')
xlabel('Melting width(mm)')
ylabel('Normalized Power Flux Distribution (NPDF) (1/mm)')
set(gcf,'color',[1 1 1]);

grid on;
grid minor ;
hold on
plot(data_new(1:Total_Datapoints,4),data_new(1:Total_Datapoints,3)/tau2
,'rsquare','MarkerEdgeColor','k','MarkerFaceColor',[0 1
0],'MarkerSize',4)

legend('Beam profile from the model','Experimental data points');
%-----^^^-----
% In this part , the area beneath the curve will be calculated :
counter=0;
for i=-lowerend:Plot_Precision:upperend
    counter=counter+1;
    EXCEL1(counter,1)=i ;
    EXCEL1(counter,2)=Estimated_Chart(counter) ;
end
xlswrite('Excel#3',EXCEL1);
end

```

## Appendix C

The tensile strengths were measured for 8 specimens for each blend following ASTM D638 using type V dogbones injection molded at Royal Military College using a 55-ton Engel injection molder. The cross-head speed was set to 5 mm/min to stay compatible with the cross-head speed during the weld strength test. Figure C-1 is the schematic view of the dogbones made in order to perform the test. The tensile test was performed using INSTRON 4206 Universal testing machine at RMC.

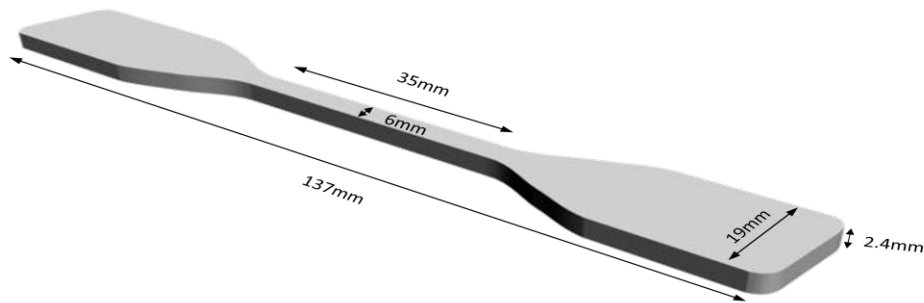


**Figure C-1 Schematic view of injection molded dogbones**

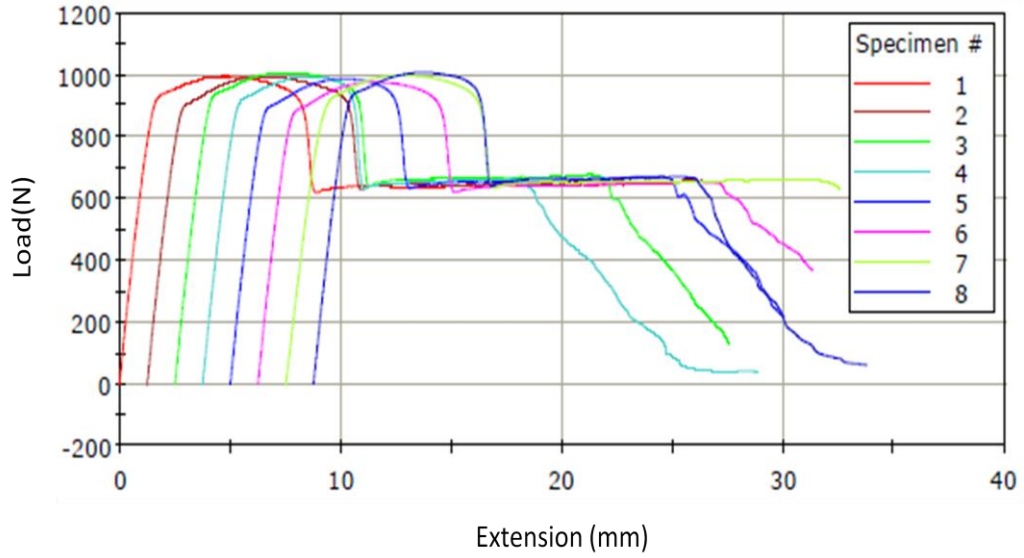


**Figure C-2 Applied load versus the extension for PBT/PET 100/0**

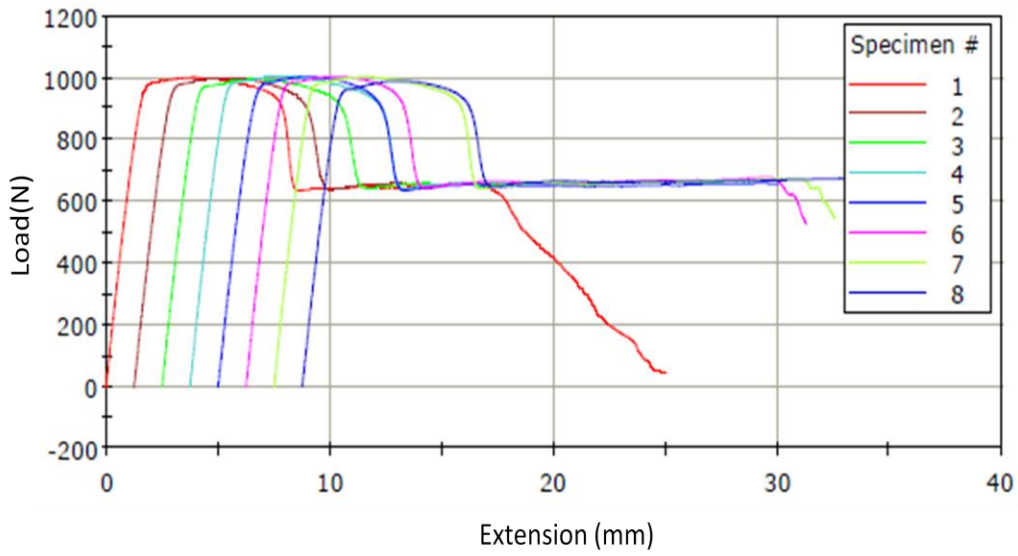


**Figure C-3 Applied load versus the extension for PBT/PET 90/10**

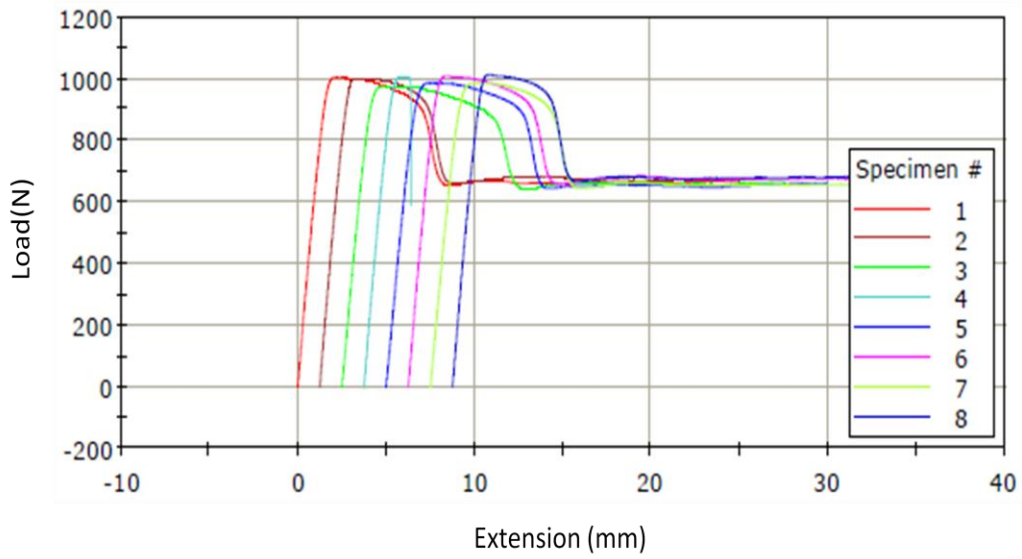


**Figure C-4 Applied load versus the extension for PBT/PET 75/25**

## Appendix D

**Table D-1 Temperature variation at time range of 0.74-1.23 for PBT/PET 100/0**

	<i>P=70W</i>	<i>P=80W</i>	<i>P=85W</i>	<i>P=90W</i>
<b>Time(Sec)</b>	<b>Temperature(K)</b>	<b>Temperature(K)</b>	<b>Temperature(K)</b>	<b>Temperature(K)</b>
0.74	303.7895	304.9059	305.3483	305.7165
0.75	306.2205	307.3921	308.0837	308.6918
0.76	309.0137	310.5456	311.4028	312.2321
0.77	312.3921	314.4457	315.4699	316.5328
0.78	316.4737	319.0939	320.3946	321.7094
0.79	321.3578	324.605	326.2883	327.8778
0.8	327.1827	331.2459	333.3705	335.2459
0.81	334.0083	339.1098	341.5663	344.0624
0.82	341.8561	348.0769	351.2667	354.2277
0.83	350.9381	358.4665	362.2079	366.1431
0.84	361.2114	370.1006	374.5763	379.4902
0.85	372.5334	383.1589	388.5347	394.5607
0.86	385.0701	397.8295	404.4521	411.7183
0.87	398.9473	414.4294	422.6859	431.8094
0.88	414.4081	433.566	443.7965	455.3909
0.89	431.8102	455.6171	469.0003	483.7572
0.9	451.2752	481.7434	493.902	505.6207
0.91	473.3158	500.5503	519.9215	540.6956
0.92	493.7181	523.4255	554.0212	578.5954
0.93	512.0505	558.7626	590.3584	621.7169
0.94	537.7878	597.1314	629.5627	665.2304
0.95	562.4636	631.7169	667.8348	707.8669
0.96	586.4207	662.1191	704.0615	748.1278
0.97	609.4204	690.7047	736.8168	784.648
0.98	629.9322	715.9149	765.0624	815.9684
0.99	647.2391	735.4512	787.582	841.2258
1	659.1946	749.6171	804.0628	859.5105

	<i>P=70W</i>	<i>P=80W</i>	<i>P=85W</i>	<i>P=90W</i>
<b>Time(Sec)</b>	<b>Temperature(K)</b>	<b>Temperature(K)</b>	<b>Temperature(K)</b>	<b>Temperature(K)</b>
1.01	664.8189	758.5075	813.8615	869.9341
1.02	668.3719	761.9261	816.9604	872.7645
1.03	667.6986	760.289	814.4451	869.2996
1.04	663.3506	754.2414	807.041	860.5349
1.05	656.148	744.6282	795.5559	847.3136
1.06	646.6778	732.1176	780.7729	830.3961
1.07	635.5353	717.3821	763.5458	810.8111
1.08	623.2074	701.0713	744.8834	789.6254
1.09	610.1973	683.9678	725.3808	767.6302
1.1	596.9367	666.6831	705.5444	745.4276
1.11	583.7596	649.6007	686.1553	723.695
1.12	570.9446	633.2195	667.7302	703.0187
1.13	558.7597	617.5811	650.1519	683.3427
1.14	547.359	602.8866	633.6857	664.9634
1.15	536.8233	589.2831	618.4545	647.9589
1.16	526.8823	576.8111	604.4216	632.3086
1.17	517.991	565.1648	591.4893	617.9706
1.18	510.7432	554.5233	579.523	604.6275
1.19	505.0243	544.8718	568.586	592.4858
1.2	501.3822	536.0436	558.4122	581.4825
1.21	498.1858	528.021	549.0408	571.4445
1.22	493.8355	520.8694	540.4855	562.2305
1.23	489.7508	514.4145	532.6582	553.757

**Table D-2 Temperature variation at time range of 0.74-1.23 for PBT/PET 90/10**

	<i>P=85W</i>	<i>P=90W</i>	<i>P=95W</i>	<i>P=100W</i>
<b>Time(Sec)</b>	<b>Temperature(K)</b>	<b>Temperature(K)</b>	<b>Temperature(K)</b>	<b>Temperature(K)</b>
0.74	303.6444	304.0648	304.4833	304.8997
0.75	305.7953	306.3291	306.8836	307.4404
0.76	308.7169	309.3627	310.0772	310.798
0.77	312.2835	312.9934	313.8878	314.7953
0.78	316.6972	317.5957	318.7688	319.958
0.79	322.0547	323.23	324.707	326.1965
0.8	328.4189	329.9577	331.7992	333.6582
0.81	335.9	337.8713	340.1282	342.4226
0.82	344.592	347.0854	349.8944	352.7132
0.83	354.6654	357.794	361.1823	364.6332
0.84	366.1221	369.9685	374.0824	378.2567
0.85	379.0976	383.7533	388.6162	393.6242
0.86	393.5297	399.1021	404.9535	410.9514
0.87	409.4317	416.1184	423.0902	430.2835
0.88	426.7923	434.8137	443.076	451.6324
0.89	445.5613	455.1788	464.9431	475.0464
0.9	465.2039	477.324	489.1031	495.3481
0.91	483.7544	502.8661	515.8951	531.1068
0.92	504.6726	532.6367	551.8985	573.0591
0.93	535.026	566.1873	590.1496	615.3381
0.94	567.6664	600.9983	628.4414	657.778
0.95	599.3567	634.794	665.6924	699.2388
0.96	628.566	666.8604	700.7213	738.0725
0.97	654.9434	695.3799	732.084	772.8632
0.98	677.7255	719.7881	759.0259	802.3067
0.99	695.5342	739.4114	780.3784	825.4424
1	708.4774	753.0234	795.6362	841.6903

	<i>P=75W</i>	<i>P=80W</i>	<i>P=85W</i>	<i>P=90W</i>
<b>Time(Sec)</b>	<b>Temperature(K)</b>	<b>Temperature(K)</b>	<b>Temperature(K)</b>	<b>Temperature(K)</b>
1.01	716.5485	761.1068	804.6659	850.8492
1.02	719.4081	764.0181	807.7448	853.203
1.03	717.4349	761.475	804.3817	849.5307
1.04	711.486	754.4751	796.1675	840.1655
1.05	702.2372	743.8064	784.4691	826.3959
1.06	690.3438	730.2896	769.7731	810.0067
1.07	676.6824	714.7175	752.9231	790.7608
1.08	662.4527	698.2028	734.7412	769.9699
1.09	647.9173	681.5408	715.8859	748.7137
1.1	633.0285	664.7565	696.8326	727.6644
1.11	618.0513	648.0611	678.145	707.2248
1.12	603.7597	631.8233	660.2385	687.6578
1.13	590.4588	616.4898	643.3545	669.2069
1.14	577.9593	602.3549	627.6127	651.9919
1.15	566.3839	589.317	613.0394	636.0695
1.16	555.7827	577.2266	599.6299	621.5042
1.17	545.9841	566.0814	587.6526	608.3181
1.18	537.1166	556.1358	576.726	596.3629
1.19	529.4186	547.162	566.746	585.3703
1.2	522.5354	539.1712	557.66	575.4367
1.21	516.0385	532.1296	549.4128	566.303
1.22	510.1198	525.8906	541.8232	557.878
1.23	505.113	519.9536	535.0808	550.2667

**Table D-3 Temperature variation at time range of 0.74-1.23 for PBT/PET 75/25**

	<i>P=90W</i>	<i>P=95W</i>	<i>P=100W</i>	<i>P=105W</i>
<b>Time(Sec)</b>	<b>Temperature(K)</b>	<b>Temperature(K)</b>	<b>Temperature(K)</b>	<b>Temperature(K)</b>
0.74	306.2192	307.225	307.7646	308.0459
0.75	309.1917	310.5085	311.2119	311.6457
0.76	312.7259	314.4754	315.3857	316.0085
0.77	317.3012	319.3479	320.5222	321.387
0.78	322.7145	325.3208	326.8038	327.9448
0.79	329.3308	332.4397	334.2853	335.9202
0.8	337.1161	340.9532	343.2495	345.3368
0.81	346.3251	350.9778	353.7345	356.3708
0.82	356.9417	362.4343	365.9907	369.2327
0.83	369.1363	375.3813	379.7857	383.8757
0.84	382.884	389.8868	395.2038	400.2592
0.85	398.2875	406.1195	412.4928	418.6209
0.86	415.2954	424.1427	431.7464	439.0482
0.87	433.8935	443.9182	452.8985	461.5974
0.88	453.8947	465.2302	475.5867	486.7685
0.89	475.1299	488.0425	501.3761	517.363
0.9	496.2353	514.7343	532.4379	551.291
0.91	519.9619	546.606	568.9032	591.6773
0.92	550.5037	580.455	606.2934	633.2656
0.93	583.1964	614.9687	643.859	673.7959
0.94	613.8441	648.0186	679.9067	712.8016
0.95	641.916	678.8322	713.2634	749.0033
0.96	666.8505	706.1086	742.7705	781.0045
0.97	687.8364	728.9876	767.4451	808.1926
0.98	704.2338	746.7897	786.5295	830.7722
0.99	715.7634	759.3767	799.6312	847.0324
1	722.3541	766.1608	806.6865	853.573

	<i>P=75W</i>	<i>P=80W</i>	<i>P=85W</i>	<i>P=90W</i>
<b>Time(Sec)</b>	<b>Temperature(K)</b>	<b>Temperature(K)</b>	<b>Temperature(K)</b>	<b>Temperature(K)</b>
1.01	721.5058	764.0996	804.0302	848.7913
1.02	714.9522	756.7485	795.6021	838.9266
1.03	704.9686	745.9891	783.4938	824.9377
1.04	692.316	732.6282	768.5635	808.0459
1.05	678.0136	717.3917	751.6317	788.9847
1.06	663.6613	700.8751	733.3909	768.6282
1.07	649.2669	683.7908	714.4906	747.7328
1.08	634.5562	666.6468	695.5784	726.954
1.09	619.6184	649.9194	677.148	706.764
1.1	605.3981	633.8739	659.5317	687.4799
1.11	592.2548	618.6951	642.9069	669.3687
1.12	579.8145	604.5945	627.3323	652.4786
1.13	568.277	591.7791	613.2565	636.8522
1.14	557.7002	579.9592	600.2408	622.1002
1.15	548.0437	569.1419	588.318	608.9275
1.16	539.3861	559.3131	577.4171	596.8201
1.17	532.8723	550.4725	567.4847	585.6521
1.18	526.3973	542.4854	558.5941	575.4533
1.19	519.4792	536.1469	550.5141	566.1968
1.2	512.8991	530.8214	543.2369	557.8049
1.21	507.0001	525.0867	537.3092	550.2987
1.22	503.0727	518.9854	532.5787	543.8098
1.23	499.9591	513.0919	527.6743	538.3578

## Appendix E

The *MATLAB* used in order to combine the temperature history resulted in chapter 6 with the degradation model discussed in chapter 7 is presented in this appendix:

```
function degradation(TempMat)
    n= TempMat(1,3);
    R=8.314472;
    E= TempMat(2,3);
    A= 2.7182^(TempMat(3,3));
    sz=max(size(TempMat)) ;
    y=zeros(size(TempMat)) ;
    z=1;
    y(:,1)=TempMat(:,1);
    y(:,2)=TempMat(:,2);
    final_mass_percentage=0.05 ;
    NonDegraded_Ratio=1 ;
    y(1,4)=100;
    for t=2:sz
        integral=0;
        for j=2:t
            integral= integral + exp (-(E)/(R * (y(j,2))))*(y(j,1)-
                y(j-1,1));
        end
        NonDegraded_Ratio=((A*(n-1)*integral) +1)^(1/(1-n)) ;
        y(t,4)=100*(1- NonDegraded_Ratio)*final_mass_percentage
            +NonDegraded_Ratio);
    end
    disp(y);
    disp('Press any key to save the results in an Excel datasheet...');
    pause ;
    xlswrite('TGA_DATA11',y(75:125,:));
    clc ;
    figure
    plot(y(:,1),y(:,4), 'r');
end
```

Figure E-1, Figure E-2 and Figure E-3 show the treated degradation data in order to measure the order of the reaction and the activation energy of a degradation reaction following Freeman-Carroll method. Figure E-4, Figure E-5 and Figure E-6 demonstrates the frequency factor measured by the same method.

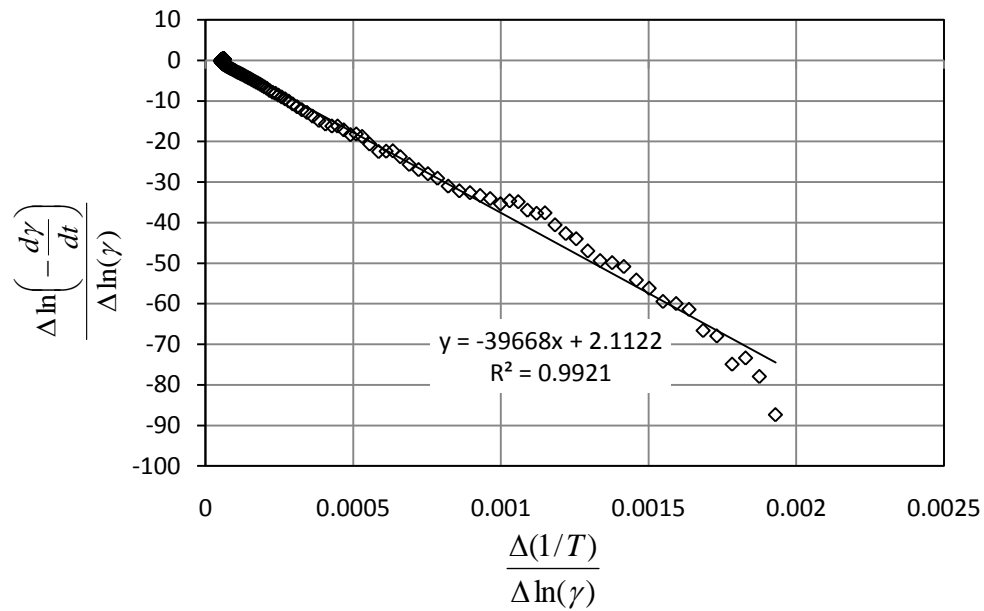


**Figure E-1 Linear Relationship for Order of the Reaction (*n*) and Activation Energy (*E*) for PBT/PET 100/0**

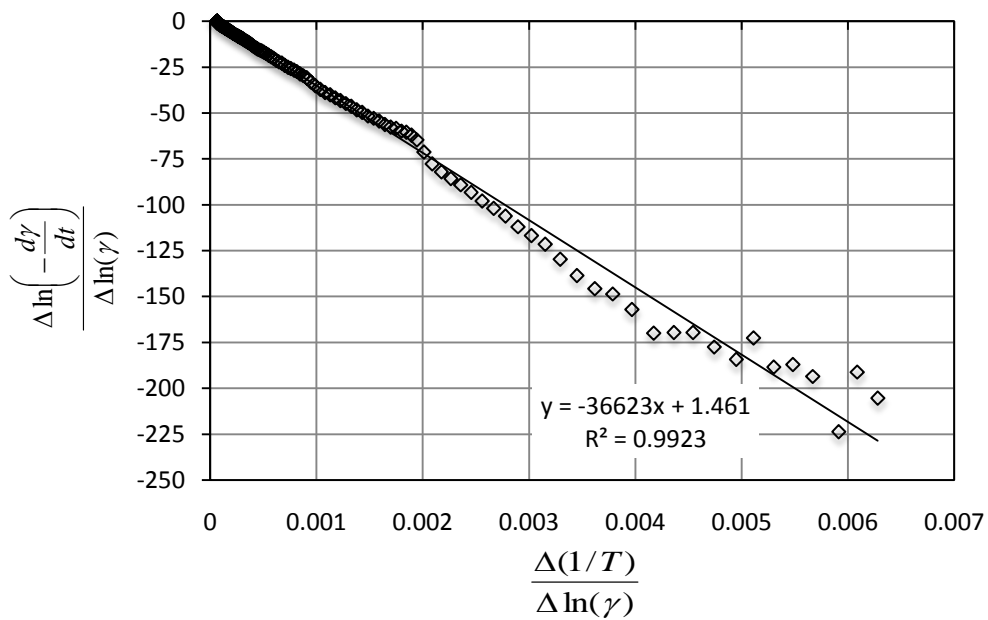


**Figure E-2 Linear Relationship for Order of the Reaction (*n*) and Activation Energy (*E*) for PBT/PET 90/10**

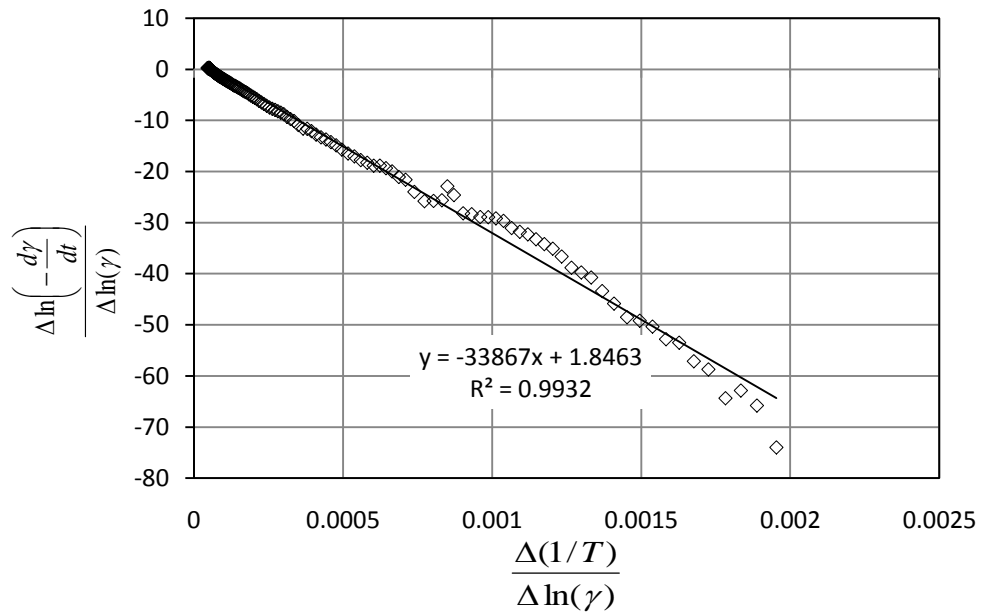


**Figure E-3 Linear Relationship for Order of the Reaction ( $n$ ) and Activation Energy ( $E$ ) for PBT/PET 75/25**

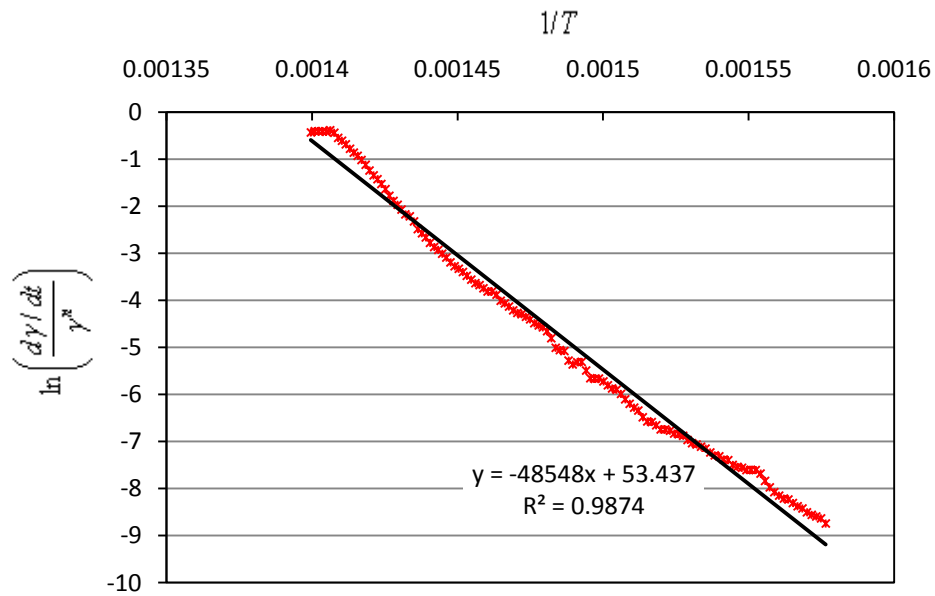


**Figure E-4 Linear Relationship used for measuring frequency factor ( $A'$ ) for PBT/PET 100/0**

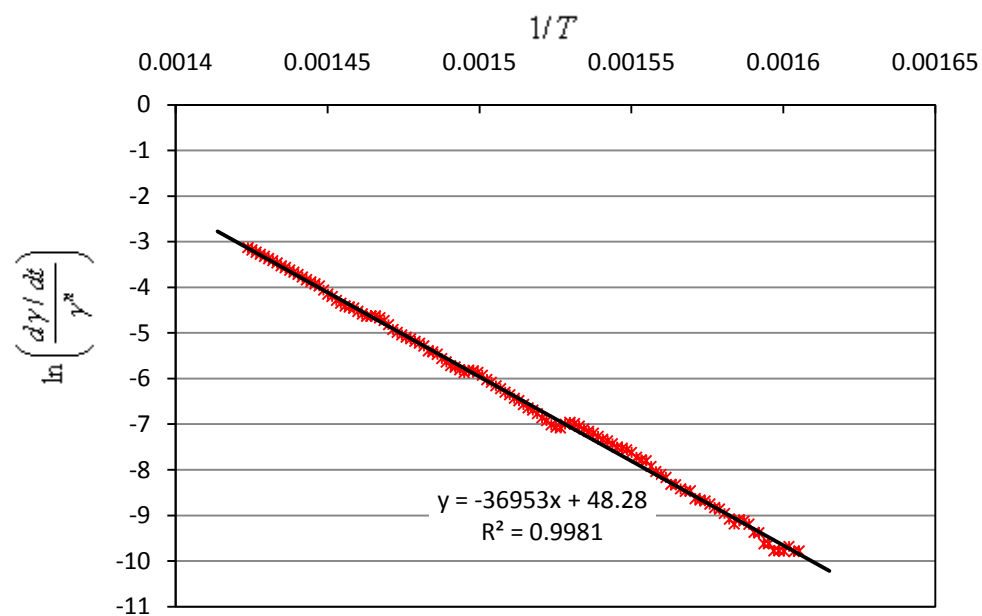


Figure E-5 Relationship used for measuring frequency factor ( $A'$ ) for PBT/PET 90/10

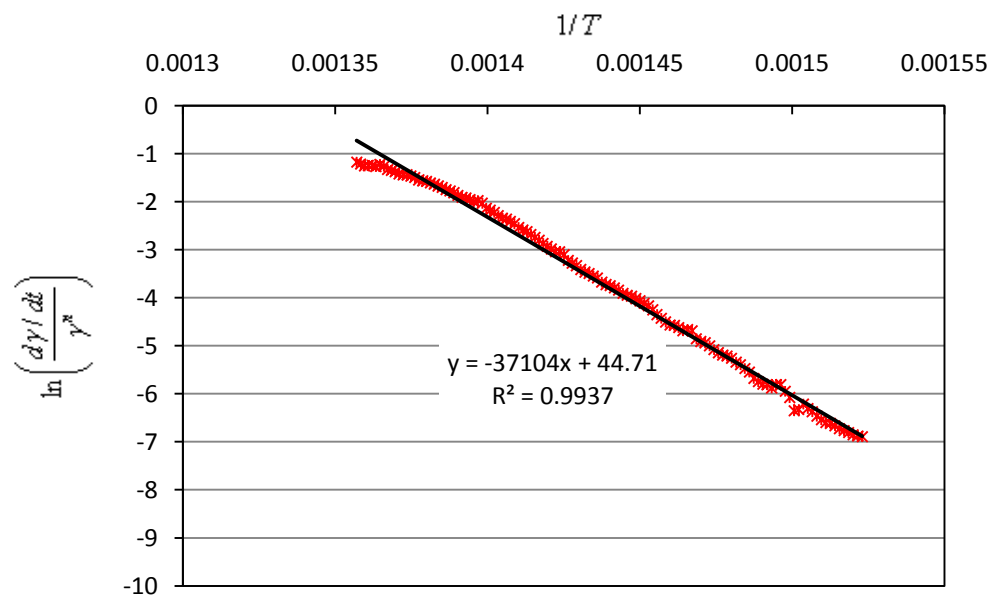


Figure E-6 Relationship used for measuring frequency factor ( $A'$ ) for PBT/PET 75/25